UNIVERSITY OF GENOA
POLYTECHNIC SCHOOL

DIME - Department of Mechanical, Energy, Management and Transport Engineering

PhD in Engineering of Models, Machine and Systems for Energy, Environment and Transport

PhD Thesis
XXXV Cycle

Dynamic analysis and energy management strategies of micro gas turbine systems integrated with mechanical, electrochemical and thermal energy storage devices

Supervisor:
Prof. Mario Luigi Ferrari

Co-supervisor:
Prof. Aristide Fausto Massardo

Candidate:
Martina Raggio

January 2024

UNIVERSITÀ DEGLI STUDI DI GENOVA
SCUOLA POLITECNICA

DIME - Dipartimento di Ingegneria Meccanica, Energetica, Gestionale e dei Trasporti

Dottorato di Ricerca in Ingegneria delle Macchine e dei Sistemi per l'Energia, l'Ambiente e i Trasporti
Curriculum Ingegneria Matematica e Simulazione

Tesi di Dottorato
XXXV Ciclo

Analisi dinamica e strategie di gestione di sistemi con microturbine a gas integrate con sistemi di accumulo di energia meccanica, elettrochimica e termica

Supervisore:
Chiar.mo Prof. Mario Luigi Ferrari

Co-supervisore:
Chiar.mo Aristide Fausto Massardo

Candidato:
Martina Raggio

Gennaio 2024

Contents

Abstract

The growing concern related to the rise of greenhouse gases in the atmosphere has led to an increase of share of renewable energy sources. Due to their unpredictability and intermittency, new flexible and efficient power systems need to be developed to compensate for this fluctuating power production. In this context, micro gas turbines have high potential for small-scale combined heat and power (CHP) applications considering their fuel flexibility, quick load changes, low maintenance, low vibrations, and high overall efficiency. Furthermore, the combination of micro gas turbines with energy storage systems can further increase the overall system flexibility and the response to rapid load changes. This thesis aims to analyse the integration of micro gas turbines with the following energy storage systems: compressed air energy storage (CAES), chemical energy storage (using hydrogen and ammonia), battery storage, and thermal energy storage.

In particular, micro gas turbines integrated with CAES systems and alternative fuels operate in different working conditions compared to their standard conditions. Applications requiring increased mass flow rate at the expander, such as CAES and the use of fuels with low LHV, such as ammonia, can potentially reduce the compressor surge margin. Conversely, sudden composition changes of high LHV fuels, such as hydrogen, can cause temperature peaks, detrimental for the turbine and recuperator life. A validated model of a T100 micro gas turbine is used to analyse transitions between different conditions, identify operational limits and test the control system.

Starting from the dynamic constraints defined in the related chapters, in the final part, an optimisation tool for energy management is developed to couple the micro gas turbine with energy storage systems, maximizing the plant profitability and satisfying the local electrical and thermal demands. For the modelling of the CAES system and alternative fuels, the operating constraints

obtained from the initial analyses are implemented in the optimisation tool. In addition, a battery and thermal energy storage system are also considered.

In the first part, a comprehensive analysis of the T100 combined with a second-generation CAES system showed enhanced efficiency, reduced fuel consumption, reduced thermal power output and increased maximum electrical power output due to the reduction of the rotational speed. The study identified optimal air injection constraints, demonstrating a +3.23% efficiency increase at 80 kW net power with a maximum mass flow rate of 50 g/s. The dynamic analysis exposed potential instabilities issues during air step injections, mitigated by using ramps at a rate of +0.5 (g/s)/s for safe and rapid dynamic mode operation. The second part explored the effects of varying H_2-NG and NH_3-NG blends on the T100 mGT. Steady-state results showed increased power output with hydrogen or ammonia, notably +6.1 kW for 100% H_2 and up to +11.3 kW for 100% NH_3. Transient power steps simulations showed surge margin reductions, especially at lower power levels with high concentrations of ammonia, highlighting the need for controlled transitions. Controlled ramps were effective in preventing extreme temperature peaks during fuel composition changes. The final chapter focused on developing an energy scheduler for different plant setups, evaluating four configurations. For a typical day of the month of April of the Savona Campus, the integration of the CAES lead to relative savings of +8.1% and power-to-H_2 of +5.3% when surplus electricity was not sold to the grid. Conversely, with the ability to sell excess electricity, CAES and battery energy storage (BES) systems exhibit modest savings of +1.2% and +2.4%, respectively, while the power-to-H_2 system failed to provide economic advantages.

Sommario

La crescente preoccupazione legata all'aumento dei gas serra sta portando ad un aumento di energia prodotta da fonti rinnovabili. Tuttavia, a causa della loro imprevedibilità e intermittenza, risulta necessario sviluppare nuovi sistemi più flessibili ed efficienti. In questo contesto, le microturbine a gas hanno un elevato potenziale per applicazioni con produzione combinata di calore e potenza (CHP) su piccola scala, grazie alle basse vibrazioni, flessibilità di combustibile, rapidi cambiamenti di carico, bassa manutenzione ed elevata efficienza complessiva. Inoltre, l'abbinamento delle microturbine a gas con sistemi di stoccaggio può aumentare ulteriormente la flessibilità e la rapida risposta alle variazioni rapide del carico. Questa tesi mira ad analizzare l'integrazione delle microturbine a gas con i seguenti sistemi di stoccaggio: sistemi ad aria compressa (CAES), accumuli chimica (tramite idrogeno e ammoniaca), stoccaggio dell'energia tramite batterie e stoccaggio dell'energia termica.

In particolare, il funzionamento con sistemi di stoccaggio dell'energia mediante aria compressa e carburanti alternativi comporta diverse condizioni operative rispetto al normale funzionamento. Applicazioni che richiedono un aumento di portata all'espansore, come il CAES e l'uso di combustibili a basso LHV, come l'ammoniaca, possono aumentare il rischio di pompaggio del compressore. Al contrario, improvvisi cambiamenti di composizione dei carburanti ad alto LHV, come l'idrogeno, possono causare picchi di temperatura dannosi per la vita della turbina e del recuperatore. In questa tesi, è stato utilizzato un modello validato di microturbina a gas T100 per analizzare le transizioni tra diverse condizioni, identificare i limiti operativi e testare il sistema di controllo.

Grazie ai risultati ottenuti in condizioni dinamiche per il calcolo di vincoli operativi, nella parte finale, è stato sviluppato uno strumento di ottimizzazione per la gestione dell'energia con microturbina e i sistemi di accumulo, per massimizzare la redditività e soddisfare le domande elettriche e termiche. I vincoli operativi ottenuti dall'analisi iniziale del CAES e dei combustibili

alternativi e sono stati inclusi. L'analisi inoltre include una batteria e un sistema di accumulo termico.

Nella prima parte della tesi, un'analisi completa della microturbina T100 integrata con un sistema CAES di seconda generazione ha mostrato una maggiore efficienza, un ridotto consumo di carburante, una ridotta potenza termica e un aumento della potenza massima elettrica grazie alla riduzione della velocità di rotazione. Lo studio ha identificato i vincoli ottimali di iniezione dell'aria, dimostrando un aumento di efficienza del +3.23% a una potenza netta di 80 kW con una portata massica massima di 50 g/s. L'analisi dinamica ha evidenziato potenziali problemi di instabilità durante le iniezioni di aria, mitigati utilizzando rampe a una velocità di +0.5 (g/s)/s per un funzionamento rapido e sicuro in modalità dinamica. La seconda parte ha analizzato gli effetti delle variazioni delle miscele H_2-NG e NH_3-NG sulla T100. I risultati stazionari hanno mostrato un aumento della potenza erogata con idrogeno o ammoniaca, in particolare +6.1 kW per il 100% H_2 e fino a +11.3 kW per il 100% NH_3. Le simulazioni di variazioni di potenza transitori hanno mostrato riduzioni del margine di pompaggio, soprattutto a livelli di potenza più bassi con alte concentrazioni di ammoniaca, evidenziando la necessità di transizioni controllate. Le rampe controllate si sono rivelate efficaci nel prevenire picchi di temperatura estremi durante i cambiamenti nella composizione del carburante. Il capitolo finale si è concentrato sullo sviluppo di un ottimizzatore energetico per diverse configurazioni di impianto, valutando quattro configurazioni. Per una giornata tipo del mese di aprile del Campus di Savona, l'integrazione del CAES ha comportato un risparmio relativo del +8.1% e di +5.3% con H_2 quando l'elettricità in eccesso non è stata venduta alla rete. Al contrario, con la possibilità di vendere l'elettricità in eccesso, i sistemi CAES e batterie mostrano risparmi modesti, rispettivamente del +1.2% e del +2.4%, mentre il sistema power-to-H_2 non è riuscito a fornire vantaggi economici.

Acknowledgements

Over the last three years, I have had the opportunity and pleasure to work with many different people, for which I am very grateful. In particular, I would like to thank Mario for his continuous support and mentorship during the challenging times of my PhD project. I would also like to thank all the other colleagues of the University of Genoa that I have cooperated with during these years, especially Ravi that started with me (more or less) this PhD journey.

As part of my PhD, I had the opportunity to work at different places abroad. The experience gained at these places has fundamentally improved my skills to cooperate with people from different backgrounds. For this I am also vey grateful. I worked at ENGIE in Brussels, for which I would like to thank Marc for his support. I have also worked at Acceleron in Baden, for which I would like to thank Jean-Francois for his support and great advice. It was great to work in the R&D team under his guidance and enthusiasm. Furthermore, I have worked at the University of Stavanger, where I have met many great people and friends. I would like to thank all the people I cooperated with, and in particular, Mohsen and Reyhaneh for their support.

My work on the NextMGT project has given me the opportunity to further build upon my knowledge of gas turbines and energy storage systems and has provided me with a great introduction to the academic field. I feel confident that this experience has given me a strong basis for my future professional career, and at the same time allowed me to meet great friends in different parts of the world.

Finally (last but not least), I would like to thank my mom and dad for their great care. I would also like to thank Marijn, for his support during the most challenging times.

Nomenclature

Abbreviations and Acronyms

A-CAES	Adiabatic Compressed Air Energy Storage
AEL	Alkaline Electrolyses
AE-T100	Ansaldo Energia T100
AIST	National Institute of Advanced Industrial Science and Technology
A-TES	Aquifers Thermal Energy Storage
ATR	Auto Thermal Reforming
BECCS	Bioenergy with Carbon Capture and Storage
B-TES	Borehole Thermal Energy Storage
CAES	Compressed Air Energy Storage
CCS	Carbon Capture and Storage
CHP	Combined Heat and Power
CSP	Concentrated Solar Panels
D-CAES	Diabatic Compressed Air Energy Storage
DER	Distributed Energy Resource
DHN	District Heating Network
DLR	German Aerospace Center
EGR	Exhaust Gas Recirculation
ESS	Energy Storage Systems
FBES	Flow Batteries
FES	Flywheels
FF	Fossil Fuel
GME	Gestore Mercati Elettrici
GHG	Greenhouse Gasses
I-CAES	Isothermal Compressed Air Energy Storage
IES	Innovative Energy Systems

IRENA	International Renewable Energy Agency
I-TES	Ice-cool Thermal Energy Storage
LA	Lead acid
LH-TES	Latent Heat Thermal Energy Storage
Li-ion	Lithium ion
MCFC	Molten Carbonate Fuel Cells
MG	Microgrid
mGT	micro Gas Turbine
mHAT	micro-Humid Air Turbine
MM	Main line mass flow
N	Rotational Speed
Na-S	Sodium Sulphur
NextMGT	Next Generation of Micro Gas Turbines for High Efficiency, Low Emissions, and Fuel Flexibility
Ni-Cd	Nickel Cadmium
OPEX	Operating Expense
PCM	Phase Change Materials
PEM	Polymer Electrolyte Membranes
PEMEC	Polymer Electrolyte Membranes Electrolyser
PHES	Pumped Hydro Energy Storage
PI	Proportional Integral
PID	Proportional Integral Derivative
PRC	Recuperator Outlet Pressure Cold Side
PRC1	Recuperator Inlet Pressure Cold Side
PVM	Combustor Inlet Pressure
RE	Renewable Energy
RES	Renewable Energy Source
RRMSE	Relative Root-Mean Squared Error
S-CAES	Second Generation Compressed Air Energy Storage
ScSZ	Scandia-Stabilised Zirconia
SH-TES	Sensible Heat Thermal Energy Storage

SMR	Steam-Methane Reforming
SOC	State of Charge
SOEC	Solid Oxide electrolysers
SOFC	Solid Oxide Fuel Cells
SPM	Smart Polygeneration Grid
TC-TES	Thermochemical energy storage
TES	Thermal Energy Storage
TOT	Turbine outlet temperature
TPG	Thermochemical Power Group
TRC1	Recuperator inlet temperature cold side
TRC2	Recuperator outlet temperature cold side
TRE	Recuperator outlet temperature hot side
TVCC1	Combustor inlet temperature
UiS	University of Stavanger
VUB	Vrije Universiteit Brussel
YSZ	Yttria-stabilised zirconia

Variables

A	Area [m^2]
C	Momentum contribution [Pa]
c_p	Specific Heat at Constant Pressure [$J\ kg^{-1}\ K^{-1}$]
c_v	Specific Heat at Constant Volume [$J\ kg^{-1}\ K^{-1}$]
D	Diameter [m]
f	Friction coefficient [–]
h	Enthalpy [$W\ m^{-2}\ K^{-1}$]
J	Rotational inertia [$kg\ m^2$]
k_p	Surge margin [–]
L	Total length [m]
LHV	Low heating value [$J\ kg^{-1}$]

M	Mass [kg]
$\dot{m}$	Mass flow rate [kg/s]
N	Rotational speed [rpm]
p	Pressure [Pa]
P	Power [W]
$\dot{q}$	Heat flux [W]
T	Temperature [°C]
T_o	Ambient temperature [°C]
v	Velocity [m/s]
V	Volume [m^3]
x	Discretised axial length [m]

Greek symbols

η	Efficiency
β	Pressure ratio
γ	Ratio of the Specific Heats at Constant Pressure and Volume
Δ	Delta
ρ	Density
ω	Angular rotational speed

Subscripts and Superscripts

air	Referred to air properties
charge	Referred to the charging phase
cold	Cold side
comb	Combustor
comp	Compressor
el	Electrical
eq	Equivalent
fuel	Referred fuel

gas	Referred to gas properties
gen	Generated
hot	Hot side
i	i-th element in the discretisation
in	Referred to inlet properties
inj	Referred to the injection phase
j	j-th element in the discretisation
loss	Losses
m	Mechanical
max	Maximum
mean	Referred to average properties
net	Net
out	Referred to outlet properties
pipe	Pipe
rec	Recuperator
s.l.	Surge line
solid	Referred to the solid part
tank	Referred to the storage tank
th	Thermal
turb	Turbine

1 Introduction

1.1 Energy scenario and future of power generation

The global energy landscape is currently undergoing a transformative phase, driven by the need to deal with multiple challenges simultaneously: producing secure energy (electricity and heat) to meet the ever-growing demand while continuously reducing greenhouse gasses (GHG) and pollutants emissions [1]. In response to these pressing issues, new international agreements and policies are taking place. The first initiatives to reduce air pollution started in the late 1970s. Later in 1997, the Kyoto Protocol was adopted and went into force in 2005, laying the foundations for future climate agreements on the international level. However, the standards set by the protocol received some criticism, since actions were required only from the developing countries and global emissions continued to rise compared to 1990 levels [2]. The Paris Agreement, adopted in 2015, which entered into force in 2016, included more severe measures: governments set targets to avoid the rise of the global average temperature to 2°C above preindustrial levels, and pursue efforts to keep it below 1.5°C. In this case actions were also required from developing countries, comprising the major carbon emitters of the Global South that are China and India (as shown in Figure 1-1) [3].

Examining more in detail the worldwide greenhouse gas emissions, Figure 1-1 shows the history of the rising annual CO_2 emissions by world region and Figure 1-2 analyses potential scenarios for greenhouse gas emissions in the future, based on various assumptions from the Climate Action Tracker (based on national policies and pledges as of November 2021) [4]. These assumptions include 1) a scenario without any climate policies, 2) a scenario where current policies are maintained, 3) a scenario where all countries fulfil their commitments for future emissions reductions, and scenarios 4) and 5) where the pathways essential for limiting global warming to either 2°C or 1.5°C within this century are followed.

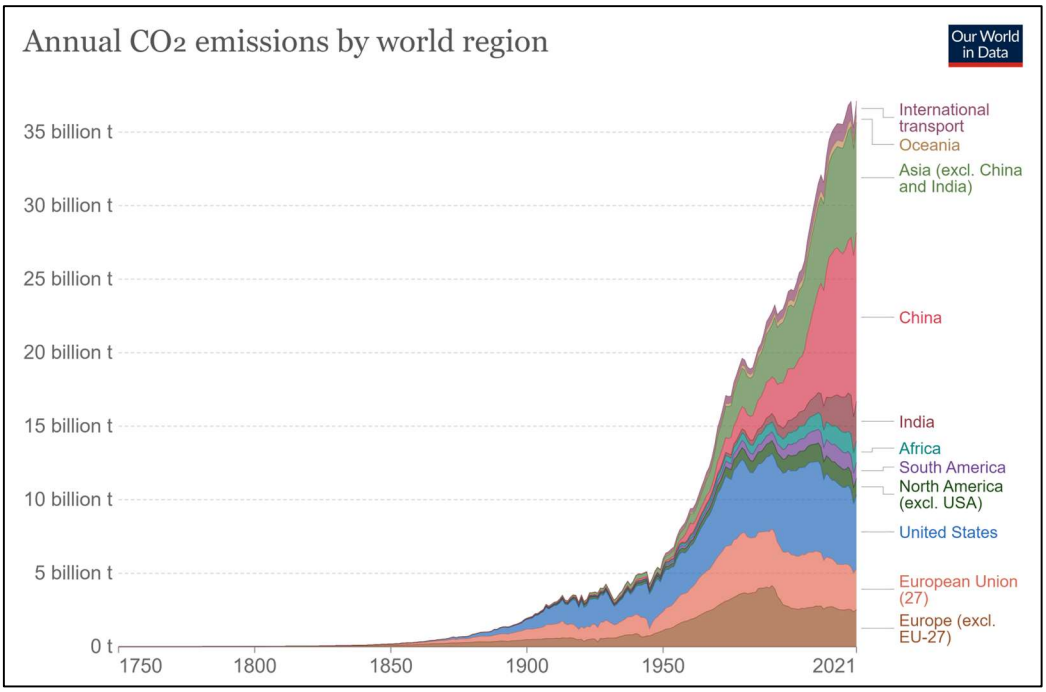

Figure 1-1. Annual CO_2 emissions by world region [4].

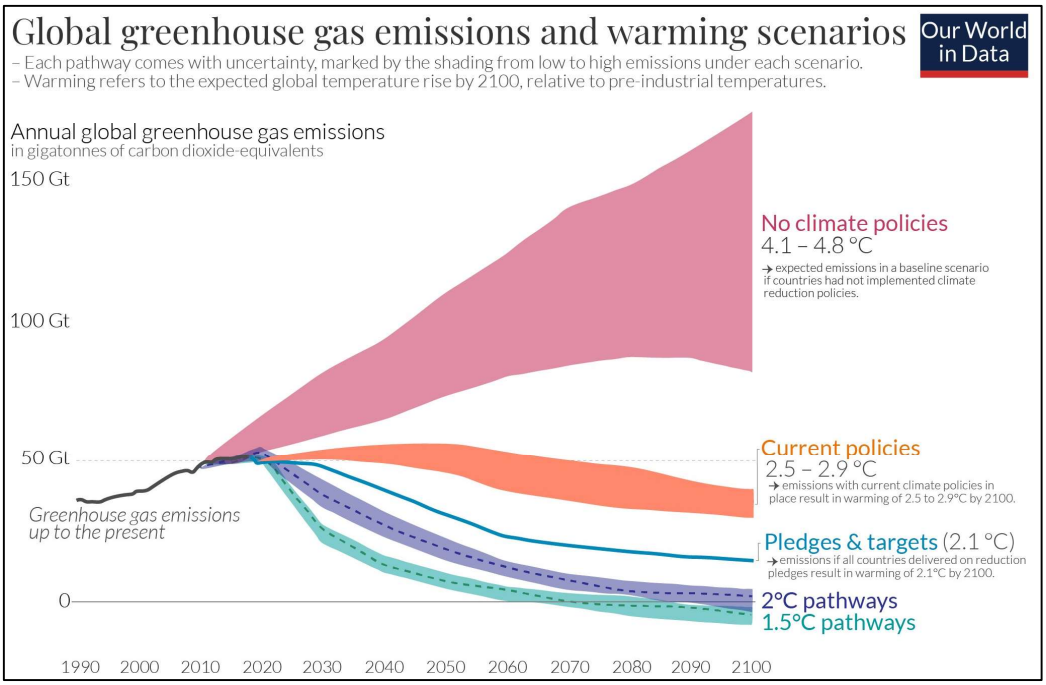

Figure 1-2. Global greenhouse gas emissions and warming scenarios [4].

These projections indicate that, if every nation fulfils its existing targets and pledges outlined in the Paris Agreement, the average temperature rise by 2100 would range between 2.5 and 2.8°C. This outcome would significantly surpass

the objective to limit warming below 2°C. To achieve a 2°C temperature limit goal, substantial enhancements of the present commitments are required. If the limit is set to 1.5°C, even more urgent and rapid actions are needed. It is evident that the transition must be accelerated to effectively meet the climate targets effectively.

Despite noticeable improvements in some areas, there are significant mismatches between utilisation of current technologies and the ones needed to achieve the Paris climate goals by 2050. The energy transition heavily relies on the development of new technologies, improvement of energy efficiency of energy conversion and cost reduction. The International Renewable Energy Agency (IRENA), in its World Energy Transitions Outlook 2022 document [5], outlines a strategic approach to the energy transition following the 1.5 °C pathway, summarised in Figure 1-3.

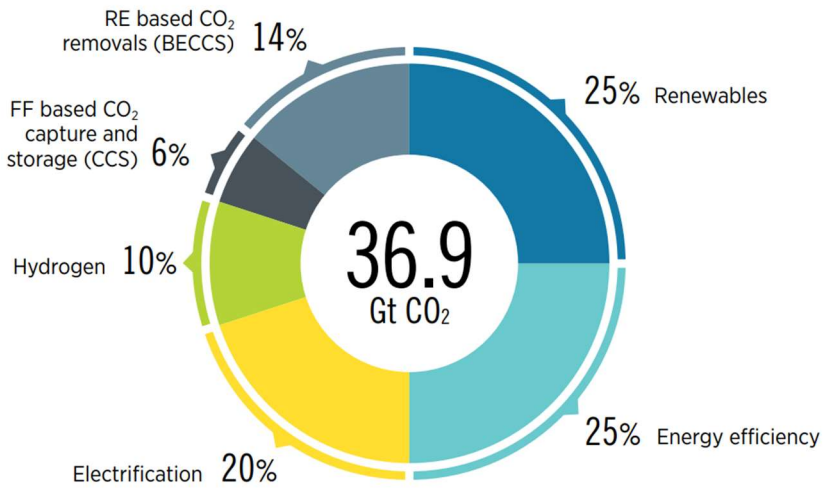

Figure 1-3. Achievement of emissions by 2050 by means of six technological paths [5].

Wind and solar energy will play a dominant role in this transition, as their costs continue to decline, while efficiency steadily increases. Energy efficiency increase is equally important and can serve to reduce costs, improve energy security, and create new jobs in the energy sector. Energy efficiency not only includes the technological improvements of energy systems, that results in a better conversion from a primary source to electricity or heat, but also a

reduction in its consumption and improvements on its conservation. Electrification is a key strategy for the future energy scenario driven by higher penetration of renewable energy sources, which also contributes to improved air quality. Hydrogen and its derivatives obtained from renewables will be required to replace other fossil fuels. Carbon capture usage and storage is also required to support the transition to a low-carbon economy.

Given the rapid timescales involved, policy interventions become crucial to accelerate the transition process. Balancing these policies is critical to both incentivise the adoption of cleaner technologies and promote a gradual reduction in hydrocarbon consumption from fossil origin, avoiding disruptive price volatility and potential energy shortages. Each country's current level of development plays a significant role in determining the fundamental issues and the delicate balance between developed and developing nations. Navigating the energy transition globally presents fundamental challenges, particularly in striking a balance across different countries and economies [6]. Moreover, the energy transition is not only a matter of technological and economic implications but also geopolitical consequences. The reduction in fossil fuel use will impact fossil fuel-producing nations, potentially altering international relations and increasing the risk of conflicts. Additionally, securing access to limited reserves of essential metals and minerals needed for key energy transition technologies will become a critical global issue [7].

1.2 Renewable energy sources challenges

According to the IRENA, global renewable energy capacity grew by 9.6% in 2022 [5]. Despite the increase of the last years, energy production from RES needs to grow three times compared to the current level by 2030 to stay on the 1.5°C pathway. Renewable energy sources are non-dispatchable, often intermittent, and not fully predictable (despite the growing improvements in forecasting tools). These are barriers that increase the complexity of the grid management and prevent a faster penetration of RES [8]. Being non-dispatchable means that the energy cannot be produced based on the demand

needs, but it is dependent on the availability of natural sources, mainly wind and sun. For instance, during high availability of renewable power but low electrical demand, the electricity needs to be transferred through transmission lines to locations where the demand is higher. However, the transportation of energy through long distances brings high losses. Moreover, there are some physical limitations to this process since the capacity of the transmission lines cannot be exceeded, as it would cause congestions issues. In this case, the energy needs to be curtailed resulting in a waste of clean energy and in a loss of the plant revenue.

An example of overgeneration risk can be visually identified in the famous so called "duck curve", shown in Figure 1-4 [9].

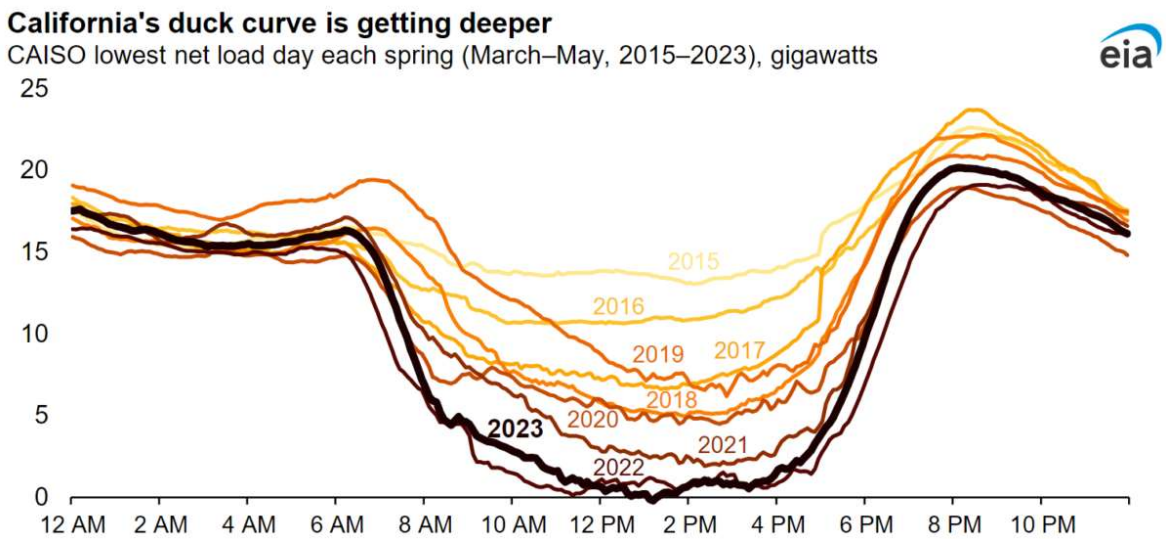

Figure 1-4. "The Duck Chart" [9].

This graph represents the net power demand of a typical spring day in California. This shows a significant reduction of the demand over the years during the sunny hours of the day, because of the increasing installation of solar panels. Another issue that can be noticed from this graph is the ramp increase needed during the evening hours, due to the combined effect of the reduced power produced from solar panels and the increased power demand. This poses additional challenges for conventional generators that need to quickly compensate for the non-availability of renewables sources.

Accurate renewable production is vital for their integration, particularly at high penetration levels. Advanced forecasting methods, including AI and big data analysis, have improved power generation forecasts. Short-term accurate forecasts help asset owners and market players in electricity markets, reducing penalties for imbalances. Long-term forecasts aid in system planning and the allocation of balancing reserves for extreme weather events. Forecasting accuracy decreases as the forecast time horizon increases, making it essential to choose an appropriate time horizon for accurate forecasting [10].

RES are also intermittent and this can lead to grid stability issues especially if there is a fast rate of change [11]. The intermittency is typical of electricity production from solar PV during partly cloudy weather. Figure 1-5 shows an example of power generation from solar panels for 3 different days. Day 1 is representative of a completely sunny day and therefore the energy production is smooth. However, day 2 and 3 represent the solar production with intermittency during cloudy days, where day 3 shows a higher variability of clouds during the day.

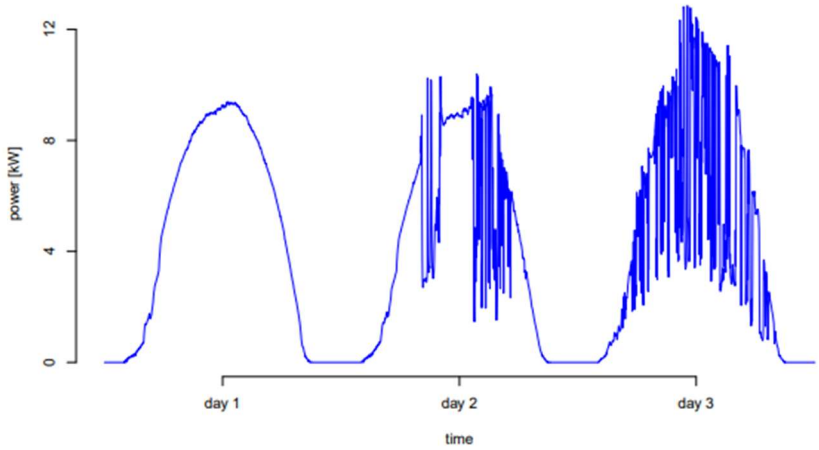

Figure 1-5. Example of intermittent power production from solar panels [11].

In a scenario with a low share of RES, these issues can be overcome by employing conventional generator that can compensate to these fluctuations ensuring that the energy supply is always matching the demand and providing ancillary services to maintain grid stability. However, since the installation of

RES must increase and the production from carbon-based generators reduce, alternative solutions to reach higher flexibility and promote a higher penetration of renewables are required.

1.3 Energy storage systems for flexibility

Energy Storage Systems (ESSs) are devices able to store energy during excess of renewable production and release it later at a more convenient time. Therefore, ESS have the potential to reduce the mismatch between power production and demand, relieving the grid during the surplus of renewable production while supporting the reduction of fossil fuel utilisation [12,13].

Depending on the energy conversion process and storage medium, different storage systems are available, each of them with advantages and drawbacks depending on the considered application. There is not a unique classification, but different criteria can be used, for example based on the energy conversion mechanisms, performance characteristics, end-use applications, and so on.

In this paragraph the most common energy storage technologies are classified based on the conversion process [12,14,15]:

- Thermal energy storage systems
- Electrochemical energy storage systems
- Chemical energy storage systems
- Mechanical energy storage systems

In general, a form of energy (for example, electricity or heat) can be converted into another form for the storage and then reconverted back into another one to be used. For example, in chemical ESSs, electricity can be used to synthetise an e-fuel (chemical potential energy), which could be later re-converted in electricity by means of an engine or in heat, for example through its combustion. In thermal energy storage devices, generally the stored thermal energy is directly used later in the same form without conversion in another form. However, especially for high temperature thermal storage devices, the available

heat could be used to also generate electricity by heating up a working fuel of an engine. In mechanical energy storage devices, for example compressed air storage systems, electricity can be converted into mechanical energy (as potential energy of the compressed air). This energy can be reconverted into electricity if air is expanded into a turbine. Another possibility is to also use the heat generated during the compression in CHP applications or directly employ the compressed air for other purposes, such as in industrial and manufacturing applications, to power pneumatic tools that rely on compressed air to perform mechanical work directly.

Despite all the numerous possibilities, the classification considered in this work differentiate the ESSs devices only considering the form of energy used for the conversion mechanism, without differentiating between initial and final energy form. This is also the most common classification approach, as reported in different reviews on ESSs devices [14–17].

Figure 1-6 [18] illustrates the utilization of ESSs, which are broadly categorized into large, medium, and small scales based on their discharge time at rated power and power rating. Electrochemical storage systems, including lithium-ion, lead-acid, and sodium-sulphur batteries, are predominantly suitable for applications with a medium discharge time ranging from minutes to hours. High-power storage technologies such as flywheels, supercapacitors, and superconducting magnetic energy storage are appropriate for applications with a short discharge time at rated power. Pumped hydro storage and compressed air energy storage fall between medium discharge times and large-scale systems designed for discharge times at rated power. Energy storage systems currently available for applications related to power quality include supercapacitors, nickel-cadmium batteries, lead-acid batteries, and lithium-ion batteries. Additionally, Flywheels also represent a viable option for such applications [19].

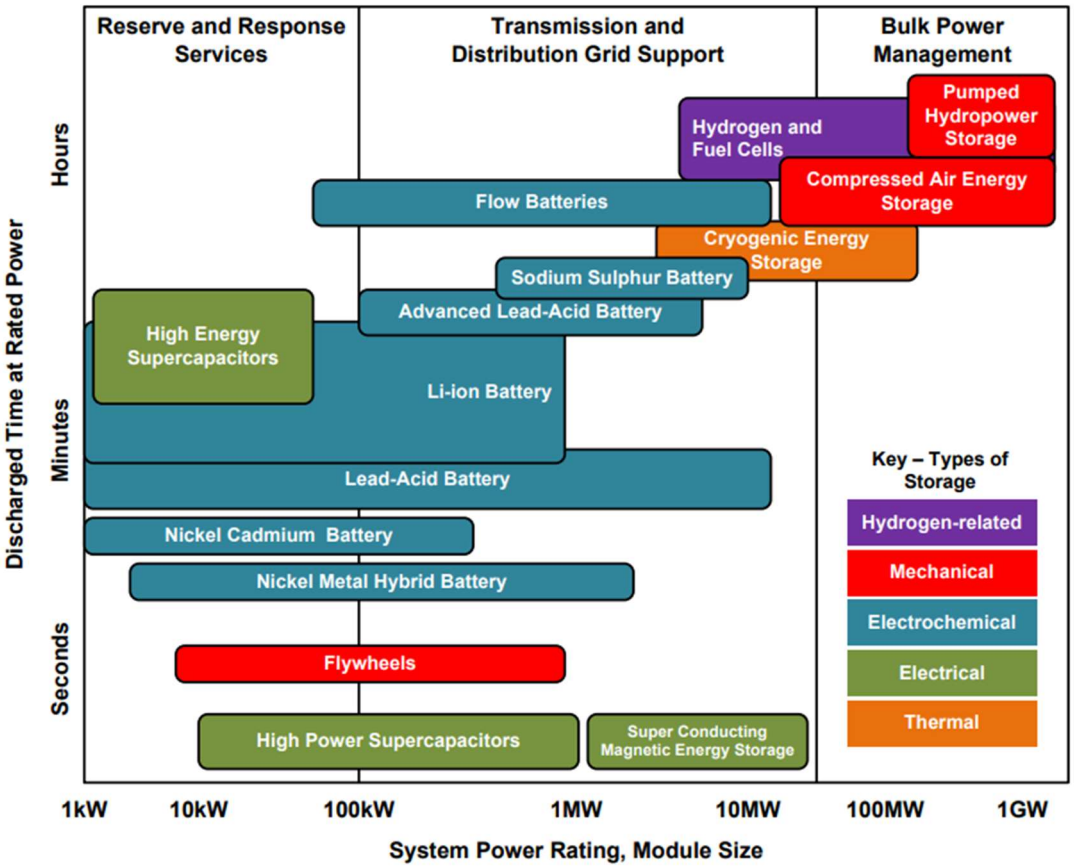

Figure 1-6. Power ranges and discharge power duration of different energy storage technologies [18].

1.3.1 Thermal energy storage

Thermal energy storage systems (TES) store heating or cooling energy into a substance, surrounded by an insulating material. The stored thermal energy can be used in several ways depending on the specific function. The most common applications mainly depend on the operating temperature and capacity of the storage; some examples are buildings/industrial heating or cooling, hot water production and electricity generation. TES can be classified in low-temperature or high-temperature based on their working temperature. Industrial cooling works with temperatures below −18 °C, building cooling in the 0 – 12 °C range, building heating in the 25 – 50 °C range and industrial heat storage higher than 175 °C [20]. Another, more common classification is based on the storing mechanism, where three categories can be considered:

- Sensible heat thermal energy storage (SH-TES)
- Latent heat thermal energy storage (LH-TES)
- Thermochemical energy storage (TC-TES)

In SH-TES thermal energy is stored by increasing or decreasing the storage temperature, LH-TES involves a phase change during charging and discharging while TC-TES indirectly stores heat through a thermochemical reaction.

1.3.1.1 Sensible heat systems

In sensible heat systems [21], heat is stored by increasing or decreasing the temperature of the system. The stored heat is proportional to the heat capacity of the medium, mass of the storage material and the temperature rise between initial and final states. The storage medium can be liquid or solid. The main advantages of SH-TES are their simplicity, ease of implementation, long life cycles. One drawback is related to the significant space required directly impacting capital costs. Another significant drawback is the fact that the discharge always occurs with variable temperature, which does not allow for constant temperature operation.

The most common liquid SH-TES are *hot and cold water TES* [22], where water is stored in tanks located above, below ground or partially buried, depending on the size and space availability. These systems are typically used for intraday storage (e.g., heating during the day and release during the night) since the heat losses become significant for longer time scales if the storage is in the sensible form. The typical tank material is concrete lined with stainless steel to improve insulation and reduce thermal losses due to diffusion through the concrete. Instead of steel liners, high-density concrete, organic foams, inorganic insulations, composites, and phase change materials can also be used as insulation to reduce thermal losses.

Another form of liquid based TESs are aquifers thermal energy storage systems (A-TES) [23], generally used for inter-seasonal storage for regulating the temperature of buildings. An aquifer uses the movement of the water contained

under the soil or bedrock to transfer thermal energy in between, at least, one cold and one hot well. In addition, at least one or more heat pumps are used to exploit the incoming thermal energy and provide the required temperature to the buildings. In winter, groundwater is pumped from the warm well to a heat exchanger. This heat is used to increase the low temperature source of the heat-pump that operates to reach the requested building temperature. This mechanism is reversed during summer, where cold water is pumped out of the cold well to the heat exchanger.

Other possible water-based TES are *cavern thermal energy storage* and *gravel water thermal energy storage.* Cavern TES can be naturals (mines, tunnels, natural structure) or artificials (underground built water reservoirs), with a more expensive construction than the naturals one. Despites some advantages such as high injection and extraction rates, few installations (mainly from natural spaces) are available worldwide [24]. Instead, gravel water TES systems use an underground storage, presenting some economic advantages compared to water tanks as the water is buried in the ground around 5-15 m below the surface. The heat can be exchanged either with direct water transfer or through pipes placed through different layers [25].

If higher storing temperatures (T > 100°C) are needed, *molten-salt TES* can be used. This technology uses a fused inorganic salt characterised with higher boiling temperatures. Other advantages compared to the use of water are low viscosity, low vapour pressure (no need to pressurise the storing tank) and high volumetric heat capacity (smaller volumes required) [26].

Borehole TES (B-TES) is a form of underground storage directly using the solid ground as storage medium. A B-TES is typically used as seasonal storage: vertical boreholes are drilled into the ground so that, during summer, the heat transfer fluid passes through polymer-based pipes located inside the bore holes and heats-up the soil, while during winter the heat is extracted in the reversed direction [27].

Finally, *packed-bed thermal energy stage systems* are solid based TES systems that store energy into a packed bed of solid particles. These particles are heated up by means of a fluid, typically water or air, that circulates through the bed in two possible directions for the charging or discharging of the system. Packed bed systems are simple systems, that employing various heat transfer fluids, have high thermal efficiency with low maintenance costs. However, some of the drawbacks are the large space required for the installation and the possibility of thermal stratification [25].

1.3.1.2 Latent heat systems

Latent heat systems [28] use the process of phase change to absorb and release heat from the storing material. In this way, the TES always operates at constant temperature. Desirable properties of LH-TES are both high latent heat and moderate volume change during the phase transition to avoid issues on the containment vessel. Potentially, all the possible transitions could be exploited sold-solid, solid-liquid, solid-gas, and liquid-gas. Practically, the storage devices based on solid-liquid transformations are the most employed, representing a good trade-off between latent heat and volume change requirements. In details, solid-solid transformations consist of phase transitions between a crystalline or semi-crystalline phase, and another amorphous, semi-crystalline, or crystalline phase [29]. Solid-solid phase changes present small volume variations, but also little latent heat during the passage from one crystalline form to another, conversely solid-gas and liquid-gas transitions have high latent heat of reaction but unacceptable volume variations.

Ice-cool TES (I-TES) are a common LH-TES storage system exploiting the water transition from solid to liquid form and vice versa. During charging, the heat transfer liquid circulates through coils freezing water, during discharging, ice melts into liquid water. Large systems can be used as seasonal storage to be charged during winter and discharged during summer to satisfy space temperature requirements. Smaller systems can be used to improve cooling

devices efficiency by charging during the night (lower cooly demand) and using the cooling capacity during the day [30].

Phase change material thermal energy storage systems (PCM-TES) are a wide family of materials that can be used as TES systems. PCMs can be classified into three main categories: organic, inorganic, and eutectic. Due to the large number of available substances, PCMs can cover different levels of operating temperatures, making them suitable for multiple applications. Important properties of PCMs employed for TES applications are high latent heat of fusion to minimise the size and high thermal conductivity to effectively transfer heat to the heat transfer fluid. Additional characteristics are limited volumetric capacity change, reversibility of the chemical reaction, stability, non-flammability, non-toxicity, low environmental impact, and cost. Organic PCMs have high storage density, with melting and freezing cycles and are stable, and recyclable. The main limitation is the low thermal conductivity which makes them not suitable for industrial applications. Instead, inorganic PCMs have high thermal conductivity, together with sharp phase changes, high latent heat and are not flammable. However, these materials are prone to corrosion, phase segregation and supercooling. Eutectic PCMs are alloys created by combining at least two compounds, organic and/or inorganic [31].

1.3.1.3 Thermochemical heat systems

Thermochemical energy storage systems (TC-TES) [32] use a reversible chemical reaction: the storage device is charged during a reversible endothermic reaction and discharged during an endothermic one. The heat stored is dependent on the mass of storage medium, reaction enthalpy and conversion degree. Some of the main materials and processes currently investigated are reviewed here [33].

TC-TES can be divided into two subcategories system: open and closed systems. While in open systems, the working fluid is released in the environment, in closed systems a heat-exchanger thermally connects storage to the environment. TC-TES devices offer different advantages such as higher energy densities and

extended temperature ranges compared to sensible and latent heat TESs, no heat losses and can be employed in long-term applications. As main downside, their increased complexity and cost are a limit for commercial applications.

1.3.2 Electrochemical energy storage

Electrochemical devices convert the chemical energy contained in its active materials, directly into electrical energy by means of an electrochemical oxidation-reduction. There are two main categories of electrochemical ESS: 1) standard batteries (BES) and 2) flow batteries (FBES). In BES the charge energy is stored in the two electrodes ("active mass") in a solid or semi-solid form and the electrolyte is used to conduct the ions, while in FBES the energy is stored in two electrolytes which are continuously pumped across the membrane connected to the electrodes [34].

1.3.2.1 Batteries

The basic elementary cell of a battery includes a negative and positive electrode (anode and cathode) and an electrolyte in between that only allows for ionic conduction and stops the electronic flow. Anode and cathode are electrically connected through an external circuit where the flow of electrons (current) can circulate. During the battery discharge, the anode is oxidised and electrons flow through the external circuit delivering a flow of current. The cathode receives the incoming electrons that activate a reduction reaction. The generated electricity is proportional to the chemical reaction rate at the electrodes according to the Faraday's law. Batteries can be divided in 1) primary batteries or 2) secondary batteries. The first types are non-rechargeable and are only employed for single use applications, representing around 20% of the entire battery market. Only the second types are rechargeable and can be used as storage devices for stationary applications. Although primary batteries can be employed in several applications due to their high specific energy density and low cost, this review focuses only on batteries used as ESS (secondary batteries). In the case of secondary batteries, the cell can be recharged applying an external

voltage that can reverse the electrochemical processes and restore the electrodes initial form. Batteries are composed of several cells, connected in series and parallel, to obtain the required voltage and current for the specific application.

Numerous types of batteries are available combining different electrodes and electrolytes materials; some of the most common battery technologies are lead-acid, lithium-ion, nickel-cadmium, sodium-sulphur, metal-air batteries and solid-state batteries and are briefly described in this paragraph. There are other batteries technologies under development or already available on the market, which can be found described in different review studies [12,35–37] .

Lead-acid (LA) battery are the oldest and most diffused electrochemical batteries. The anode is made of lead with a sponge-like structure and the cathode of lead dioxide. The two electrodes are immersed in a liquid electrolyte made of water and sulphuric acid with a water to acid ratio of 3:1. LA batteries can be flooded or valve-regulated, both characterised by the same electrochemical reaction but different construction, where valve-regulated batteries are equipped with a valve to regulate the internal pressure and avoid contact with air. The main advantages of LA batteries are the low capital cost combined with high specific power, good performance for a wide range of temperatures, availability in large quantities in a variety of sizes and designs, making them suitable and flexible for different environments and use cases. One major drawback is their limited life cycle and slow charging speed, not acceptable in applications where quick recharge times are crucial. Lead-acid batteries also have a high self-discharge rate, when not in use. Moreover, these batteries can be hazardous to the environment if not properly disposed and recycled [38].

Lithium-ion (Li-ion) batteries use graphitic carbon for the anode, lithium metal oxide for the cathode and inorganic dissolved lithium salt for the electrolyte. The main attractive characteristics of lithium-ion batteries are their light weight and high energy density, which make them ideal storage decides for portable and compact applications. Moreover, li-ion batteries have high efficiency, long

life cycle. Among some of the drawbacks of li-ion batteries is their high production cost, the need for special charging circuits to ensure proper charging and prevent overcharging or undercharging. These batteries are also sensitive to high temperatures, as extreme heat can lead to reduced performance, degradation, or even safety risks. Li-ion batteries also carry the risk of bursting or catching fire if mismanaged. Finally, complete discharge of lithium-ion batteries can lead to irreversible damage, reducing their overall lifespan [39].

Nickel-Cadmium (Ni-Cd) batteries have spongy nickel oxide anode, a cadmium cathode, and a potassium hydroxide electrolyte. Ni-Cd batteries have good performance in a wide range of temperatures, low operational costs, and fast charging capabilities. Despite their long shelf life (capability of being stored in a discharged state without significant loss of capacity), they have high self-discharge rates during normal operations. From an environmental standpoint, one significant disadvantage is toxicity of cadmium requiring proper disposal methods. This environmental concern limits their overall sustainability [40].

Sodium sulphur (Na-S) batteries are made of two molten salts-based electrodes: molten sulphur at the positive side, molten sodium at the negative side; for the electrolyte solid beta alumina is used. To maintain the cathode and anode in the liquid form operating temperature above 270°C is required. These batteries have high energy density and can provide high power with high conversion efficiency. They are also robust with the capability of undergoing numerous charge-discharge cycles without significant degradation. The main limitation of Na-S batteries is related to possible safety issues that may arise with Na-S batteries, due to the high operating temperature and the potential risks associated with the materials used [41].

Metal air batteries involve the utilisation of a metal with high energy density as a solid anode and oxygen as cathode. The O_2 is obtained from the outer ambient air often using a catalyst covering either a porous carbon structure or metal mesh. The electrolyte depends on the anode composition and normally consists of a hydroxide (OH-) ion conductor, such as potassium hydroxide, sodium

chloride or a non-aqueous solution. The most promising metals are lithium, magnesium, zinc, aluminium, sodium and iron [42].

1.3.2.1 Flow batteries

Flow batteries use the flow of liquid electrolytes to feed the electrochemical reaction. Typically, the two electrolytes are stored in external separate reservoirs and are pumped to reach the anode and cathode respectively. The positive and negative sides are separated by a membrane that only allows conduction of ion. The electrons released during the reaction flow from the cathode to anode during the discharge and vice versa during the charge [43]. The main FBES technologies are vanadium redox batteries (VRBs), polysulfide bromide batteries (PSB) and zinc bromide (Zn-Br) batteries.

Vanadium redox batteries exploit the ability of vanadium of existing in four different states (V^{2+}, V^{3+}, V^{4+} and V^{5+}). One tank contains a mixture of V^{2+}/V^{3+} to feed the anode and the other contains a mixture of V^{4+}/V^{5+} to feed the cathode. During the discharge, on the negative half-cell V^{2+} oxides into V^{3+} releasing one electron; on the positive half-cell V^{5+} oxides into V^{4+} receiving one electron. The two half-cells are connected by a membrane separator where H+ can pass through maintaining balance of charge.

Polysulfide bromide batteries use two other electrolytes: sodium polysulfide to feed the anode and sodium bromide to feed the cathode. A polymer membrane allows the sodium cations to pass through and stops the electronic flow. During the discharge, the polysulfide ions on the negative half-cell are reduced to sulphur; on the positive half-cell the bromide ions are oxidised to bromine.

Zinc bromide batteries use two different solutions of zinc and bromine placed in separate containers. During the discharge, the zinc ions on the negative half-cell are oxidised into zinc, while the bromide ions on the positive half-cell are reduced to bromine.

Flow batteries are suitable technologies for grid-scale energy storage, due to their high power, long duration, no self-discharge (the electrolytes are kept

separate when not in use) and fast response. Moreover, the big volumes required for the electrolyte tanks and pumping system are not an issue for stationary applications. Some drawbacks of these technologies are the low efficiency and complex flow control due to the external circulating pumps.

1.3.3 Chemical energy storage

Chemical storage can give good flexibility and high energy storage capacity especially for long term applications [36,59]. All the traditional carbon-based fuels, such as coal, gasoline, diesel, natural gas, liquefied petroleum gas (LPG), are a form of chemical storage. However, the scope of this review is to analyse chemical storage obtained from off-peak or excess of renewable power production ("power-to-fuel"). This is typically performed by an electrolyser that produces hydrogen, splitting water H_2 and O_2 by means of an electrolysis reaction. Electrolysers show rapid response and can also be used to provide ancillary services by matching fluctuating demand signals. Hydrogen is an energy vector nowadays mainly used in industrial processes for refining petroleum, treating metals, to produce chemicals or for steel production. As shown in Figure 1-7, in 2020, about 90 Mt H_2 have been consumed, of which 45 Mt H_2 to produce chemicals, mainly ammonia (around three-quarters of the total), used as fertiliser and methanol (around one-quarter), used for the manufacturing of polymers, and nearly 40 Mt H_2 in refineries. The residual 5 Mt H_2 was employed for steel production using the direct reduction of iron (DRI) method, where hydrogen is used to reduce iron pellets into sponge iron, which can then be processed to form steel [44].

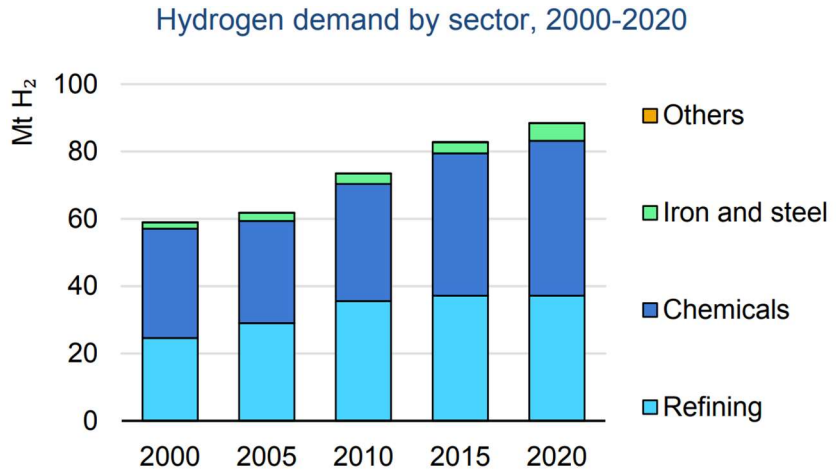

Figure 1-7. Hydrogen use by sector [44].

The current production pathways of hydrogen are summarised in Figure 1-8 [45]. Hydrogen generation technologies are increasingly categorized using a color-coded system:

- "Grey" (or "brown/black") hydrogen, derived from fossil fuels, predominantly natural gas and coal. This is the most common and cheapest type of hydrogen. However, this process releases carbon dioxide into the environment. The traditional mechanism for hydrogen production from methane is the steam-methane reforming (SMR) process. This reaction uses natural gas and steam to break the CH_4 atoms bonds and obtain H_2. Autothermal Reforming (ATR) is a method utilized to generate syngas, which consists of hydrogen, carbon monoxide, and carbon dioxide. The technical maturity of the partial oxidation process for hydrogen is well-established. In this method, oxygen is introduced to the raw materials, natural gas or heavy hydrocarbons like fuel oil or residual oils from petroleum processing. Finally, gasification is a thermal process that transforms carbon-based fuels (organic or fossil-based) at elevated temperatures (>700°C). This occurs without combustion, employing a

regulated quantity of oxygen and/or steam to produce carbon monoxide, hydrogen, and carbon dioxide.

- "Blue" hydrogen is an alternative option to limit these CO_2 emissions by using carbon capture or thermo-catalytic decomposition. Therefore, this type of hydrogen is considered a carbon neutral alternative.

- "Green" hydrogen, is a more sustainable form of hydrogen which is obtained from renewable energy either from electrolysis using the excess of electricity or from biofuels with the same thermochemical processes used to produce the "grey" and "blue" hydrogen.

- "Yellow" (or "purple") hydrogen is generated when electrolysers are powered by electricity sourced from nuclear power plants.

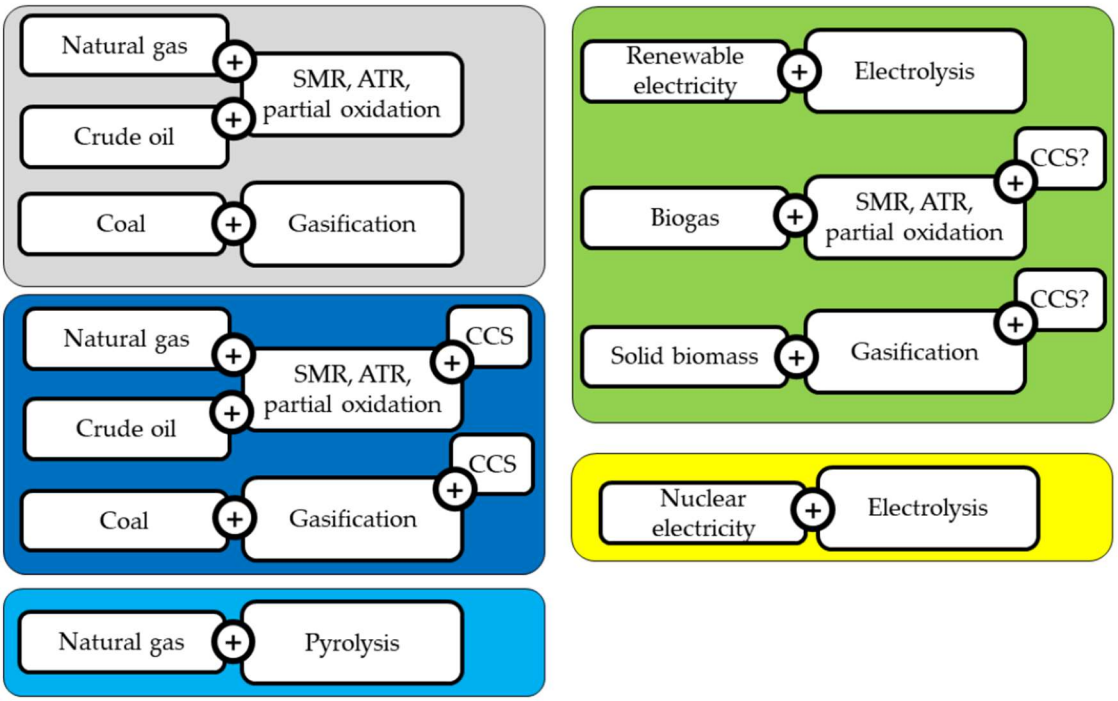

Figure 1-8. Hydrogen production pathways divided in colours [45].

Considering the current need of H_2 in the industrial sector, the substitution of the "grey hydrogen" with water electrolysis represents the best application in the short term. However, due to the increase of renewable energy sources and

the need for decarbonisation, H_2 needs to be employed more broadly in the energy sector, to fuel traditional generator such as gas turbines, combined cycles, or new generators such as fuel cells to re-convert the chemical energy into electrical ("fuel-to-power") [46]. Hydrogen generation from water electrolysis, currently has higher costs than fossil-based solutions, the expected learning curves for both RES electricity generation and electrolysers could make it a viable solution in the next decades as reported in Figure 1-9 [45].

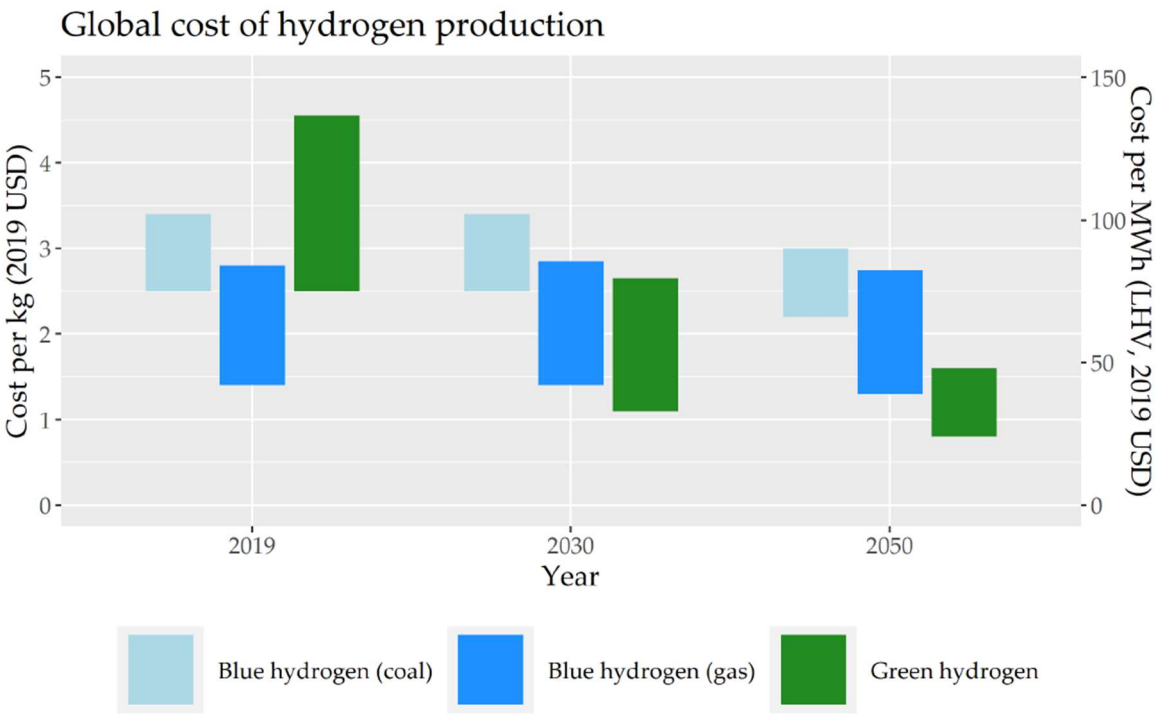

Figure 1-9. Estimation of future hydrogen costs for different pathways [45].

There are three main technologies available to produce hydrogen through electrolysis: alkaline electrolyses (AEL), polymer electrolyte membranes (PEM) and solid oxide electrolysers (SOEC) [47]. Alkaline electrolysers are based on a traditional technology that appeared at the industrial scale at the beginning of the 20th century. Among their advantages there are low cost, reliability and durability, and the capability to operate at high pressure. Although pressurised AELs have lower efficiency than the atmospheric electrolysers, they immediately provide pressurised H_2, reducing the compression work required after the reaction to pressurise the gas. This overall results in higher efficiency.

The main drawbacks are their large size, modest current density and not appropriate for transient power sources. Although AELs can operate part-load between around 20 - 100% of design conditions, fluctuations of electricity are not handled well. In addition, cold start-ups are slow and can require from minutes to hours. In AELs the electrodes are immersed in a highly concentrated alkaline solution (KOH or NaOH). A porous solid material separates the electrodes and allows for the hydroxide ion transport. The electrodes materials should have good corrosive resistance, high electronic conductivity, and high catalytic activity. Generally, nickel or nickel-based compounds are employed: for the cathode, either nickel or nickel-sulphur alloys and for the anode, nickel plates combined with a porous layer of nickel or a nickel-iron alloy.

Polymer electrolyte membranes are newer technologies and appeared in 1970s. PEM operate safely at high pressure with good performance during part-load and intermittent operation. The startup is also quicker, in the order of seconds-minutes required. PEM can offer higher current density and purity than AELs electrolysers. The higher current density results in a more compact structure. This is due to the proton-conducting membrane used as the "solid" electrolyte. Due to the acid environment required for the reaction, platinum-based electrocatalysts are employed. Both the required membrane and the need for platinum makes this technology more expensive.

Among the electrolysers technologies, solid oxide electrolysers are the newest and still at the laboratory stage. Nickel-YSZ (yttria-stabilised zirconia) cermet is mainly used for the cathode electrode and perovskite ceramic materials for the anode. At the electrolyte YSZ or ScSZ (scandia-stabilised zirconia) can be used. The SOECs operate at high temperature (between 600 to 1000°C) reducing the required electrical energy to split the water atoms. The efficiency of these electrolysers is around 90% and can theoretically reach 100% when using excess heat (endothermic mode). Despite the high electrical efficiency and the possibility to be coupled with waste heat recovery systems, SOEC have several drawbacks: long startup times, non-suitability for intermittent demand, fast

degradation of cell components, mechanical instability due to thermal stresses and the high cost.

Hydrogen is the fuel with the highest energy content per unit mass with a low heating value LHV = 119.96 MJ/kg. Despite this, there are some limitations related to the low volumetric energy density both in gaseous and liquid states. In addition, the more energy dense liquid form is difficult to obtain due to the low boiling temperature (T= -252.9°C, at standard ambient pressure). This means that complex cryogenic systems are required. Furthermore, since liquid hydrogen can evaporate quickly, the container must be properly insulated. Regardless of the application, the boil-off issue of liquid hydrogen is the result of its evaporation, mainly caused by heat leakages into the cryogenic tank. While various approaches exist to reduce or recapture the evaporated gas, in numerous cases, hydrogen remains unused, leading to fuel loss into the atmosphere and the consequent waste of energy [48]. Hydrogen has a low electrical conductivity, meaning that the agitation of hydrogen molecules may result in electrostatic charges, that require related equipment to be properly grounder to avoid spark productions. Hydrogen has low ignition energy (0.02 MJ), despite the high autoignition temperature (585°C). The flammability range is the widest among all the fuels: from 4% to 75 %. Another issue related to hydrogen is the embrittlement phenomenon, which makes metals become brittle and lose their ductility due to the introduction and diffusion of hydrogen into the material. The combination of these chemical properties make the storage and distribution of H_2 highly unpractical and expensive [49]. The main methods for hydrogen storage involve hydrogen compression into tanks (pressure range of 350 bar - 700 bar), cryogenic compression and liquefaction into tanks, metal hydride storage and underground storage. The liquefaction of H_2 is energetically demanding, with technical limitations such as unstable pressure, gas leakages and expensive insulation. The underground storage is only suitable for long term storage. Therefore, the most common storage techniques are the use of pressurised hydrogen tanks and metal hydrides. Metal hydrides are formed

when metal atoms bond with hydrogen to form stable compounds. Compressed hydrogen is best suited for large-scale applications, while metal hydride is more efficient in small-to-medium scale energy storage systems, since they can store a large amount of hydrogen per unit volume [50].

Alternatively, fuels with higher energy density (higher hydrogen content per unit of volume) can also be used as hydrogen carriers, being methane, methanol and ammonia the main candidates [51]. Methane (CH_4) can be synthetised from H_2 and CO_2 according to the following global exothermic reaction (Eq. (1-1)):

$$CO_2 + 4H_2 \rightarrow CH_4 + 2H_2O \qquad (1\text{-}1)$$

The methanation reaction can be both biological and chemical-catalytic. The catalysts of the biological methanation are methanogenic microorganisms while the catalysts of the chemical-catalytic reaction, also known as the Sabatier reaction, can use metals such us Ni, Ru, Rh and Co, being nickel the most performing among them. Typical reaction temperatures are in between 250°C to 550°C range and pressures between 1 to 100 bar.

Methanol (CH_3OH) can also be produced combing H_2 and CO_2 according to this other less exothermic reaction (Eq. (1-2)):

$$CO_2 + 3H_2 \rightarrow CH_3OH + H_2O \qquad (1\text{-}2)$$

The process requires a unique catalyst material like $Cu/ZnO/Al_2O_3$, where methanol is formed at temperatures between 250°C to 300 °C and pressures between 50 to 100 bar. Methanol is a liquid at ambient conditions and therefore easy to store. Both methane and methanol production are interesting solution for recycling of CO_2.

Ammonia (NH_3) can also be synthetised from green H_2, but it is instead carbon-free. NH_3 can be obtained from H_2 and NH_3 according to this other exothermic reaction (Eq. (**1-3**)):

$$N_2 + 3H_2 \rightarrow 2NH_3 \qquad (1\text{-}3)$$

This process is also known as Haber-Bosch reaction where nitrogen and hydrogen react at high temperature and pressure (between 300-500 °C and 140-250 bar), thanks to an iron-based catalysts. Ammonia is relatively easy and cheap to store and transport due to an easier and less energy intense liquefaction: ammonia is a gas at standard ambient conditions but can be liquefied at ambient pressure with temperatures below -33°C and at ambient temperature with pressures above 20 bar. Despite being a toxic substance the procedures and standards for safely manage ammonia are already well-known by the experience of the chemical industry [52].

Finally, liquid fuels (mostly straight-chain alkenes) such as e-kerosene can be obtained through the Fischer-Tropsch process [53], where, carbon monoxide and hydrogen in the syngas are converted into liquid hydrocarbons in the presence of catalysts, typically at temperatures of 150-300°C and pressures of one to several tens of atmospheres, according to the following global reaction (Eq. (1-4)):

$$(2n + 1)\ H_2 + n\ CO \rightarrow C_nH_{2n+2} + n\ H_2O \qquad (1\text{-}4)$$

where n is typically 10–20.

1.3.4 Mechanical energy storage

Mechanical energy storage systems convert the electricity in a form of mechanical energy such as pressurisation or liquefaction of gas, kinetic or potential energy. The main examples of mechanical energy storage systems are pumped hydro (PHES), flywheels (FES), and compressed air storage systems (CAES).

1.3.4.1 Pumped hydro energy storage

Pumped hydro energy storage systems are the most widespread systems among all the mechanical ESSs, catheterised by high energy capacity, efficiency and long storage periods. PHES systems exploit the different elevation of two water

reservoir: during the charging process, water is pumped from the low reservoir to the upper reservoir; during the discharging process, the stored water is released through turbines following the same mechanism of conventional hydro stations. PHES is one of the most cost-effective utility-scale options for grid energy storage, suitable for providing ancillary services such as providing reactive power support to frequency control, synchronous or virtual inertia. Other key features of PHESs are the absence of pollutant production during operation, low operational and maintenance costs. The disadvantages of pumped hydro energy storage systems are the strong geological limitations by requiring two interconnected water reservoirs at different heights which is not always feasible and the strong landscape impact for the construction of the plant, such as natural habitat destruction and water quality change [54].

1.3.4.2 Flywheels

A FES system consists of a rotating solid massive cylinder (flywheel) inside a vacuum chamber, magnetic bearings, an electrical motor/generator with power conditioning devices. The energy is stored in the form of kinetic energy: during charging, electricity is used to drive the motor that spins the flywheel, while during discharging the motor acts as a generator converting the kinetic energy back into electricity. FES can reach rotational speed up to 10^5 rpm, requiring a strong containment in case of mechanical failure, due to the consistent forces involved. The magnetic bearings are used to support the cylinder through magnetic levitation. This and the vacuum chamber are required to reduce friction losses. Flywheels are highly efficient, long lifespan, high power density, fast time response, reliable, safe and with minimal environmental impact. However, flywheels have a restricted energy storage duration (order of minutes), which means they are best suited for rapid and time-sensitive tasks. Consequently, flywheels are primarily employed for the regulation and optimisation of systems instead of providing long-lasting energy autonomy [55].

1.3.4.3 Compressed air energy storage

The working principle of CAES is based on a Brayton cycle where compression and expansion are decoupled in time. An excess of renewable energy, typical of off-peak hours, can be used to power the compression system. The compressed air can be stored and then expanded in a turbine group to satisfy the electrical demand during peak hours [56]. The amount of compressed air is dependent on the volume, pressure and temperature of the storage vessel.

Different types of compressed air energy storage systems have been extensively investigated. Diabatic-CAES (D-CAES) is the simplest among the CAES technologies as the heat developed during compression is dissipated into the environment. Before the expansion, thermal energy is typically added through a combustion process to increase the electrical power output of the turbine [57,58]. D-CAES systems have relatively simple installation and control procedures and have the capability to work as a standard gas turbine when the compressed air storage is fully discharged, providing continuous power supply. The first two ever implement CAES plant are diabatic systems: the 290 MW Huntorf plant in Germany installed in 1978 and the 110 MW McIntosh plant in Alabama installed in 1991. This second plant was also equipped with a recuperator to pre-heat the air before entering the combustor using the turbine exhaust gas.

To eliminate the dependency on the fuel, reduce thermal losses and improve the conversion efficiency, adiabatic-CAES (A-CAES) solutions have been proposed. A-CAES systems can store the generated heat during the compression directly into the storage tank or by employing a TES system [59–61]. The advantage of the former case is that the air does not require to be reheated before the expansion. However, the storage vessel needs to be larger and manufactured with more expensive materials. In addition, pressure ratios are limited since the compressed air is not cooled. In the latter case, heat is not wasted but stored in the TES during the charging phase and it is released during the discharge. This

reduces the tanks size and improves the round-trip efficiency. In general, the increase in efficiency and the elimination of CO_2 emission are obtained at the expense of higher costs and plant complexity due to the presence of a TES system.

Isothermal-CAES (I-CAES) systems have also been considered with the aim of eliminating the combustion process and the TES system at the same time, with potential benefits on both costs and efficiency [62]. Nearly isothermal compression and expansion can be obtained by using liquid pistons or hydraulic pumps/turbines, exploiting the higher thermal capacity of liquids. However, slow compression/expansions are required to leave sufficient time for the heat transfer exchange, which makes this not suitable for industrial applications. Faster processes can be obtained by introducing liquid or foam drops inside the air, but these solutions are not yet ready for a commercial use [63].

An alternative option, namely second generation CAES (S-CAES), integrates the compression and storage systems with a standard gas turbines [64–66]. During off-peak hours, when electricity demand is low, surplus electricity is used to compress air and store it in underground caverns or above-ground tanks. When electricity demand is high, the compressed air is released from the storage tanks and expanded through a gas turbine. In addition, the total plant efficiency can be improved by heating and expanding the stored compressed air in a topping air expander before the injection into the micro gas turbine. The advantages of this system are the lower capital costs, possibility to always satisfy the energy demand. Despite the benefits in terms of fuel savings and increased power outputs, the main drawback of this system is the need of a fuel.

1.4 Distributed Generation

The current energy scenario is not only changing in terms of energy mix but also on the structure of power plants layout which is moving from a hierarchical and supplier-centric structure towards a more decentralised and consumer-centric

structure (Figure 1-10). This is because, the adoption of distributed generation systems can support a cleaner and more efficient energy production compared to traditional centralised power plants and can improve the exploitation of RES [67].

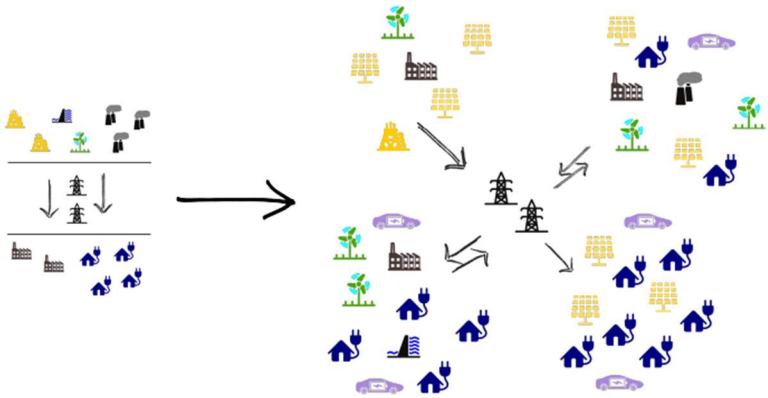

Figure 1-10: Change on the electrical power network from centralised to decentralised structure [68]**.**

The use of small-scale generators close to the consumers can significantly improve energy conversion efficiencies due to the possibility to maximise local power production, reduce transportation and conversion losses and extensively employing cogeneration or trigeneration. Some of the DERs benefits are the better exploitation of RES and other energy-efficient solutions such as combined heat and power (CHP) units, reduced transmission losses, increased control and energy security for local communities, the possibility to provide electricity in remote rural areas and cost-effectiveness for small-scale projects [67]. Distributed prime movers, with different characteristics, both programmable and non-programmable, can be grouped in microgrids (MGs) to combine their benefits and exploit all their potential [69]. However, the integration of microgrids into the existing grid infrastructure also comes with several challenges on the management of generators with different requirements, especially if the microgrid includes CHP units that are required to satisfy not only the electrical demand but also the thermal needs of a nearby istrict heating network (DHN). These criticalities make energy storage systems essential for microgrids efficient operation. ESSs can help balance mismatches between

electricity supply and demand, optimising the use of distributed energy sources for efficient energy use and decoupling electrical and thermal energy production in case of CHP plants [70]. In addition, energy storage systems can also improve the reliability and resiliency of the grid when employed as backup power during possible outages [16].

Microgrids can operate in two different configurations: parallel or islanded mode. The advantages of one mode compared to the other, depend on different factors such as location of the consumers, availability of resources and economic scenario. Under parallel (or on-grid) operation, the microgrid is connected to the primary central grid, allowing electricity imports and exports according to the specific needs of the grids. This configuration can provide several benefits to both the micro and primary grid: the microgrid can sell energy and provide ancillary services to the main grid, but at the same time the connection to the main grid allows for more reliable energy to the local end-users. ESS have a fundamental role in ensuring that microgrid can provide different services to their consumers especially if a considerable part of renewable generators is present. ESSs have a great potential for increasing the utilisation of local resources and reduce transportation losses, reducing import and export with the main grid. Under islanded (or off-grid) operation, the microgrid does not rely on the connection with the primary grid. The typical end users of islanded microgrids are remote communities or islands, where the connection to the national grid is unfeasible from the economical and practical perspectives. In this configuration, ESSs have the important role of contributing to the provision of secure energy to the local users by maintaining the frequency and voltage stability through regulation of the real and reactive power output.

1.5 Micro gas turbines

In the growing decentralised market, micro gas turbines (mGTs) are interesting technologies due to due to their high efficiency in combined heat and power (CHP) applications, low vibrations and noise levels, quick response, fuel

flexibility, low maintenance costs, modularity and compact size [71–73]. In particular, the ability of mGTs to quickly vary power output is an important asset when used in combination with intermittent renewable energy sources. Micro gas turbine also offer possibility for hybridisation with renewables and energy storage systems. Traditional micro gas turbines are based on carbon-fuels, typically natural gas. However, due to their fuel flexibility in the future it could be possible to utilise them with green fuels such as hydrogen or ammonia to re-convert the stored chemical energy into electric energy [52,74].

Micro gas turbines are small prime movers providing power in the range of 30 kW to 250 kW. Similarly to traditional gas turbines, mGTs operate according to the Brayton cycle. However, there are several characteristics that differentiate large gas turbine from micro gas turbines. Micro gas turbines operate at high and variable rotational speed (60000-120000 rpm) requiting variable-speed permanent magnet generator. The typical operating pressure ratios are small (in the 2-5 bar range), this makes the radial compressors and turbines more suitable than axial devices. The turbine inlet temperature is also moderate, typically below 1000 °C, as turbine blade cooling is usually unpractical due to the small size of the machines. The low operating pressure and temperature, together with the general small size of mGTs result in a lower electrical efficiency, around 17 %, in a simple Brayton cycle. Therefore, to increase the electrical efficiency, up to around 30 % (for sizes around 100 kW of electrical power output), recuperated cycles are typically used. Despite the relatively low electrical efficiency, mGTs are normally employed in cogeneration cycles reaching an overall efficiency of around 80% [71].

1.6 Micro gas turbines integrated with ESSs

This review is focusing on the energy storage devices that, when integrated with a micro gas turbine device, require a retrofitting and or change of operation of the device compared to standard operation, use of alternative fuels (mainly hydrogen and ammonia) and the coupling with compressed air storage systems.

1.6.1 Micro gas turbines fuelled with hydrogen

Micro gas turbines are interesting solutions for reconverting in electrical energy the energy stored in the hydrogen molecules. Various experimental studies have been conducted with blends containing low concentrations of H_2 (around 10/15% in vol) in blend with natural gas to demonstrate the feasibility on commercial micro gas turbines [75,76]. However, the combustion of hydrogen in blend with natural gas at higher concentrations shows several issues because of the different combustion characteristics compared to conventional fossil fuels, for example higher LHV, higher reactivity, flame speed and burning velocity. Therefore, different research activities have been conducted with a focus on combustion CFD modelling to improve its efficiency, stability and reduce NOx emissions [74,77,78].

Several numerical and experimental activities have been conducted with blends containing low concentrations of hydrogen to demonstrate the feasibility of their use on commercial micro gas turbines [60,61]. For the original T100 combustor, it was proved that concentrations of up to 10% of H_2 in volume can be used without a re-design of the combustion chamber. Calabria et al. [60] performed a CFD analysis on the original T100 combustor operating with different concentrations of hydrogen in blend with methane. The analysis showed that it is possible to operate with 10% of H_2 in volume even at part load, while higher amounts can lead to flashback issues. The safe operation at 10% of H_2 in volume was also demonstrated experimentally by Reale et al. [72]. The use of hydrogen for higher concentrations presents several challenges due to the different combustion characteristics compared to conventional fossil fuels, such as higher low heating value (LHV), higher reactivity, flame speed and burning velocity. Therefore, different studies have been conducted with a focus on combustion computational modelling to improve its efficiency, stability and reduce NOx emissions [15,62,63]. For example, Cappelletti et al. [15] proposed a CFD-based redesign of the T100 combustor fuelled with 100% H2. Devriese et al. [73]

investigated the possibility to use a micromix geometry to reduce NOx emissions.

1.6.2 Micro gas turbine fuelled with ammonia

Ammonia combustion has also to overcome different issues related to the low LHV, low reactivity, high ignition energy and low laminar burning velocity [79]. Therefore, initial studies were mainly focusing on studying blends containing methane and hydrogen, where the latter can be obtained from ammonia pre-cracking. Valera et al. [80] identified narrow equivalence ratios for stable combustion with CH_4 – NH_3 and H_2 – NH_3 blends on a generic swirl burner. Rocha et al. [81] investigated the combustion properties of different ammonia blends in a porous burner. Although most of the research activities are dealing with generic burners to improve stability and reduce NO_x emissions, some projects are in place to reach 100% ammonia on micro gas turbine combustors [82]. Researchers of the National Institute of Advanced Industrial Science and Technology (AIST) were able to operate a 50 kW micro gas turbine fired with ammonia-kerosene blends substituting the original combustor with a diffusive bi-fuel combustor [83,84]. After that, they also demonstrated the operability of the same micro gas turbine fired with pure ammonia, utilizing a two-staged rich-lean burner [85,86]. However, one of the limitations is the production of high NO_x emissions that required a separate gas after-treatment systems for their abatement. After that, they were also able to fire the micro gas turbine with pure ammonia thanks to a two staged rich-lean burner [85,86]. However, one of the limitations was the production of high NOx emissions which make essential the use of a selective catalytic reactor (SCR) for the reduction of NOx to acceptable limits.

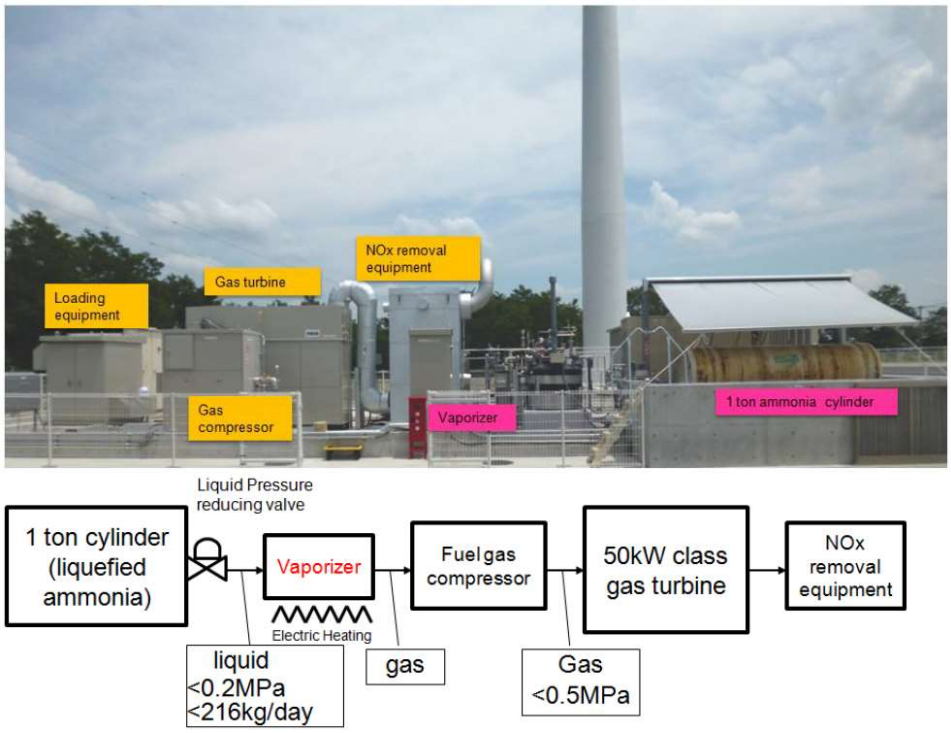

Figure 1-11: Facility of the ammonia micro-GT [83,84].

1.6.3 Micro gas turbines and small-size S-CAES

Compressed air energy storage systems for small-size applications can be integrated with commercially available mGTs (small size second generation CAES or small S-CAES). While large size systems require to be placed closed to natural caverns due to the high volumes required for the air storage, in small CAES system air can be simply stored in artificial tanks (man-made, not natural), eliminating the dependency on geological formations. Compared to other storage solutions, such as batteries, small CAES systems are not susceptible to high temperatures, have lower capital cost and longer lifespan [87]. Distributed CAES is also suitable for cogeneration or trigeneration, thanks to the heating and cooling power obtained during compression and expansion [88–90]. In addition, the lower capital and installation costs of small-size CAES systems make these systems more accessible to a broader range of customers [65].

Typically, two different solutions are possible [65] as illustrated in Figure 1-12: 1) the compressed air can be directly injected at the exit of the mGT compressor or 2) the compressed air is pre-heated and expanded in an additional expander before being injected into the mGT to exploit the pressure difference between storage vessel and the mGT injection point.

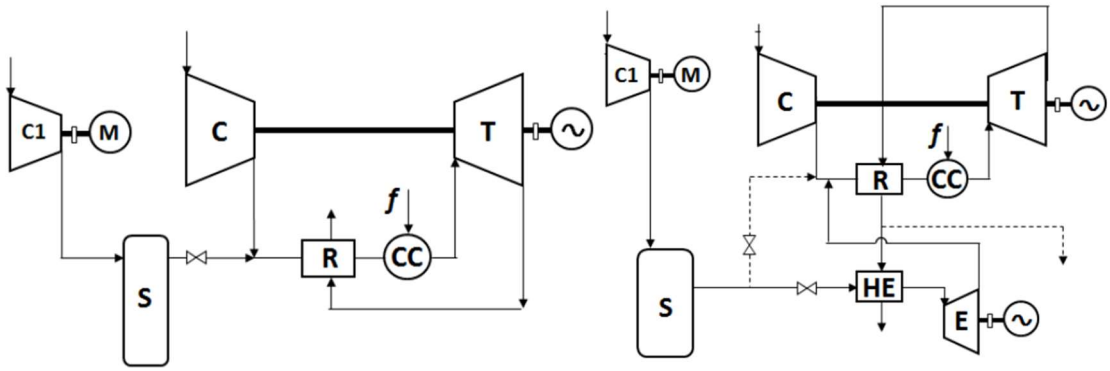

Figure 1-12: CAES air injection (left) and CAES air injection/expander (right) [65].

Despite the reliability and flexibility, the S-CAES mass flow discharge rate is limited by the specific mGT capabilities to handle an increased mass flow rate at the expander. These limitations are mainly related to the structural limits of the machine, combustion performance, possible thermal gradients and compressor instabilities. Especially during transients, thermal gradients and reduced surge margin [64,65] can decrease the system flexibility and limit the mGT operating conditions. Most published works on small-size CAES focus on design optimisation, techno-economic analysis and energy management within microgrids [91–93]. In addition, few analyses have been performed on second-generation small CAES systems. Salvini [65] studied an S-CAES system based on a 4600 kW Mercury recuperated gas turbine, demonstrating that a 30% maximum power augmentation can be obtained during the discharging phase with the safe operation of the machine. Arnulfi [64] considered a 100 kW mGT with a similar S-CAES configuration, estimating the maximum mass flow that could be injected in the mGT. Both these studies were based on steady-state off-design models, neglecting the time-dependent performance and constraints.

Some dynamic studies have been carried out, but mainly concerning A-CAES systems. Jin et al. [94] considered an A-CAES used to reduce fluctuations generated by wind power production. Mucci et al. [95] analysed different control strategies to increase the system performance during off-design conditions by regulating the compressor speed and the throttling valve opening during the charge phase.

1.7 Work motivation and thesis highlights

This thesis aims to analyse the integration of micro gas turbines with the following energy storage systems: compressed air energy storage (CAES), chemical energy storage (using hydrogen and ammonia), battery storage, and thermal energy storage. The studies conducted and the obtained results are presented and discussed in separate chapters:

- **Dynamic modelling of the T100 micro gas turbine**

  The aim of this chapter is to present the main characteristics of the T100 micro gas turbine and its dynamic model which will be used in the following chapters for the integration with the CAES system and when injecting H_2-NG and NH_3-NG blends. Two models are presented: the former was already validated in a previous study at the Vrije Universiteit Brussel (VUB) and will be used for the following analyses of the other chapters, the latter was validated against experimental activities conducted on the T100 of the Innovative Energy Systems (IES) laboratory of the Savona Campus of the University of Genoa.

- **Steady-state and dynamic analysis of the T100 integrated with a small-size CAES system**

Starting from background on design and management optimisation, this work proposes dynamic simulations and definition of operational constraints, not

available in previous publications. These are important results to extend the system range (producing efficiency and cost benefits), avoiding risks and failures in prototypes or commercial applications. Special attention is devoted to the discharging of the air storage vessel because the increment of mass flow at the turbine expander can lead to surge margin decrease and thermal stresses, especially during dynamic operations. Maximum limits for the air injection are obtained and different operational strategies are considered to ensure safe operation during the system dynamics, enlarging the application range or proposing modifications in the control system. The fact that this work regards a commercial micro gas turbine (the T100) for extending its application range considering the integration with the CAES system means that the results obtained in this work can have fast commercial application in real CAES/mGT plants with an important positive impact for sustainable energy generation coming from average efficiency increase of a system suitable also for alternative fuels (e.g., biogas, hydrogen [32], etc.) or applications in concentrated solar systems [33]. This is an important innovation considering that the most recent papers on CAES systems in dynamic conditions refer to large plants connected with caverns [34] (in some cases with compressing and expanding systems operating on different shafts [35,36]) and the attention is mainly related to the charging/discharging dynamics [37]. When the surge margin limitation is taken into account (e.g., in [38]), no specific dynamic results are reported and since compressors and turbines are on different shaft, results are not able to cover the air injection issues in a commercial microturbine.

- **Steady-state and dynamic analysis of the T100 with fuel composition change**

The aim of this chapter is to analyse the effects of fuel composition change on the performance and dynamic behaviour of the T100 micro gas turbine. Although the current research effort is mainly focusing on improving combustion performance with alternative fuels, there is a lack of studies about the impact of different compositions of alternative blends at a system level on

the steady-state performance and transient behaviour. These aspects are important when considering the possibility to retrofit a micro gas turbine for flexible operation with different fuel blends. In particular, dynamic analysis is required to investigate the effects on key performance parameters to ensure safe operation of the mGT in all the working conditions, including transient operations. To date, few analyses have been carried out, but mainly considering the effect of different biogas compositions or small percentages of hydrogen blended with natural gas. For example, Zheng et al. converted a 2 MW natural gas fired gas turbine to operate with biogas concentrations. Transient manoeuvres during load increase and load shedding were performed to investigate the effect of fuel type on overspeed, surge margin, fuel mass flow and settling time [133]. Zornek et al. analysed the behaviour of a modified T100 operating with a new flameless oxidation combustor, experimentally demonstrating safely operation with different biogas composition during start-up and steady-state conditions [134]. Gaeta et al. performed an experimental and dynamic study of a T100 fuelled with methane and small percentages of H2 (~10% mol), within a hybrid power plan including hydrogen production and storage [99]. Therefore, it is necessary to analyse the effect of carbon-free fuels, such as hydrogen and ammonia, for wider operating ranges.

During transient operation, the use of fuels with a low LHV requires an increased fuel mass flow that can potentially reduce the compressor surge margin. Conversely, sudden composition changes of high LHV fuel can cause temperature peaks, detrimental for the turbine and recuperator life. A transient analysis with injection of hydrogen and ammonia was performed to monitor the main performance parameters with the aim to (i) verify compressor safe operations during different working conditions and (ii) to identify appropriate fuel composition change schedules to ensure turbine outlet temperature values within an acceptable range, while keeping the original fuel control system.

- **Energy management of the T100 integrated with energy storage systems**

This chapter focuses on developing an energy scheduler for different plant layouts based on the integration of the previously analysed T100 with different energy storage systems (TES, BES, CAES and power-to-H_2 system). The operational limits identified with the dynamic model of the T100 are essential for conducting and justify this final optimisation. For a complete analysis, it was required to verify that these new operating conditions could be safely reached also during transient operations.

Managing energy produced by different generators and using different energy storage devices can pose significant challenges, especially in cogenerative plants. There are different possible approaches for managing a microgrid [13]. Typically the following different steps are considered [96]:

1. *Day-ahead scheduling* (timescales: ~ 30 minutes/1 hour): it represents an offline optimisation to estimate the scheduling of the energy systems the day before the operation. This step is crucial in providing a high-level indication of the plant operation for the following day. Although this study focuses on the management of an existing plant, this same optimiser could also be used to assess the plant economic feasibility and optimal sizing if the capital costs and different representative days are considered over the plant lifetime.
2. *Intermediate control* (timescales: ~ 5-15 minutes): this represents the online Energy Management System (EMS) that readjusts the optimal setpoints considering updated forecasted conditions (i.e., new energy demands, prices and ambient conditions) and energy storage systems state of charge (SOC). The optimisation is performed over a future window (typically a day), and it is essential to reschedule the energy storage systems operation correctly. The approach is the same as the offline scheduler, but in this case, the optimiser is updated with the new forecasted and SOCs. In this case, although the optimisation is performed over a future optimisation window, the returned

outputs set points are the only ones referred to the immediately following time step.

3. *Real-time adjustments* (timescales: seconds): this is also an online control, but it is used to compensate for errors between real demand and the EMS signal. Typically, PID controllers or more complex model predictive controller (MPC) can be used for this.

In this chapter, a MATLAB optimisation tool is developed to calculate the offline optimised energy scheduling, which could be used for a day-ahead planning of the plant (step 1). The aim is to find different optimal operative strategies considering different fixed plant layouts. The sizing of the plants considering the components CAPEX could be considered in future studies. In general, the work conducted in this thesis provides the bases also for the future development of the other 2 control steps. In detail, this optimisation tool, properly modified, could be used as online EMS (step 2), due to its fast computational time (below 5 minutes). Regarding the real-time adjustments (step 3), the linear ramps obtained from the previous dynamic analysis could be implemented within the control system to guarantee the plant safe operation.

2 Dynamic modelling of the T100 micro gas turbine

The scope of this chapter is to describe the main features of the Turbec T100 (now AE-T100) micro gas turbine and the respective TRANSEO dynamic model, an in-house tool for the modelling of energy systems dynamics. This model will be used in the following chapters to test the performance and dynamic behaviour of the mGT integrated with a small size CAES system and fuel composition change using H_2-NG and NH_3-NG blends. In detail, two T100 dynamic models are considered in this chapter:

- The first model was already previously validated based on a work conducted at the Vrije Universiteit Brussel (VUB) facility. This first model will be extensively used for the detailed dynamic analysis in the following chapters.
- The second model was validated against experimental activities conducted on the T100 of the Innovative Energy Systems (IES) laboratory of the Savona Campus of the University of Genoa. This second model was validated both during regular operating conditions and with air injection after the compressor. The air injection is representative of the mGT operation during the discharge of a CAES system. This second activity main goal was to verify that the TRANSEO model could effectively reproduce the T100 behaviour also during air injection.

The second model was not used for the dynamic analysis with the integrated energy storage systems due to the lower maximum power output of the specific machine, caused by some modifications of the original machine of previous activities. Instead, the first model was used for the extensive analysis to capture a wider range of operating conditions.

2.1 Turbec T100 general specifications

The Turbec mGT company was originally a division owned by Volvo and ABB, and it is now under the ownership of Ansaldo Energia (now the machine is AE-

T100). This micro gas turbine (Figure 2-1) is a compact single shaft mGT for CHP applications that provides in nominal conditions an electrical and thermal power output of 100kW$_e$ and 165kW$_{th}$ respectively, with an electrical efficiency of 30% and overall cogeneration efficiency of 80% [97]. The T100 works according to a recuperated cycle (Figure 2-2) to increase its electrical efficiency.

Figure 2-1. Turbec T100: whole unit (left), inside view (right).

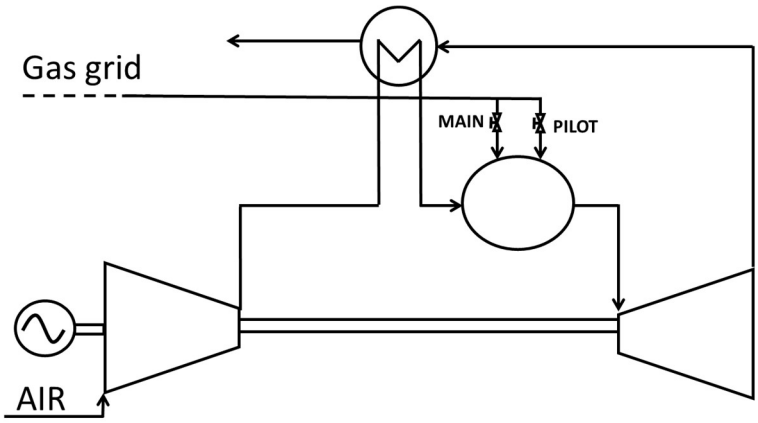

Figure 2-2. Turbec recuperated cycle scheme.

The main components are a single stage radial compressor and turbine, a recuperator, a tubular combustor, a high-speed generator, and auxiliary units. The compressor and turbine operate with pressure ratios around 4.5. The turbine inlet temperature is around 950 °C. The shaft, mechanically connecting

the compressor and turbine, can reach a maximum speed of 70000 rpm. The T100 traditional combustor is fired with natural gas, where a small percentage of fuel is provided by a pilot line, while the remaining is injected into the main line to operate the combustor in lean conditions. The fraction of natural gas injected in the pilot is used to ensure flame stability. The control system is designed to maintain the Turbine Outlet Temperature (TOT) constant and equal to 645°C, in the operating range considered in this thesis (around 40 kW_{el} - 100 kW_{el}). This TOT value ensures a good electrical efficiency – typical of similar-sized mGTs - while preserving the recuperator life, sensitive to high temperatures and thermal gradients. While at low load and especially at low ambient temperature, when the TOT does not reach 645 °C the control system varies the power output regulating the rotational speed.

The mGT main specifications at full load are summarised in Table 2-1 and are referred to an ambient temperature of 15 °C [98].

Table 2-1: T100 nominal specifications.

Parameter	Value	Unit
Electrical power	100	kW
Thermal power	165	kW
Electrical efficiency	0.3	-
Overall cogeneration efficiency	0.8	-
Pressure ratio	4.5	-
Rotational speed	70000	rpm
Turbine outlet temperature	645	°C

2.1.1 T100 innovative layouts

The T100 is a flexible machine already extensively studied in different configurations due to its technical simplicity, ease of installation, high reliability and low maintenance requirements. It is suitable for operating with different fuels, in innovative cycles and integrated hybrid systems.

The T100 is fuel-flexibile provided that the combustor is redesigned based on the specific fuel combustion properties. The T100 is already commercially available in three different configurations: natural gas fired (AE-T100NG), biogas fired (AE-T100B) and externally fired (AE-T100E) [99]. The externally fired configuration can provide increased modularity and is generally used to exploit different non-standard solid and liquid fuels, like coal and biomass, thanks to the external boiler connected to a high-temperature heat exchanger used to transfer the thermal energy to the air after the compression. The heat source of externally fired mGTs can also be provided by renewable energy sources, avoiding the use of an external boiler (which is anyway made by the user and is not bought commercially). The use of other more innovative fuels, such as hydrogen and hydrogen-based blends to power the T100 combustor is currently under research. The traditional T100 combustor, similarly to other gas turbines, can operate with a maximum of 10 % of H_2 in volume as tested by Gaeta et al. [100] with minor modifications on the mGT, but the operation with higher percentages of hydrogen requires a combustor redesign due to the different combustion properties of H_2. Despite the combustion challenges, the first T100 in fuel flexible mode with different NG - H_2 blends was operated in 2022 in Stavanger as a result of a collaboration from the University of Stavanger (UiS) and the German Aerospace Center (DLR) which developed a jet-stabilsed burner for this specific application. In this test campaign, the H_2 content was varied from 50% to 100% at different part load conditions in the 35 kW – 100 kW range [101]. Regarding the use of ammonia as innovative fuel, the University of Genova is currently planning to test an existing T100, installed within a smart grid, properly modified for ammonia combustion, as part of the FLEXnCONFU European project [82].

Innovative cycles have also been extensively studied considering the T100 with the aim of increasing its electrical efficiency. Water or steam injection is considered an effective way to both increase efficiency and power output. Another beneficial effect is the reduction of the combustion temperature peaks which lowers NO_x production [102]. The T100 operation was tested in different

layouts considering liquid water or steam injection into various locations of the mGT. Renzi et al. tested the effect of air inlet fogging, a type of evaporative cooling that reduces the compressor inlet temperature by spraying small water droplets at the compressor inlet. The experimental activities showed an increase of +1.03 kW of power and +0.41 % efficiency for each degree Celsius of inlet temperature reduction as a result of the reduced compressor work [103]. The injection of water directly in the combustion chamber is another possibility for increasing the turbine power output. However, the best location for injecting liquid water is between the compressor and recuperator as proved by De Paepe et al. [104,105]. The mGT waste heat can be used to pre-heat the liquid water before the injection. During the injection the water evaporates lowering the air temperature. The combined effect of the reduced temperature and the increased heat capacity of the fluid increases the heat-recovery. Instead, the injection directly in the combustor would require additional fuel for the evaporation. Steam injection was also tested in different locations of the T100 all demonstrating improved performance and operating stability: De Paepe et al. performed different experimental activities injecting steam after the compressor [106], Renzi et al. numerically investigated the performance of steam injection into the combustor [107], while Ferrari et al. experimentally performed steam injection upstream of the combustion chamber [108]. Finally, a third option for water injection involves the use of a saturation tower with a water recovery loop. This configuration, named micro-humid air turbine (mHAT), is more efficient than steam injection due to the lower exergy destruction into the saturator, where an excess of water is injected into the compressed air. The air leaves the saturator with 100% of relative humidity and the remaining non-evaporated water is recirculated and heated again using an economiser. This configuration with the T100 has been extensively tested by Paepe et al. [109] .

Different hybrid systems have been integrated with the T100. Hybrid systems consist of the use of different components that have improved performance when working in an integrated system compared to using either technology alone. An example of an integrated system is the use of mGT coupled with high

temperature fuel cells, such as Molten Carbonate Fuel Cells (MCFC) or Solid Oxide Fuel Cells (SOFC). These systems can achieve very high conversion efficiencies (potentially over 60%), despite some issues such as high costs and difficult transient operation. For example, Pascenti et al. [110] developed a test rig of a high temperature fuel cell – micro gas turbine emulator based on the T100 micro gas turbine, in order to experimentally to study the effects of this integration with a focus on critical conditions like start-up and shut down of the machine.

The T100 has also been integrated with renewable energy sources. An example is the work from Barberis et al. [111] where the mGT was integrated with Concentrated solar panels (CSP) and a ceramic TES to stabilize the combustor inlet temperature subject to the renewable source availability and improve the system flexibility. Comodi et al. [112] considered the integration of a photovoltaic (PV) plant with the T100 considering smart management strategies to solve the issues related the renewables unpredictability.

The performance of the T100 has been investigated considering carbon capture storage systems. Giorgetti et al. [113] assessed the performance of the mGT performing Exhaust Gas Recirculation (EGR) to increase the concentration CO_2 at the exhaust and therefore improve the performance of the CC plant.

2.2 The TRANSEO tool

The T100 was modelled with the TRANSEO software, a library of modular components for modelling energy systems dynamics. It was developed in the MATLAB/Simulink platform by the Thermochemical Power Group (TPG) of the University of Genoa. The MATLAB/Simulink tool was used instead of open access software because the component models to be used in this thesis (the TRANSEO tool) work in MATLAB/Simulink. In details, Simulink is mainly used to exploit the visual interface to easily connect the library of different components, for the post-processing and for the managing the time-varying simulations. However, the core functions are developed in Fortran and C

languages. In detail, the chemical and thermodynamic fluid properties are computed from a Fortran code database based on the Perry's Chemical Engineers' Handbook [114], common for all the tools developed by the TPG research group, while each component dynamic behaviour is developed in separate C functions. The Fortran and C functions result in a higher time-performance than a direct software written in the MATLAB language. These subroutines are connected to Simulink through C MEX functions.

The TRANSEO tool was designed for modelling the dynamic behaviour of energy systems. The dynamic behaviour of plant layouts can be determined by mass and energy balances with a good approximation, while the impact of the momentum balance, such as the phenomena of pressure wave propagation, can typically be neglected due to faster timescales to allow for faster computational time. Many previous studies have validated all the available single components and the interconnecting approach [115–117]. Each component receives a stream of information including mass flow, pressure, temperature, and chemical composition. The interconnecting logic can be set in the following different ways:

- "Mass flow active": the component receives the information about the upstream and downstream pressure and calculates internally the mass flow rate, depending on the component physical characteristics.
- "Mass flow inactive": the component receives the mass flow rate information from either the upstream or downstream connected component. At the same time, the pressure is calculated internally, whose value is sent in the opposite direction of the mass flow.

Along with validating the single components, TRANSEO has shown accurate predicting behaviour for modelling micro gas turbines in various configurations [115,116,118–121]. In particular, the T100 micro gas turbine has been investigated in different layouts such as standard recuperated cycles [122], externally fired configurations [123], solar-hybrid systems [116,117] and humidified cycles [120]. The following paragraph describes the assumption and model description of the T100 and validation of the overall plant.

2.3 The T100 TRANSEO dynamic model

Most TRANSEO components are modelled according to a "lumped-volume" representation to calculate the impact of the volumetric and thermal capacitance of each component, the mass flow oscillations caused by pressure variations and the heat transfer exchanged between other components and the ambient. For a system dynamic analysis, the "lumped-volume" approach ensures a good balance between accuracy and calculation speed, while a more detailed, but still simplified approach is the "quasi 2D approach", which involves discretising the components to model the heat transfer effects between adjacent cells into the flow direction and between the metal parts in the parallel direction. This level of detail is required in components such as heat exchangers, where the modelling of the heat transfer phenomena requires higher accuracy.

Figure 2-3 shows the T100 layout in TRANSEO, where each component is described in the following subparagraphs.

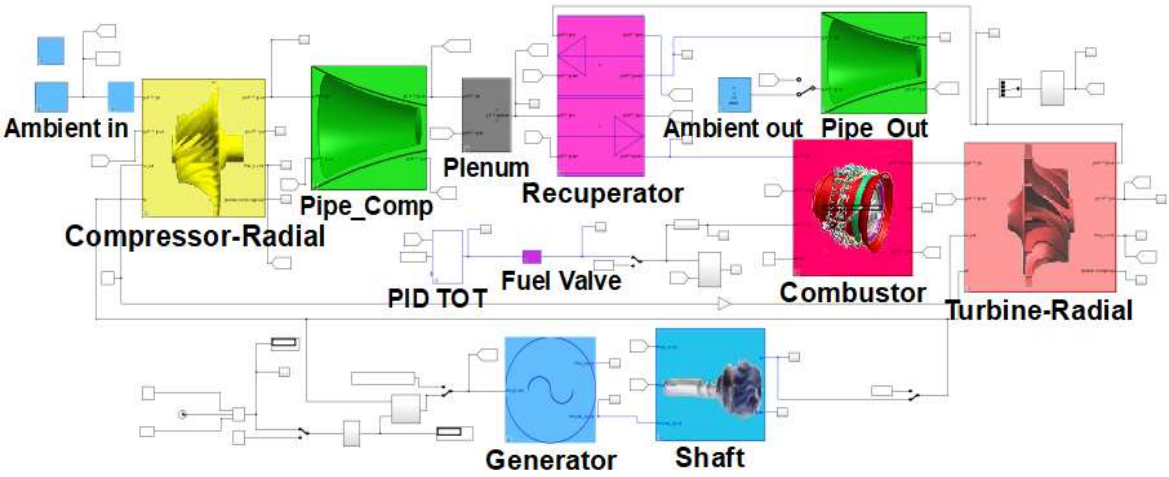

Figure 2-3: Transient model of the T100 in TRANSEO.

2.3.1 Lumped-volume components

The components modelled according to the "lumped-volume" approach are the pipes, compressor, turbine, combustor and interconnecting plenum. The general lumped-volume structure is displayed in Figure 2-4. According to this modelling approach [122], the component is divided in two parts: an actuator and an

equivalent duct. The component calculations are performed by superimposing the effects of these two parts, first 1) the steady-state off-design performance is calculated (actuator part) and then 2) the dynamic behaviour is determined by modelling the component as a duct of equivalent cross-sectional area (A_{eq}) and length (L_{eq}).

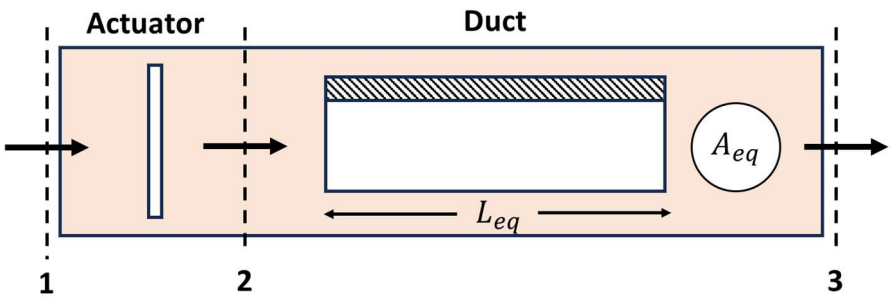

Figure 2-4. Configuration of a TRANSEO component based on the lumped volume approach (1: the input of the component is connected to the input of the actuator disk; 2: the output of the actuator disk is linked to the input of the duct; 3: the output of the duct corresponds to the output of the component).

The off-design behaviour of each component is dependent on its specific internal characteristics. For example, the off design of a pipe can be represented by a pressure loss; for a compressor or turbine this can be represented by their characteristic map.

The transient behaviour is determined by using the momentum and energy equations, (Eq. (**2-1**) to (**2-3**)):

$$\frac{d\dot{m}}{dt} = \frac{A_{eq}}{L_{eq}} (C - \Delta p) \tag{2-1}$$

$$\frac{d(c_v \rho\, V\, T)}{dt} = \dot{m}\, \Delta \mathrm{h} - \dot{q}_{solid} \tag{2-2}$$

$$\frac{d(c_{p,solid}\, M_{solid}\, T_{solid})}{dt} = \dot{q}_{solid} - \dot{q}_{loss} \tag{2-3}$$

Where the momentum contribution from the actuator is represented by C, the pressure and enthalpy difference of the fluid between the duct inlet and outlet are represented by Δp and Δh respectively, $\dot{q}_{solid}$ represents the heat flux

through the solid duct part, including the thermal power heating the metal and the heat lost to the environment.

In summary, each component solves the characteristic steady-state equations and equations (2-1) to (2-3). The equivalent duct is not divided into discretised segments (its properties are homogeneous along the duct), meaning that its equations are only integrated over time and not along its length.

2.3.1.1 Pipes

Two pipes are present in the T100 model, one after the compressor and another before the exhaust. Only two pipes are considered, concentrated in two different points as a compromise between accuracy and computational time. It is assumed that the pressure drops and temperature variations due to the inlet, air filter and the combustor collector are distributed in the different components of the mGT to reduce the simulation speed.

The piping system steady-state behaviour is modelled according to a pressure drop (Eq. (2-4)):

$$\Delta P_{pipe} = \rho \frac{v^2}{2} f \frac{L_{eq}}{D_{eq}} \tag{2-4}$$

Where ρ and v are the density and fluid velocity, f is the friction coefficient and D_{eq} is the duct equivalent diameter.

The mass storage effect cannot be simulated in pipes components. To simulate the mass storage, a "plenum" component (described in paragraph 2.3.3.1) is located after the compressor pipe. The delays due to the mass accumulation are concentrated in a single plenum to reduce the computational time.

2.3.1.2 Compressor and turbine

Both the radial compressor and turbine are represented by non-dimensional characteristic maps, where the non-dimensional mass flow and efficiency are determined from the corrected rotational speed and pressure ratio. This allows

calculating the total outlet temperatures through isentropic relations (Eq. (2-5) and Eq. (2-7)) and, therefore, the power consumed or produced, respectively (Eq. (2-6) and (2-8)). The main compressor equations to calculate the outlet total temperature $T_{comp-out}$ and absorbed power P_{comp} are reported below:

$$T_{comp-out} = T_{comp-in}\left(1 + \frac{\beta_{comp}^{\frac{\gamma-1}{\gamma}} - 1}{\eta_{comp}}\right) \tag{2-5}$$

$$P_{comp} = \dot{m}_{comp} C_{p-mean}\left(T_{comp-out} - T_{comp-in}\right)/\eta_m \tag{2-6}$$

Where $T_{comp-in}$ is the compressor inlet total temperature, β_{comp} is the compressor pressure ratio, η_{comp} the isentropic efficiency, γ is the ratio of the specific heats at constant pressure and volume, $\dot{m}_{comp}$ is the compressor mass flow, C_{p-mean} the compressor average specific heat and η_m is the mechanical transmission efficiency, which is 0.99 in this case.

Similarly, the turbine equations to calculate the outlet total temperature $T_{turb-out}$ and the generated power P_{turb} are reported below:

$$T_{turb-out} = T_{turb-in}\left[1 - \eta_{turb}\left(1 - \beta_{turb}^{-\frac{\gamma-1}{\gamma}}\right)\right] \tag{2-7}$$

$$P_{turb} = \dot{m}_{turb} C_{p-mean}(T_{turb-in} - T_{turb-out}) \tag{2-8}$$

Where $T_{turb-in}$ is the turbine inlet total temperature, β_{turb} is the turbine expansion ratio, η_{turb} the isentropic efficiency, γ is the ratio of the specific heats at constant pressure and volume, $\dot{m}_{turb}$ is the turbine mass flow and C_{p-mean} the turbine average specific heat.

The heat transfer calculation considers the compressor and turbine heat exchange, along with the heat lost to the environment. A unique heat transfer coefficient has been considered to take into account of both effects.

2.3.1.3 Combustor

For the combustor, the off-design behaviour is described by solving the unsteady energy equation (Eq. (2-9)) considering a combustion efficiency η_{comb} of 0.996 and methane LHV = 43.44 MJ/kg:

$$\frac{d(c_v \rho_{mean} V\, T_{out})}{dt} = (\dot{m}_{air} h_{air})_{in} + \dot{m}_{fuel} h_{fuel} + \dot{m}_{fuel} \eta_{comb} LHV - \left(\dot{m}_{gas} h_{gas}\right)_{out} \tag{2-9}$$

$$\dot{m}_{gas} = \dot{m}_a + \dot{m}_f \tag{2-10}$$

Where, c_v is the specific heat at constant volume, ρ_{mean} is the mean density, V is the volume, T_{out} the combustor outlet total temperature, $\dot{m}$ is the fluid mass flow rate and h the enthalpy; the subscript "a" is referred to the inlet air properties, "f" to the fuel properties and "g" to the exhaust gas, whose mass flow is calculated according to Eq. (2-10).

The pressure losses in the combustor are calculated considering the contribution of both viscous losses and pressure drops due to the fluid acceleration.

2.3.2 Quasi-2D components

In this T100 layout, the recuperator is the only component modelled using a quasi-2D approach [122]. This approach involves a discretisation of the component to model the unsteady form of the energy equation. Instead, the continuity and momentum equations are calculated according to the simplified "lumped-volume" approach in one single cell. This is a reasonable assumption considering the low flow velocity involved in the heat exchanger (around 10 m/s).

2.3.2.1 Recuperator

The recuperator is a counter-flow heat exchanger used to heat up compressed air with a pressure around 4.5 bar using the hot stream of exhaust gases leaving the turbine at ambient pressure. The discretisation of the recuperator is shown in Figure 2-5, where the component is vertically divided into four main parts, identified by the subscript "j", representing the hot and cold flow passages, the

internal matrix, and the external vessel. Each main part is then longitudinally discretised into N elements to improve the calculation accuracy of the dynamic energy and heat transfer equations, where "i" refers to the i-th element in the discretisation. The following energy equation Eq. (2-11) is solved according to a partial difference numerical scheme:

$$\rho_{j,i}\, c_{v_j} A_j \frac{\partial T_{j,i}}{\partial t} = -\, c_{p_j} \dot{m}_j \frac{\partial T_{j,i}}{\partial x} + \dot{q}_{j,i} \qquad \text{for j=0 to 3 and i=0 to N} \qquad (2\text{-}11)$$

Where the heat source $\dot{q}_{j,i}$ includes factors such as convection between solid walls and fluids, heat losses to the environment and conduction along the longitudinal axis of the heat exchanger. The components of $\dot{q}_{j,i}$ are calculated using standard conductive and convective heat transfer equations based on the parameters and physical properties specified by the specific heat exchanger. The surfaces A_j represent the total cross-sectional areas of each cell, while the surfaces S_j represent the portion of the exchanging surface relative to each cell.

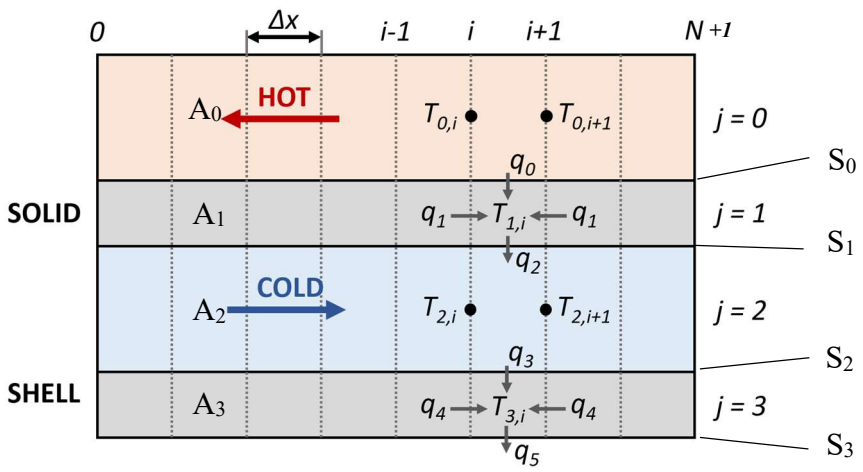

Figure 2-5. TRANSEO heat exchanger discretisation (j=0 - hot fluid, j=1 - solid matrix, j=2 - cold flow, j=3 - outer shell).

2.3.3 Other components

The other components that do not belong to the "lumped-volume" and "quasi 2D" categories are the plenum, T100 shaft and control system.

2.3.3.1 Plenum

The plenum is a rigid volume that can be used to mix different mass flow and to reproduce the fluid dynamic inertia that leads to mass storage and pressurisation effect, which are not considered in the lumped volume. The plenum volume V is set equal to the total piping system volume. In the general form, this component can receive different mass flow streams and it integrates the continuity and energy equations to determine its internal pressure and temperature based on the incoming mass flow information from upstream and downstream, while considering the heat loss to the environment. The unsteady continuity and energy equations (Eq. (2-12) and (2-13)) are reported below:

$$\frac{d(\rho V)}{\mathrm{dt}} = \dot{\mathrm{m}}_{in} - \dot{\mathrm{m}}_{out} \tag{2-12}$$

$$\frac{d(\rho V T)}{\mathrm{dt}} = \frac{c_{\mathrm{p-out}}}{c_{\mathrm{v}}}(\dot{\mathrm{m}}_{in} T_{in} - \dot{\mathrm{m}}_{out} T_{out}) \tag{2-13}$$

The plenum outlet temperature T_{out} for the following time step is calculated from Eq. (2-13) while the continuity equation of Eq. (2-12) is used to update the plenum mass flow.

2.3.3.2 Shaft

The T100 shaft is the link between the compressor, turbine, and generator and transfers the mechanical power produced by the turbine to the generator, where it is transformed into electrical power. The rotational speed of the shaft is determined by Eq. (**2-14**), considering the effect of the turbocharger rotational inertia J and the mechanical power losses in bearings:

$$P_{turb} - P_{compr} - P_{loss} = J\frac{d\left({\omega^2}/{2}\right)}{dt} \tag{2-14}$$

where P is the power, ω is the rotational speed.

2.3.3.3 Control system

The T100 model control system integrates two control loops [120] to deliver the required power output and maintain the TOT value equal to the setpoint of 645 °C. The first control loop is for controlling the electrical power output and it uses a feedforward and a slow PI technique. In detail, the set point value of the rotational speed is obtained by combining the effects of the feedforward approach based on a predefined table and of the PI controller, which receives the TOT as input. The second loop employs a fast PID controller to manage the fuel valve opening and keep the TOT equal to 645 °C.

2.4 First model: VUB micro gas turbine

The T100 model used in this analysis was validated in a previous study, where the experimental activities performed to validate the model were conducted on a Turbec T100 of the Vrije Universiteit Brussel (VUB) facility [120]. This specific T100 was modified to be also used in a humidified cycle, but in this work, only the standard dry operation is considered. To consider this, longer pipes were included, leading to higher pressure losses concentrated in the compressor pipe component. The overall comparison between experimental data and model results is presented by Carrero et al. [120] and it is summarised in this paragraph. The steady-state tests to validate the model were obtained in the 25 °C - 27 °C temperature range, with different measurements up to the generated maximum power output P_{gen}= 85.8 kW. Removing the percentage of power used to run the auxiliaries, which includes the gas compressor, this corresponds to a net power output P_{net}= 82.8 kW. The T100 was not able to reach a higher power output since the ambient temperature was higher than the nominal (15 °C) and due to the additional piping system required for the mGT modification. In detail, both these effects make the rotational speed rise to increase the mass flow rate, but for structural limitations of the machine, the maximum rotational speed is set to 70000 rpm which limits the maximum net power output. Moreover, these

effects also limit the electrical efficiency to η_{el}=24.95% at the maximum power output. The results obtained in steady-state conditions matched the experimental data well, with errors below 1.5%, which is lower than the sensors accuracy range. The dynamic behaviour was also validated performing a power step from 78.3kW to 59.7 kW resulting in a good matching.

2.4.1 Steady-state characterisation

This paragraph reports the main steady-states parameters (Figure 2-6 and Figure 2-7) as a function of different net power outputs considering different ambient temperatures T_o (5°C, 15°C, 25°C and 35°C). The steady-state points are obtained numerically with the same transient code waiting for stable conditions for each operating point. These results are obtained to identify the baseline that will be used to compare the normal mGT effect with the integration of the energy storage systems.

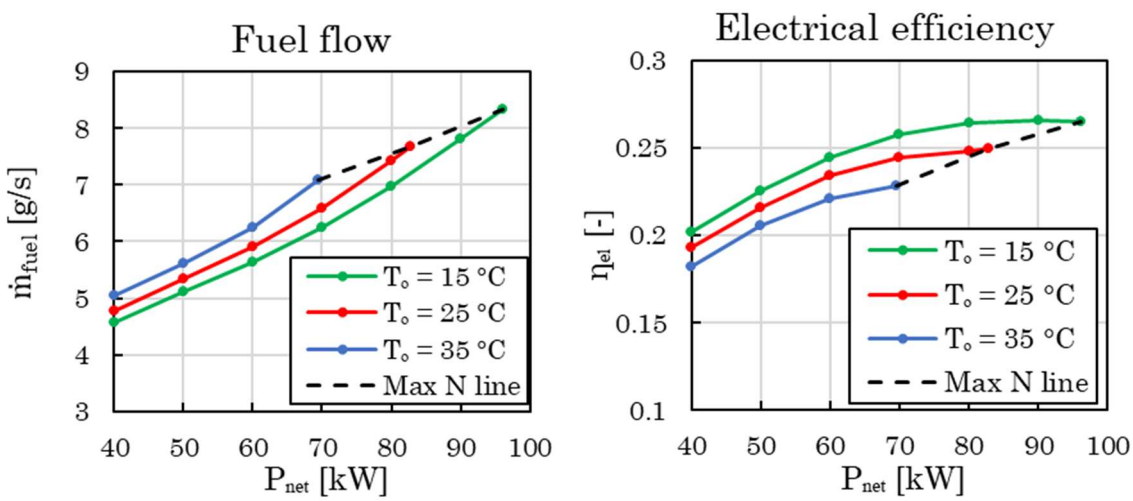

Figure 2-6. Fuel flow and electrical efficiency of the T100.

As expected from the normal behviour of micro gas turbines, the electrical efficiency and maximum power output increase when reducing the ambient temperature. The maximum line represents the points where the maximum rotational speed is reached (Figure 2-7 right). For example, while at $T_o = 25°C$, P_{net}= 82.8 kW and η_{el}=24.95%, at $T_o = 15°C$, P_{net}= 96.1 kW and η_{el}=26.5 %. In general, a reduction of T_o of 10°C leads to an increase of +13.5 kW, and around

+1.5-2% in absolute value of the electrical efficiency at the maximum power output.

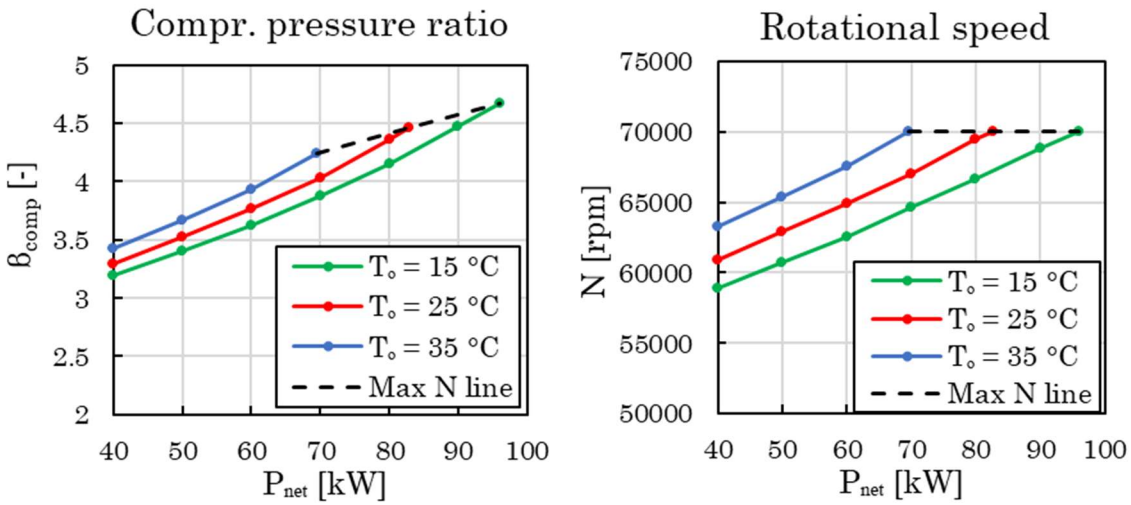

Figure 2-7. Compressor pressure ratio and rotational speed of the T100.

Along with the compressor performance parameters calculation, the evaluation of the compressor safe operating conditions is paramount. Specific working conditions could lead to the phenomena of compressor surge, a form of aerodynamic instability consisting of oscillations in the axial direction of the air flow velocity. Surge typically occurs at low mass flow rates when the blades lose their ability to effectively transfer the mechanical energy to the fluid. In some conditions, the generated oscillations can be violent and result in a negative flow direction. Operating during compressor surge is not acceptable as it leads to unstable conditions and potentially to catastrophic damages of the compressor and entire machine [124]. The surge margin is commonly used in literature as an indicator to measure the distance of an operating point from a surge event. Although various definitions exist, in this work the surge margin is indicated with k_p and it is calculated using Eq. (2-15) [123]:

$$k_p = \frac{\dot{m}/\beta}{\dot{m}_{s.l.}/\beta_{s.l.}} \tag{2-15}$$

The term k_p is defined as the ratio between the mass flow rate $\dot{m}$ and the pressure ratio β of the compressor operating condition, divided by the mass flow and pressure ratio evaluated where the iso-speed line of the operating point intersects the surge line (Figure 2-8).

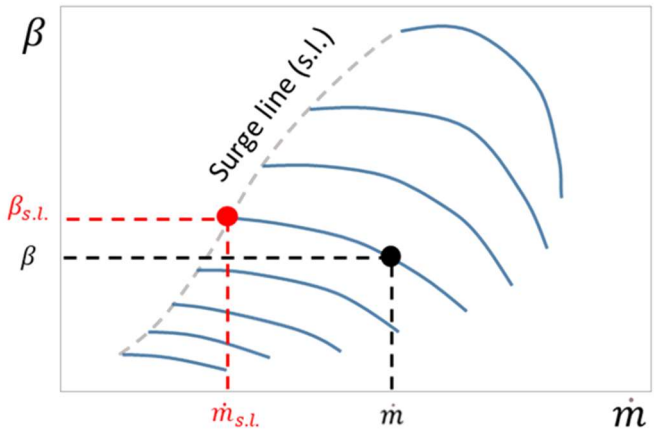

Figure 2-8. Schematic representation of the compressor operating point (black) and surge point on the same iso-speed line (red) on a generic compressor map.

According to this definition, the theoretical value for the surge margin should be at least 1, but it is advisable to maintain a higher safety limit. Following previous studies [123], a surge margin of 1.1 will be considered as the lower limit for this analysis. Although the compressor is theoretically stable for $k_p > 1$, surge conditions could be easily triggered even by minor fluctuations of the working conditions in the 1 – 1.1 range.

Figure 2-9 shows the steady-state surge margin for this specific T100. In general, higher power outputs result in safer operating conditions with higher k_p values. Despite the positive effect of the ambient temperature reduction, it is worth noting that the k_p is subject to a reduction. For example, at $T_o = 25\ °C$, the $k_p =$ 1.1 when P_{net}= 36 kW, while at at $T_o = 15\ °C$, the $k_p = 1.1$ when P_{net}= 28 kW. Therefore, low ambient temperatures limit the mGT operation at low power outputs.

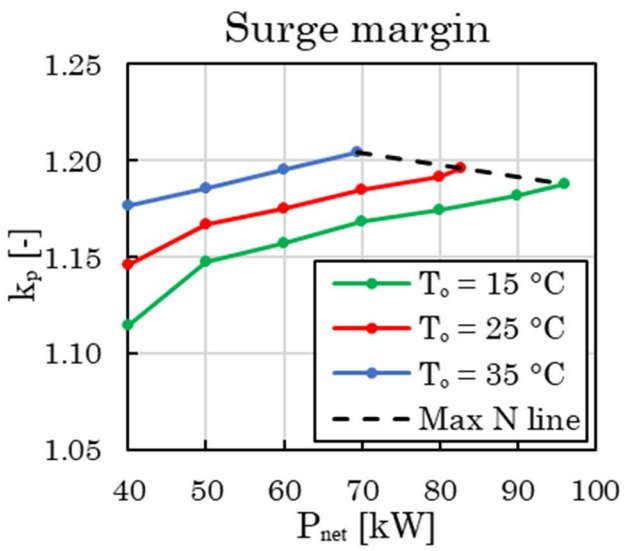

Figure 2-9. Steady-state surge margin.

2.4.2 Dynamic behaviour

This paragraph reports the transient behaviour of the main parameters: surge margin (Figure 2-10) and turbine outlet temperature (Figure 2-11), considering different power decrease steps of 10 kW starting from stable conditions of 80 kW, 60 kW and 40 kW at $T_o = 25°C$. While the surge margin should be monitored to avoid incurring into compressor instability, the TOT is a good indicator of the temperature oscillations and therefore the thermal peaks affecting the recuperator. This behaviour will also be compared with the integration of the other energy storage systems.

The reason for the surge margin reduction during a power decrease step is the following: when the power output is decreased, the control system reduces the rotational speed; this reduces the compressor mass flow with a fast response, while the pressure ratio variation is slower, and it remains high for a longer time before reducing as well. The k_p reduction during transients is acceptable at higher loads, but at lower load, for example in the case from 50 kW to 40 kW, lower rates of power decrease should be adopted to avoid a $k_p <$ 1.1 during the operation.

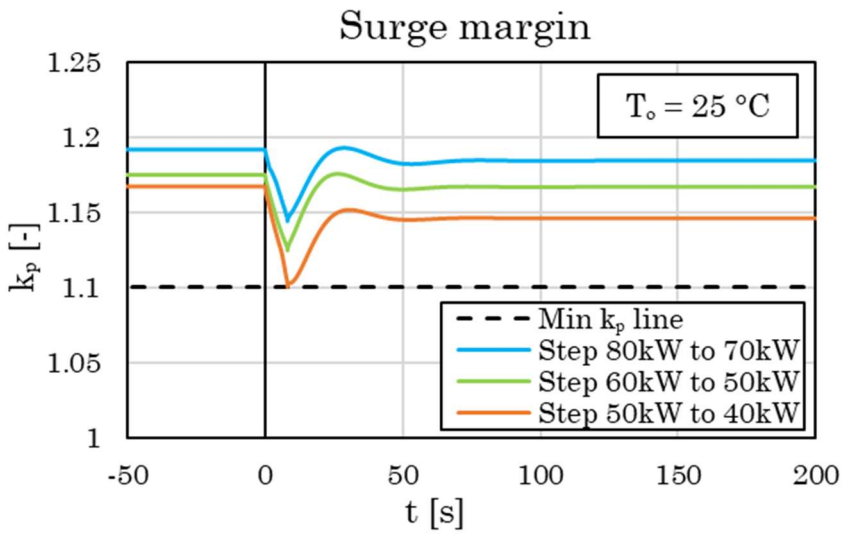

Figure 2-10. Surge Margin transient behaviour during different power steps.

At the moment of the power decrease step, the TOT initially increases because the control system reduces the air mass flow with a fast response while the fuel flow is reduced with a slower response. In general, peaks of around +10 °C are acceptable for few seconds of operation.

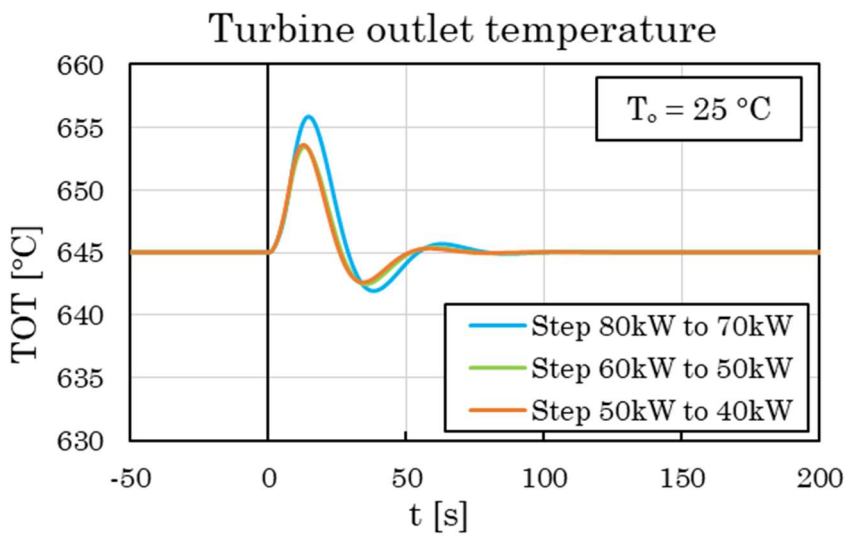

Figure 2-11. TOT transient behaviour during different power steps.

2.5 Second model: UNIGE micro gas turbine

2.5.1 Experimental activities

Experimental activities were conducted at the Innovative Energy System Laboratory in the Savona Campus of the University of Genoa to validate a transient model of a Turbec T100 micro gas turbine during regular operation and when injecting compressed air upstream of the recuperator. The injection of air is used to simulate the interaction with a CAES system in the moment where air is discharged from a tank into the mGT.

The experimental facility has been previously described in different publications [110,125,126]. The main purpose of this facility was to model a T100 connected with a fuel cell emulator. For this reason, the micro gas turbine (Figure 2-12) was connected with a high temperature volume with a new set of pipes for the physical emulation (Figure 2-13). However, in this specific case, it is of interest to test only the T100 and therefore the valves connecting the volume (VC, VR and VO) were closed. Although the T100 is equipped with standard probes for control and diagnostic, additional sensors were added to measure a higher number of properties. Table 2-2 summarises the additional parameters just used for the validation along with the probe type and accuracy. The mass flow rate is calculated from the differential pressure signals of the pitot tubes and the temperature values obtained from the thermocouples positioned nearby.

Figure 2-12: T100 of the Savona Campus IES lab.

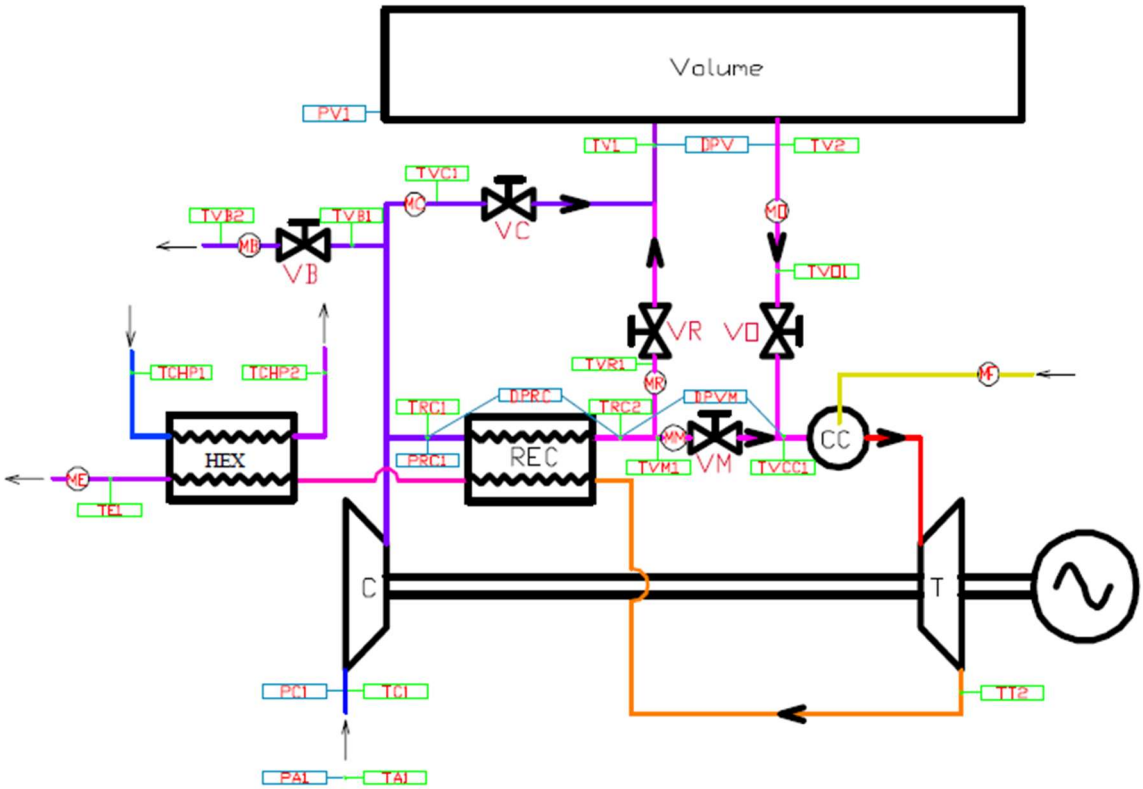

Figure 2-13: Plant layout and instrumentation.

The compressed air was injected upstream of the recuperator as in the TRANSEO model. A volume was filled with compressed air obtained with a compressor able to elaborate up to 200 g/s reaching maximum 8 bars. The volume was connected to the T100 injection point through a piping system. Due to the heat exchange with the environment, the compressed air at the point of injection can be considered to be around the ambient temperature (25 °C). The air was injected at constant power, first with a step from 0 g/s to 15 g/s and then with a step from 15 g/s to 30 g/s (maximum delivery mass flow). The mass flow was regulated through a Bronkhorst mass flow controller which has a response time of around 2 s. The air was injected imposing a constant electrical power (40 kW and 60 kW) for the mGT and, after that, imposing the maximum load. During the air injection no combustion flame out was detected.

Table 2-2: List of additional measured parameters used for the validation.

Name	Description	Probe type	Accuracy
TRC1	Recuperator inlet temperature cold side	Thermocouple	±2.5°C
TRC2	Recuperator outlet temperature cold side	Thermocouple	±2.5°C
TVCC1	Combustor inlet temperature	Thermocouple	±2.5°C
TOT	Turbine outlet temperature	Thermocouple	±2.5°C
TRE	Recuperator outlet temperature hot side	Thermocouple	±2.5°C
PRC1	Recuperator inlet pressure cold side	Absolute	±1%
PRC	Recuperator outlet pressure cold side	Differential	±1%
PVM	Combustor inlet pressure	Differential	±1%
MM	Main line mass flow	Pitot tube	±3%

The summary of the operations during the experiments is listed below and can be visually identified in Figure 2-14:

1) Steady-state condition reached at 40 kW and 0 g/s of injected air
2) Step from 0 g/s to 15 g/s of injected air at 40 kW
3) Step from 15 g/s to 30 g/s of injected air at 40 kW
4) Step from 30 g/s to 15 g/s of injected air at 40 kW
5) Step from 15 g/s to 0 g/s of injected air at 40 kW
6) Power step from 40 kW to 60 kW
7) Step from 0 g/s to 15 g/s of injected air at 60 kW
8) Step from 15 g/s to 30 g/s of injected air at 60 kW
9) Step from 30 g/s to 15 g/s of injected air at 60 kW
10) Step from 15 g/s to 0 g/s of injected air at 60 kW
11) Power step from 60 kW to the maximum allowed power output (around 72.3 kW)
12) Step from 0 g/s to 15 g/s of injected air at the maximum allowed power output (because of the air injection a higher power output is reached at about 75 kW)
13) Step from 15 g/s to 30 g/s of injected air at the maximum allowed power output (because of the air injection a higher power output is reached at about 78 kW)

The T100 maximum electrical power output was below the nominal value (100 kW) because the tests were carried out with an ambient temperature in the 25 °C–27 °C range which is higher than the nominal ambient temperature (15°C) and the additional pipes of the system produced higher pressure losses (it is a typical and well-known limitation of the used facility [125]).

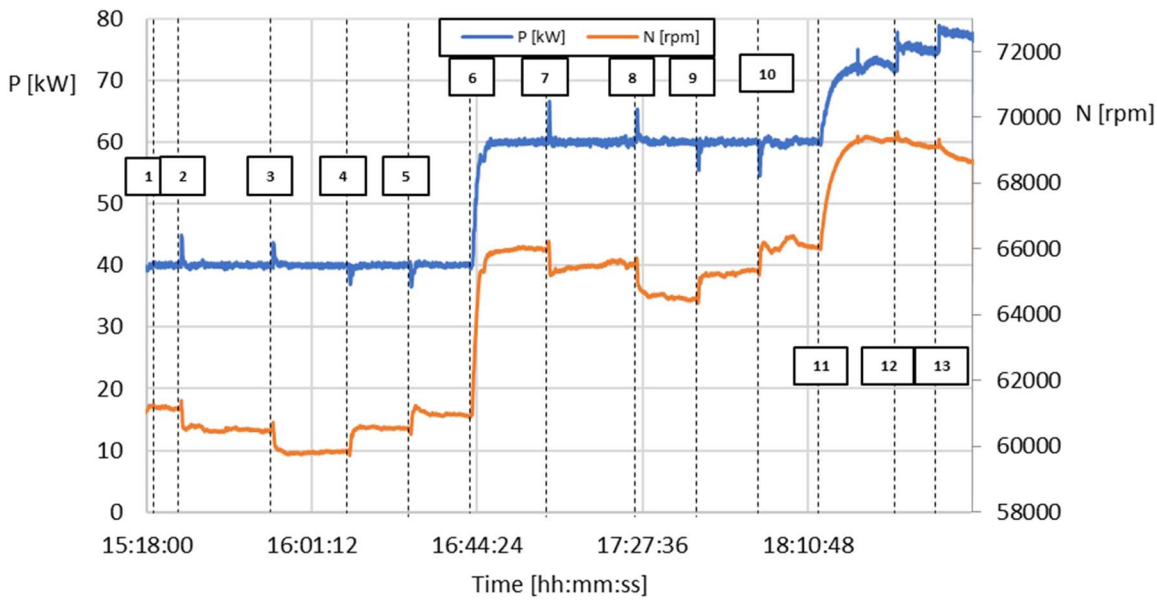

Figure 2-14. Net power output and rotational speed from tests.

Figure 2-15 provides a zoom on one of the operating points at 60 kW showing the transition from 0 g/s to 15 g/s of injected compressed air. The machine recovery is around 30 s after the injection for the power output and rotational speed.

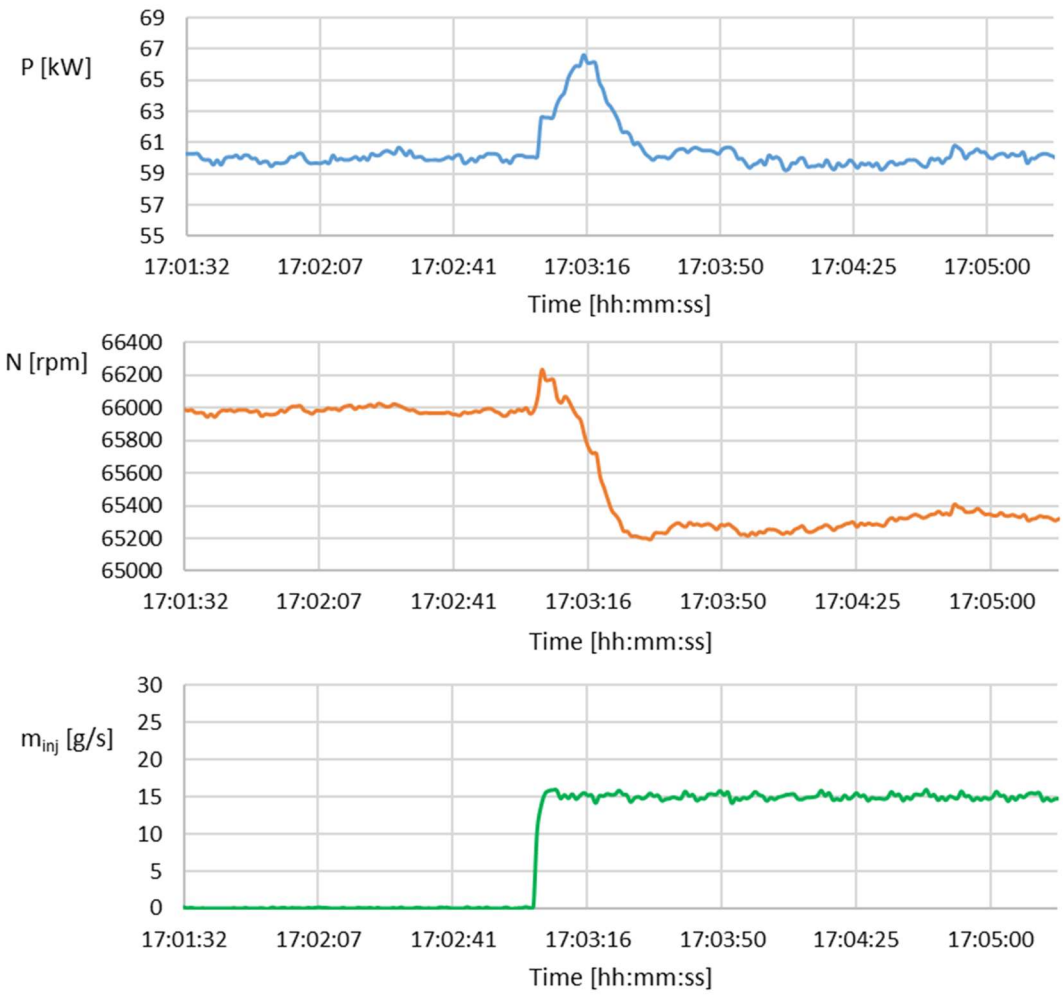

Figure 2-15. Zoom on the operating point (net power output, rotational speed, and injected air) at constant power of 60 kW while injecting 15 g/s.

2.5.2 Steady-state validation

The model was validated for both the steady-state and dynamic conditions. For simplicity, for the steady-state operations, the comparison between measured and calculated values is shown (Figure 2-16) only for of the cases without air injection. For completeness, Figure 2-17 summarizes the percentage errors for all the considered cases (no injection, injection of 15 g/s and injection of 30 g/s). While for the cases without air injection the comparison was performed at P = 40 kW, 60 kW and 72.3 kW, for the cases with air injection the comparison was performed only at P = 40 kW, 60 kW. This is because the developed TRANSEO model is yet not able to determine the maximum power output since at the

moment the power output of the mGT is an input value for the model that has to be specified. The addition of this capability within the model will be included in future activities. The comparisons against steady-state results of Figure 2-17 show a good matching with errors all below 1.5%, except from the TRE and TRC2 where the error is higher but still below 2.2%.

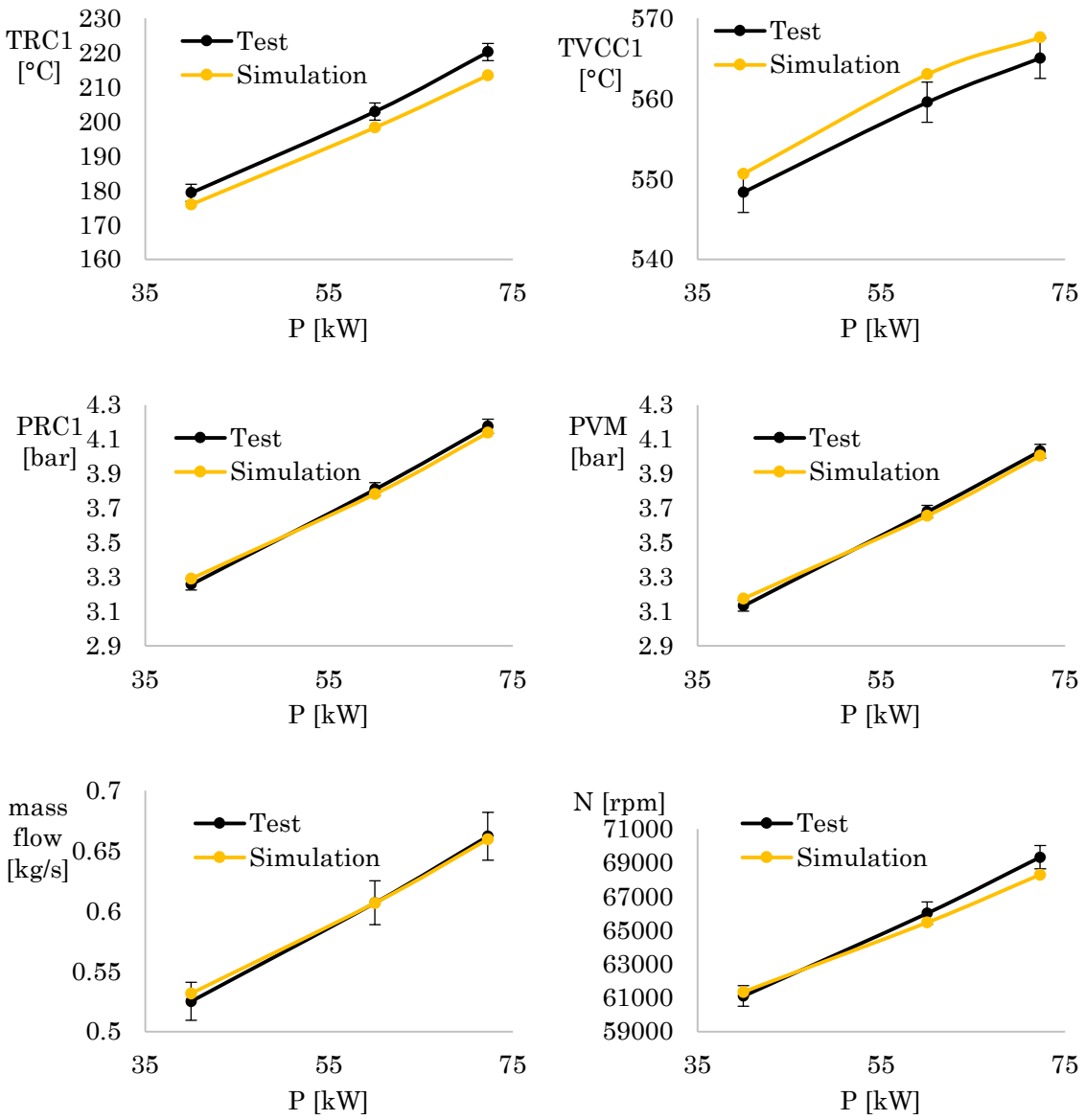

Figure 2-16. Comparison between the steady-state experimental and simulated results for the main cycle parameters.

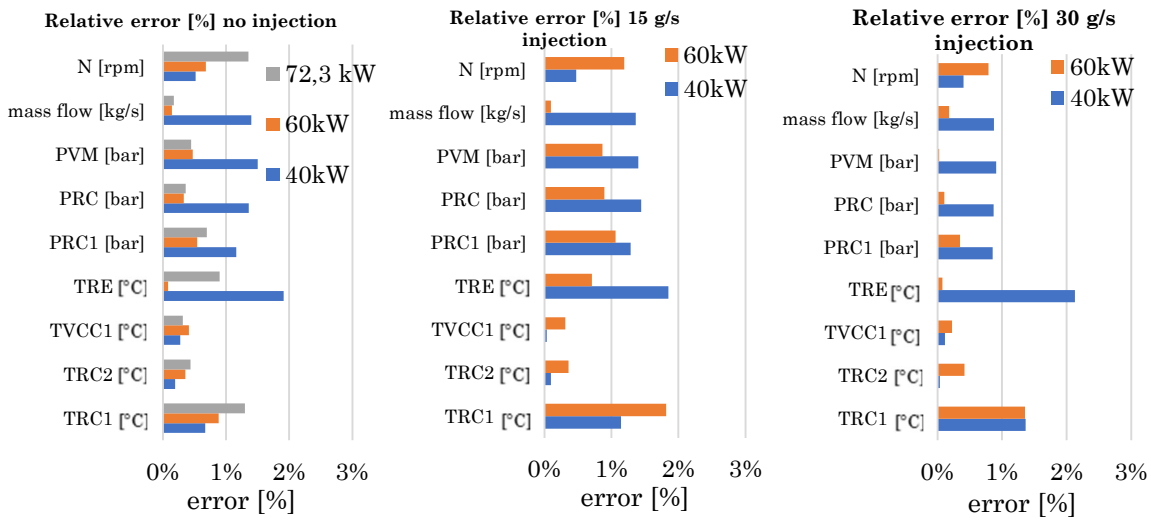

Figure 2-17: percentage errors of the results of the model relative to the experimental data for the main cycle parameters.

2.5.3 Dynamic validation

Following the steady-state validation of the T100 with injection of air, the transient behaviour was also validated. The dynamic behaviour of the model was also validated considering the case of a step change of injected air from 0 g/s to 15 g/s at constant P = 60 kW. Also in this case, some of the main performance parameters were compared against the measured experimental data providing a good agreement during the transient operation.

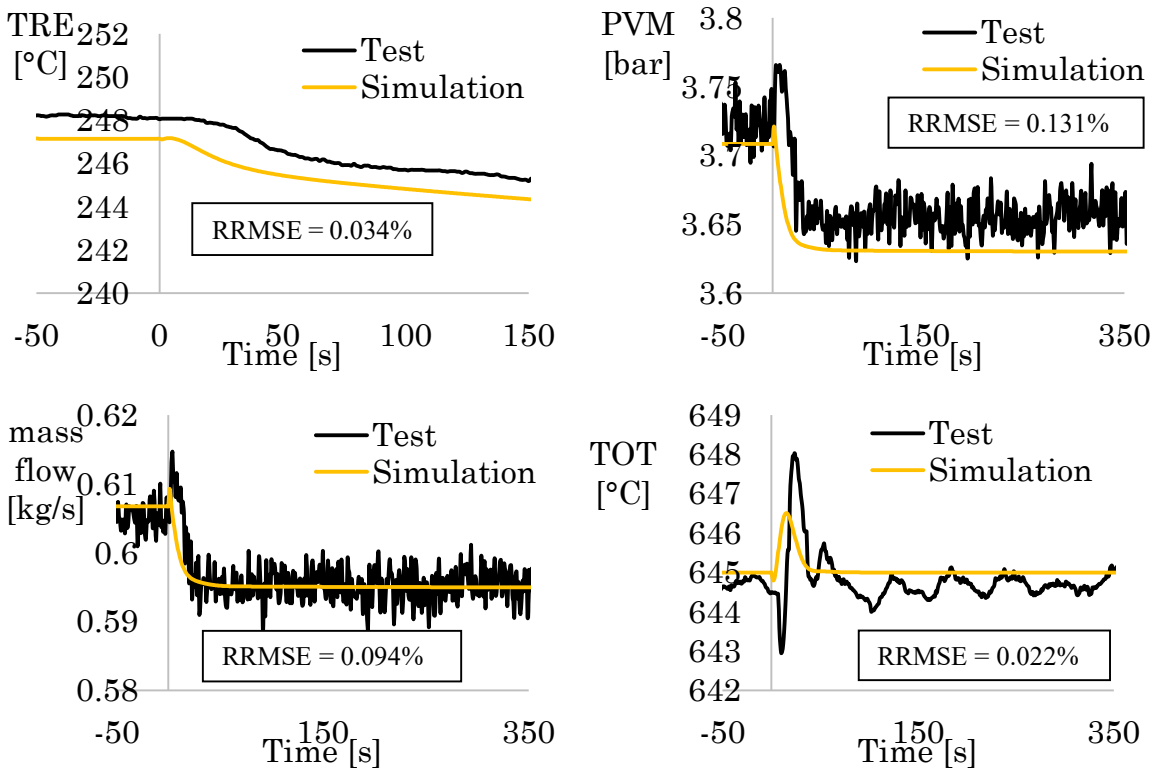

Figure 2-18: Comparison between the dynamic experimental and simulated results for the main cycle parameters at constant P = 60 kW with injection of 15 g/s.

Experimental activities were conducted on a T100 imposing a constant power of 40 kW, 60 kW and maximum load and injecting different amounts of compressed air (0 g/s, 15 g/s, 30 g/s) to simulate the effect of the discharge of a CAES system on the mGT. The TRANSEO tool was successfully validated against steady-state experimental data both in normal operation and with air injection. The obtained steady-state errors for the main cycle parameters were below 1.5 % except from the TRE and TRC2 where the error was higher but still below 2.2%. In addition, the model results for transient operation with air injection showed a good agreement with the experimental data, as also shown by the Relative Root-Mean Squared Error (RRMSE) reported in each graph of Figure 2-18. Despite some small steady-state discrepancies between the simulated and tested values, especially for PVM, these values are within acceptable limits as reported in the steady-state validation of Figure 2-17.

3 Steady-state and dynamic analysis of the T100 integrated with a small-size CAES system

This chapter regards the steady-state and dynamic analysis of a small-size second-generation Compressed Air Energy Storage system. It consists of a recuperated T100 micro gas turbine, an intercooled two-stage reciprocating compressor, and an artificial tank for air storage. A significant innovation regards the proposed integration with the Tesla turbine technology [39,40] as a topping expander to recover additional work before the injection. This work aims to fill the research gap in the dynamic analysis of small-size S-CAES systems by investigating the effects of air injection during the CAES discharging phase on transient operating issues (mainly thermal gradients and compressor stability issues) and analysing the risky operating conditions. Following a section with calculations to motivate the activity from economic point of view, the interaction of the T100 integrated with the CAES system is analysed through a validated dynamic model.

3.1 Plant layout

The plant layout considered in this work (a T100 mGT coupled with the external CAES system as shown in Figure 3-1) is not fully innovative because it was already considered in Arnulfi et al. [22]. The first innovative part from the layout point of view regards the application of a Tesla turbine to exploit the expansion for the air flow injected in the microturbine. In addition, this work considers the dynamic analysis and the identification of constraints related to the system dynamic behaviour (mainly related to the surge margin and the thermal stress related to the microturbine system).

The CAES side consists of a two-stage reciprocating compressor (85% isoentropic efficiency) with intercooling (89% effectiveness) and aftercooling (87% effectiveness) using water as a cooling medium (charging side), an artificial vessel (storage side), a small-size Tesla turbine and an additional recuperator

for the air pre-heating (discharging side). Surplus electricity from renewable sources or low-price electricity can be used to compress the air by means of the reciprocating compressor. Then, the air is stored until the discharge phase, where the air heats up and expands before being injected upstream of the T100 recuperator.

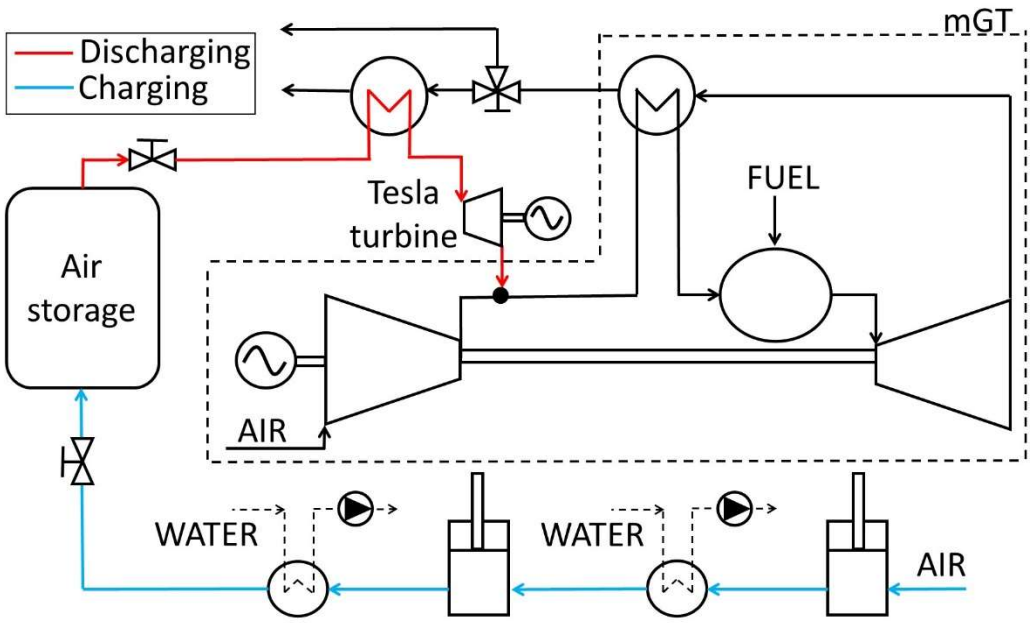

Figure 3-1. Plant Layout.

The main CAES system design point specifications are reported in Table 3-1. A two-stage compressor represents a trade-off between compressor efficiency and cost. Therefore, a relatively low tank maximum pressure of 50 bar has been chosen, in agreement with a previous off-design study from Arnulfi et al. on a similar layout [64]. On the discharging side, two options, both considered, are possible: 1) a direct injection into the mGT or 2) an expansion prior to the injection. In the former case, the obtained fuel saving is only due to the reduced compressor work; in the latter case, additional fuel can be saved by recovering additional work from the pressure difference between the tank outlet and mGT injection point. For this application, the minimum allowed outlet pressure of the turbine is set to 4.5 bar, which is higher than the maximum pressure supplied by the T100 compressor in the considered operating points. The outlet pressure

can be controlled by a pressure valve at the outlet. The value of the Tesla rotational speed is a consequence of the mass flow rate and expansion ratio. In both cases, air pre-heating is always required to avoid temperatures close to or below 0°C, which could cause freezing problems. Due to its size, a Tesla turbine is a suitable device for being employed as an expander. In detail, it is a bladeless turbine that uses discs to exploit the adhesion and friction created by the working fluid. Good isentropic efficiencies can be reached, as demonstrated in different experimental studies [39,40]. However, in this work an isentropic efficiency equal to 30% is considered to obtain results based on the state-of-the-art of Tesla expanders, not on the latest results to be confirmed by further analyses. Traditional radial turbines would have low isentropic efficiencies under these operating conditions, with a small mass flow rate and low inlet temperatures. Moreover, the cost of Tesla turbines is lower, and it is more compact than radial turbines.

Table 3-1. CAES system design point specifications.

Specification	value	unit
Tank maximum pressure	50	bar
Compressor isentropic efficiency (equal for each stage)	85	%
Tesla isentropic efficiency	30	%
Intercooler effectiveness	89	%
Aftercooler effectiveness	87	%

3.2 Steady-state results

This steady-state analysis intends to investigate the behaviour of the micro gas turbine when stable part-load conditions are reached during constant air injection. The results presented in this section were calculated with the dynamic model presented in the previous chapter waiting for stable conditions for each operating point. Part load results are useful to analyse the system overall performance and identify some of the systems operating constrains as well as the impact of the air injection on the overall performance. This also allows for

the identification of potentially dangerous points for the following dynamic analysis.

3.2.1 Steady-state results at constant ambient temperature

Initially, the main steady-state performance parameters were obtained with an ambient temperature of 25 °C, imposing different values of injected compressed air. Some of these values are presented in Table 3-2. As mentioned in Paragraph 2.4, this specific micro gas turbine has an additional piping system since it was converted to work in a humified cycle. However, in this analysis the mGT was operated in dry mode. Because of these additional pressure losses, and since the considered ambient temperature was higher (25°C) than the nominal conditions (15°C), the produced maximum net power output (82.8 kW) and electrical efficiency (24.95%) were lower than the nominal conditions. Despite this, the analysis does not lose generality and the methodology could be applied to similar micro gas turbines.

The compressor stability is the main limiting factor for the maximum amount of air that can be injected upstream of the compressor. As already mentioned, a surge margin of 1.1 is considered as the lower limit for this analysis. During steady-state conditions, when working at constant net power output P_{net} and fixed TOT, the injection of air upstream of the compressor reduces the required compression work. Therefore, the turbine subtracts less power and requires less fuel flow, increasing the electrical efficiency. At the same time, the rotational speed, compressor mass flow and pressure ratio reduce, bringing the new operating point closer to the surge line. Since the regular operating points of the T100 at higher P_{net} have a higher surge margin, more air can be injected in those conditions compared to lower P_{net} conditions. Figure 3-2 shows the surge margin for different P_{net} and $\dot{m}_{inj}$ up to 60 g/s. Air cannot be injected below the minimum line represented in the graph. It is also worth noting that the injection of air can significantly increase the maximum power output that is reached at the maximum rotational speed of 70000 rpm. This is because the air injection leads to a reduction of the rotational speed. For example, by injecting 60 g/s of

compressed air, the maximum power output can reach 99.6 kW, around +17 kW compared to the maximum power output of this specific mGT at 25°C.

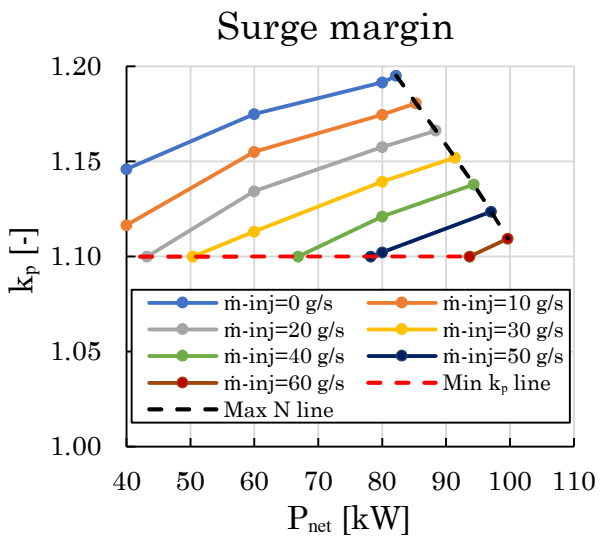

Figure 3-2. Surge margin for different P_{net} and $\dot{m}_{inj}$.

From the graph of Figure 3-2, the plots shown in Figure 3-3 can be obtained. These plots display the maximum mass flow that can be injected as a function of P_{net} and the maximum power output that can be achieved as a function of the injected mass flow for this specific machine.

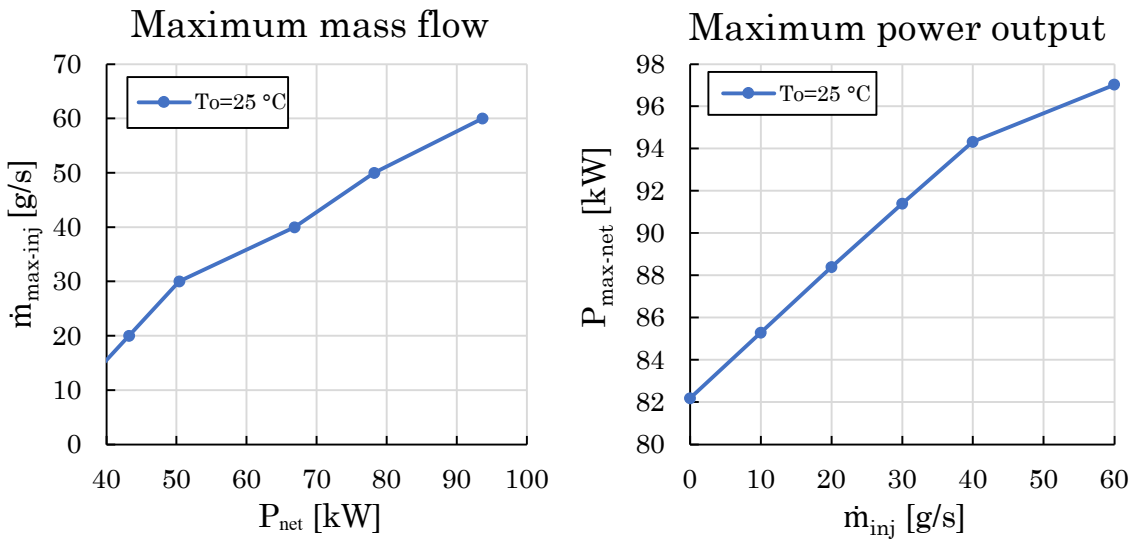

Figure 3-3. Maximum mass flow that can be injected as a function of the power output (left) and maximum power out as a function of the mass flow (right).

Steady-state results help to identify the limits during stable operations. These results are an important guide for designing the CAES/mGT integration extending the operative range of this commercial machine to the maximum operating limits and to avoid risk of failures. However, during transient variations, there could be operating conditions leading to potential compressor instability even when the injected mass flow is within the acceptable ranges in steady-state conditions. Therefore, a dynamic analysis is essential to evaluate the effective constraints to be considered in a real implementation. The most significant benefits in terms of increased electrical efficiency can be obtained by injecting air at higher P_{net} since the starting η_{el} is higher and more air can be injected due to the higher surge margin in standard operation. For example, by injecting the same air mass flow rate of $\dot{m}_{inj}$ = 10 g/s, at the low power output of P_{net}= 40 kW, the electrical efficiency increases by +0.51 %, and at the higher power output of P_{net}= 80 kW, the electrical efficiency increases by +0.74 % in absolute terms. In addition, at P_{net}= 40 kW the maximum increment of η_{el} is +0.76 % when $\dot{m}_{inj}$ = 15 g/s, while at P_{net}= 80 kW the maximum increment is +3.23 % at $\dot{m}_{inj}$ = 50 g/s. All the values of electrical efficiency and fuel mass flow are reported in Figure 3-4 as function of the injected compressed air.

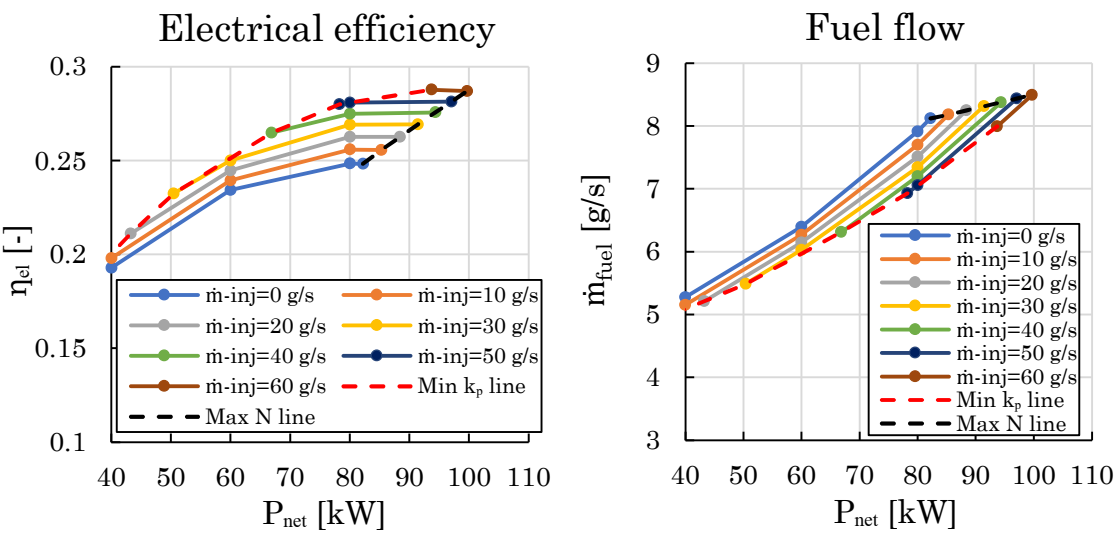

Figure 3-4. Electrical efficiency and fuel flow as function of the injected compressed air.

The results of Table 3-2 were obtained by injecting air at constant ambient temperature (T = 25°C); although during transient operation, the compressed air temperature can vary depending on the tank temperature, conditions of the heat exchanger used for the pre-heating and presence or not of the Tesla turbine. Injecting air at ambient temperature lowers the compressor outlet temperature by approximately between 2 - 4°C every 10 g/s of injected air due to the mixing with colder air. However, the recuperator can provide almost the same outlet temperature on the cold side (with a negligible variation of 0.1 - 0.3°C every 10 g/s of injected air) due to increased recuperator effectiveness as shown in Figure 3-5. At fixed power output, the recuperator effectiveness increases when the compressed air is injected into the mGT, due to the temperature reduction, resulting in an increased potential thermal flux that can be recovered, and due to the mass flow reduction, which makes the recuperator operate as an over-sized recuperator. The temperatures before and after the recuperator on the cold side (T_{c_out} and $T_{rec\_cold\_out}$) and temperature at the recuperator exhaust on the hot side ($T_{rec\_hot\_out}$) are reported in Table 3-2.

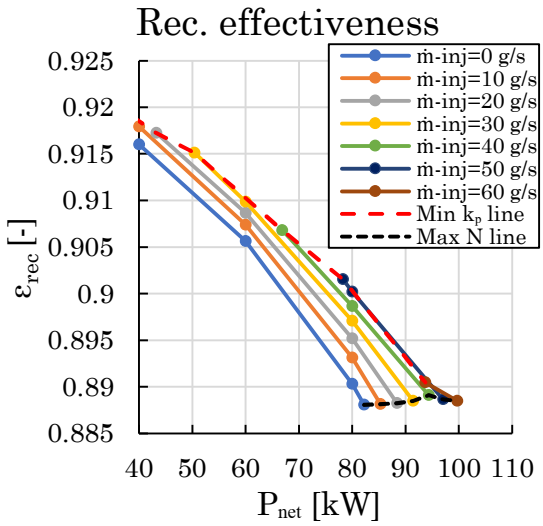

Figure 3-5. Recuperator effectiveness as function of the injected compressed air.

Therefore, the impact of possible temperature variations of the compressed air on the electrical efficiency is negligible and compressed air temperature

reductions do not affect the electrical efficiency. However, this effect causes a reduction of around 5°C every 10 g/s of injected air on the recuperator outlet temperature on the hot side, whose effect should be considered in determining the reduced thermal power. Moreover, the injected of air reduces the outlet mass flow (as reported in Figure 3-6, left). Therefore, the thermal power produced reduces due to both the air temperature and outlet mass flow reduction (Figure 3-6, right).

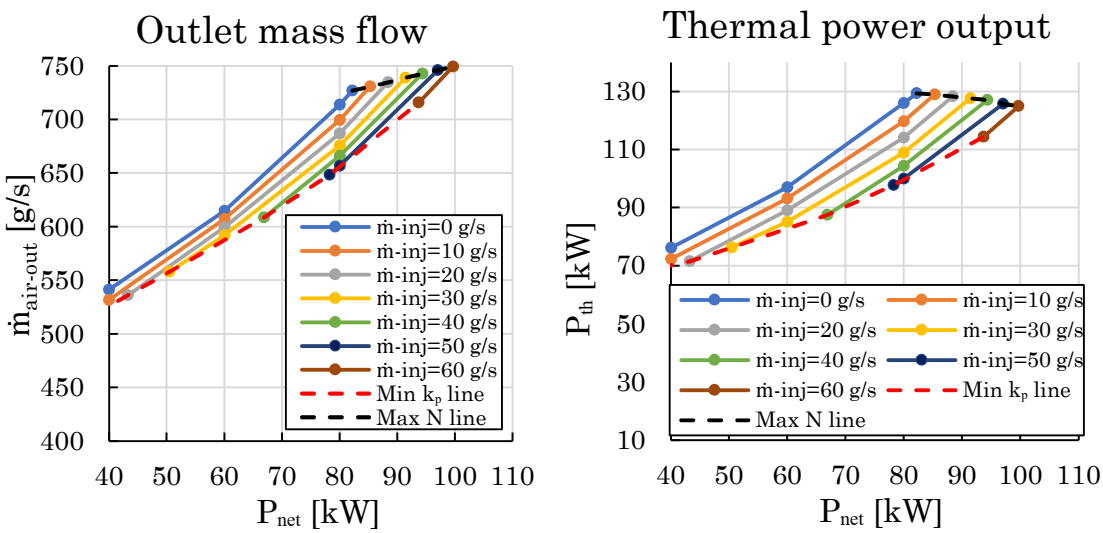

Figure 3-6. Outlet mass flow and thermal power output as function of the injected compressed air.

Table 3-2. Summary of the main steady-state performance points varying P_{net} and $\dot{m}_{inj}$.

P_{net} [kW]	$\dot{m}_{inj}$ [g/s]	η_{el} [%]	$\dot{m}_{fuel}$ [g/s]	N [rpm]	β_c [-]	T_{c_out} [°C]	$T_{rec\_cold\_out}$ [°C]	$T_{rec\_hot\_out}$ [°C]
40	0	19.28	4.774	60911	3.295	172.7	601.6	209.8
40	10	19.79	4.652	60345	3.242	170.3	601.6	205.0
40	15	20.04	4.594	60077	3.216	169.2	601.7	202.6
60	0	23.43	5.894	64885	3.763	192.3	601.6	227.1
60	10	23.93	5.770	64265	3.702	189.8	601.7	222.3
60	20	24.45	5.648	63664	3.641	187.4	601.8	217.5
60	30	24.98	5.528	63071	3.581	184.9	601.9	212.8
80	0	24.84	7.412	69515	4.363	215.7	597.0	245.6
80	10	25.58	7.198	68702	4.265	211.8	597.4	240.1
80	20	26.26	7.013	67934	4.181	208.6	597.7	235.1
80	30	26.90	6.844	67264	4.105	205.7	597.9	230.3
80	40	27.48	6.700	66703	4.042	203.3	598.1	225.8
80	50	28.07	6.559	66153	3.979	200.9	598.3	221.3

The results reported here are a good mapping of this CAES/mGT coupling with important impact on real system development and optimisation. For instance, the efficiency and fuel consumption change can be used to develop a simplified model (e.g. based on lookup tables) for the interaction with an optimisation algorithm.

3.3 Motivation of the dynamic analysis

As presented before, the aim of this chapter is to present the dynamic analysis related to the impact of the CAES system on the T100 microturbine focusing special attention on the constraints that in dynamic mode affect the operating range. No optimisation or management tools were initially developed, and no optimal operating results were obtained in this chapter (an optimisation toll will be discussed in the last results chapter). Here, to motivate this dynamic analysis a simple calculation is presented showing that the application of this CAES system can produce cost savings also in simple configurations.

Since the T100 operating range is around 20-100 kW for the electrical generation point of view and the extreme values are affected by further

limitations in the compressor surge margin and maximum rotational speed, a simple scenario was defined considering a low load of 40 kW for the first 12 hours (representative of off-peak hours) and 80 kW at a higher load for the remaining 12 hours (representative of core hours). The first 12 hours could represent night-time hours, for example, starting from 20:00 pm to 8:00 am, and the remaining hours from 8:00 am to 20:00 pm of daytime hours. This is a simple scenario, different from the reality, but useful to highlight a case with an evident positive impact of the CAES system. Therefore, the results proposed in this section are reported to motivate the following dynamic analysis and for real optimisation activities attention can be focused on the final chapter of the thesis.

The following possible configurations were considered for comparison (also summarised in Table 3-3):

1. The mGT alone satisfies the power demand; this case represents the baseline used for comparison against different CAES operations.
2. The plant consists of the mGT and small-size CAES charged during the night-time and discharged during the daytime – without Tesla (2) and with Tesla turbine (2-T).
3. The plant consists of the mGT and small-size CAES charged during the daytime and discharged during the night-time – without Tesla (3) and with Tesla turbine (3-T).

Table 3-3. Configurations description.

Case identifier	First 12 hours (off-peak hours)	Second 12 hours (core hours)
CASE:1 (BASELINE)	40 kW satisfied by the mGT only	80 kW satisfied by the mGT only
CASE: 2	40 kW satisfied by the mGT only, while CAES is charging	80 kW satisfied by the mGT, while CAES is discharging
CASE: 2 - T	40 kW satisfied by the mGT only, while CAES is charging	80 kW satisfied by the mGT and Tesla turbine, while CAES is discharging
CASE: 3	40 kW satisfied by the mGT, while CAES is discharging	80 kW satisfied by the mGT only, while CAES is charging
CASE: 3 - T	40 kW satisfied by the mGT and Tesla turbine, while CAES is discharging	80 kW satisfied by the mGT only, while CAES is charging

The chosen configurations were selected to compare two cases where the air is injected respectively at a higher load (80 kW) and lower load (40 kW). The selected injected mass flow rates are the maximum limits obtained from the steady-state analysis (to avoid not acceptable injected flows due to the surge limitation): if the discharge occurs during the daytime at P_{net}= 80 kW, the maximum mass flow considered in this evaluation is $\dot{m}_{inj}$ = 50 g/s, while if the discharge occurs during the night-time at P_{net}= 40 kW, the maximum mass flow used here is $\dot{m}_{inj}$ = 15 g/s. These numbers are considered to motivate the dynamic analysis and a further work considering an optimisation is proposed in the final chapter considering real power demand trends. The other goal of this comparison is to estimate the additional beneficial effect of including a Tesla turbine.

For cases 2 and 2-T (see Figure 3-7), the volume of the tank chosen is 40 m^3 to reach the maximum pressure of p_{max}= 50 bar during the charging time within the first 12 hours, when compressing the constant mass flow $\dot{m}_{charg}$ = 50 g/s, equal to the discharged mass flow . At t=12 hours, when the electrical demand increases from 40 kW to 80 kW, the mGT ramps up to satisfy the higher load and the injection starts after 15 minutes. The discharge stops when the tank reaches the minimum allowed pressure of p_{min}= 4.5 bar. The Tesla turbine recovers additional power when used, reducing the mGT required power production.

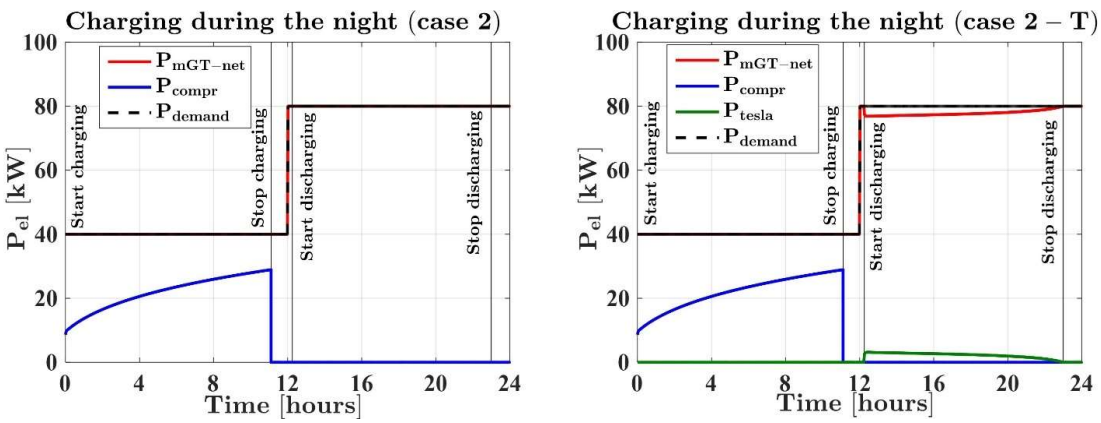

Figure 3-7. Power demand, power absorbed by the compressor and generated by the mGT and Tesla turbine for cases 2 (left) and 2-T (right).

For cases 3 and 3-T (see Figure 3-8), the chosen volume is smaller (12 m^3) since the mass flow during the charge $\dot{m}_{charge}$ = 15 g/s is lower and the comparison between cases is made by considering the same maximum tank pressure (p_{max} = 50 bar). In this scenario, at t=0 hours, the tank is fully pressurised at 50 bar and the discharging phase starts 15 mins after the start-up of the scenario. Also, in this case, the Tesla turbine allows for an additional energy recovery. The discharging phase stops some minutes before reaching 12 hours when the tank reaches p_{min}. At t = 12 hours, the mGT ramps up to provide 80 kW and at the same time, the reciprocating compressor starts to charge the storage volume where the air will be used in the following day.

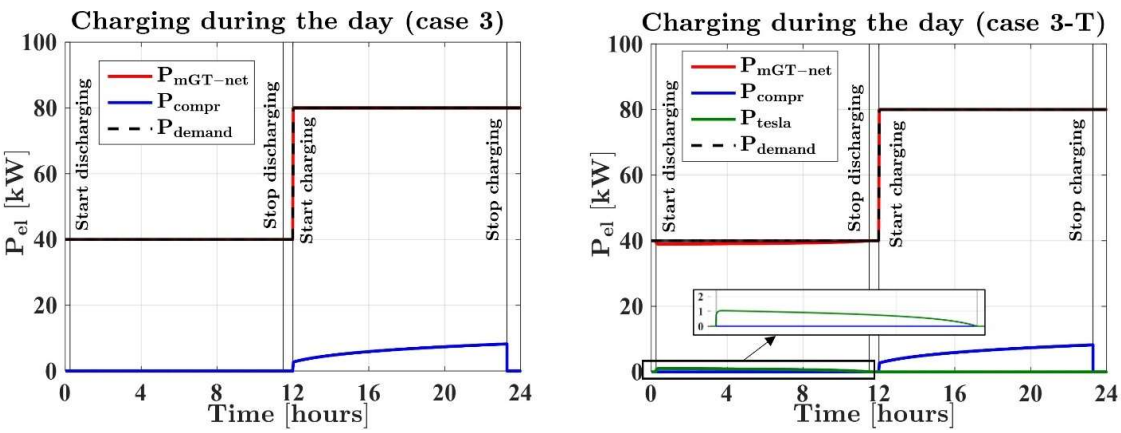

Figure 3-8. Power demand, power absorbed by the compressor and generated by the mGT and Tesla turbine for cases 3 (left) and 3-T (right).

The analysis of the different energy consumptions of these configurations, displayed in Figure 3-9, shows that thermal energy provided by the fuel ($E_{th\text{-}fuel}$) can be saved when coupling the mGT with a CAES system at the expense of a higher electrical energy ($E_{el\text{-}used}$) required to run the compressor to charge the tank. Additionally, the Tesla turbine provides further fuel savings as the mGT provides less power compared to the case without the Tesla expander. The results reported in Figure 3-9 regard the simple scenario presented in this section with the aim to motivate the importance of the dynamic analysis also from economic point of view.

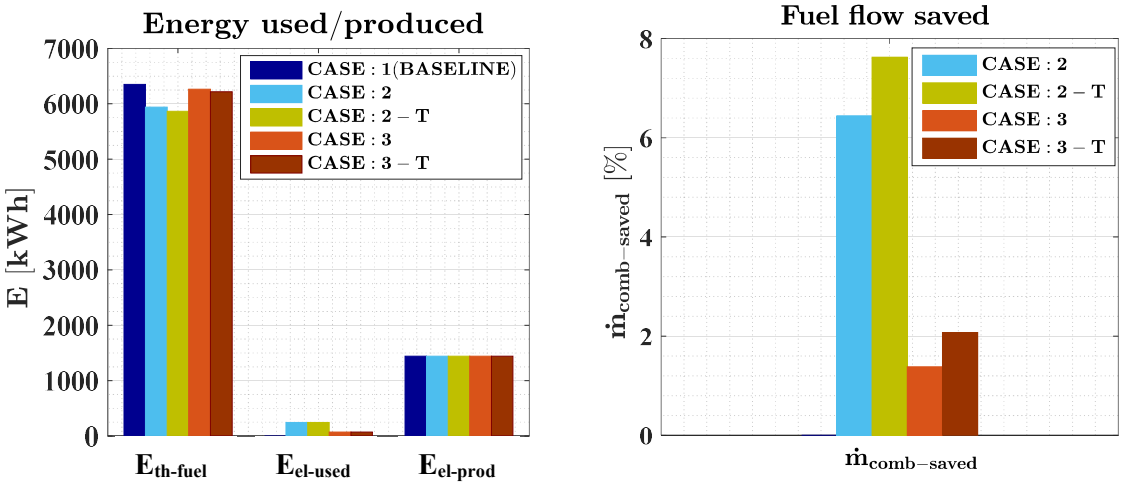

Figure 3-9. Energy used and produced comparison (left) and fuel flow saved (right).

Defining the electrical source for running the compressor while charging is required to estimate the potential economic benefits. In this study, it is considered that the CAES system could be charged in two different ways by using the following:

1. Purchased electrical energy from the grid.
2. Excess of electrical energy from renewable sources.

When purchasing electrical energy from the grid, there are no issues related to the availability of the energy, and the charging can be done at any time of the day. However, the availability of renewable energy sources depends on the weather conditions. Therefore, the charging during the day (cases 3 and 3-T) could be done by both wind and solar energy, while the charging during the night (cases 2 and 2-T) only by wind sources. Below, the two cases are considered.

3.3.1 Electrical energy for the storage charge from the grid

Table 3-4 includes the average costs of natural gas and electricity for the year 2022 (first semester) for three European countries (Italy, Moldova and Sweden) taken as examples [50,51]. These countries are taken into account for these

evaluations to compare a case with high electricity price (Italy) with countries with lower cost for electricity but with different prices for the natural gas (high in Sweden and low in Moldova). Table 3-4 also includes the ratio between fuel cost and electricity cost ($ratio_{fuel/el\text{-}cost}$) to analyse how the different cases mutually compare.

Table 3-4. Electricity and natural gas cost for the first semester of 2022 [50,51].

Country	El. cost [€/kWh]	Fuel cost [€/kWh]	$ratio_{fuel/el\text{-}cost}$ [-]
Italy	0.3115	0.0986	0.316
Moldova	0.1172	0.0842	0.718
Sweden	0.2525	0.2216	0.877

Table 3-5 displays the daily fuel cost, daily electricity cost, daily earnings, total daily cost, daily savings, and relative daily savings compared to the baseline for each case in each country. These results were obtained by combining the energy consumption results of Figure 3-9 and the electricity and natural gas costs of Table 3-4. For the scenario presented here, the CAES system leads to money savings when the daily and relative savings are positive. The savings are also graphically reported in Figure 3-10 (when having a positive value means that there are savings compared to the baseline condition). This configuration can provide economic savings in countries such as Moldova and especially in Sweden, where the fuel cost is high relatively to the electricity cost (Table 3-5). On the contrary, adding a CAES system would always result in a loss of revenues for Italy since the fuel cost is lower compared to the electricity cost. Therefore, for Moldova and Sweden, it is better to buy more electricity to compress the air (Cases 2 and 2-T). Case 2-T is the best and Case 3 the worst in these countries. For Moldova, only Case 2-T can provide significant relative energy savings (+3.3%), while for Sweden, both Cases 2 and 2-T provide good results, with energy savings of +2.8% and + 4.4%, where the increment of 1.6%

is due to the Tesla turbine. Sweden has the highest total daily cost, but in Case 2-T, it also has the highest daily savings and relative daily savings compared to all other cases, meaning that this technology has more potential for implementation in this country. For Italy, in this scenario there is always a loss when integrating the CAES system, which increases by increasing the electricity bought from the grid.

Table 3-5. Daily costs and earnings when purchasing electricity from the grid.

	Case identifier	Daily fuel cost [€/day]	Daily electricity cost [€/day]	Daily-earnings [€/day]	Total daily cost [€/day]	Daily savings [€/day]	Relative daily savings [%]
Italy	**CASE:1 (BASELINE)**	626.2	0.0	448.5	177.8	-	-
	CASE: 2	585.9	75.9	448.5	213.3	-35.6	- 20.0
	CASE: 2 - T	578.5	75.9	448.5	205.9	-28.2	- 15.8
	CASE: 3	617.6	22.2	448.5	191.3	-13.5	- 7.6
	CASE: 3 - T	613.2	22.2	448.5	187.0	-9.2	- 5.2
Moldova	**CASE:1 (BASELINE)**	534.8	0.0	168.7	366.0	-	-
	CASE: 2	500.3	28.6	168.7	360.1	+5.9	+ 1.6
	CASE: 2 - T	494.0	28.6	168.7	353.8	+12.2	+ 3.3
	CASE: 3	527.4	8.3	168.7	367.0	-1.0	- 0.3
	CASE: 3 - T	523.7	8.3	168.7	363.3	+2.7	+ 0.7
Sweden	**CASE:1 (BASELINE)**	1407.4	0.0	363.5	1043.9	-	-
	CASE: 2	1316.7	61.5	363.5	1014.7	+29.2	+ 2.8
	CASE: 2 - T	1300.1	61.5	363.5	998.1	+45.8	+ 4.4
	CASE: 3	1388.0	18.0	363.5	1042.4	+1.5	+ 0.1
	CASE: 3 - T	1378.3	18.0	363.5	1032.7	+11.2	+ 1.1

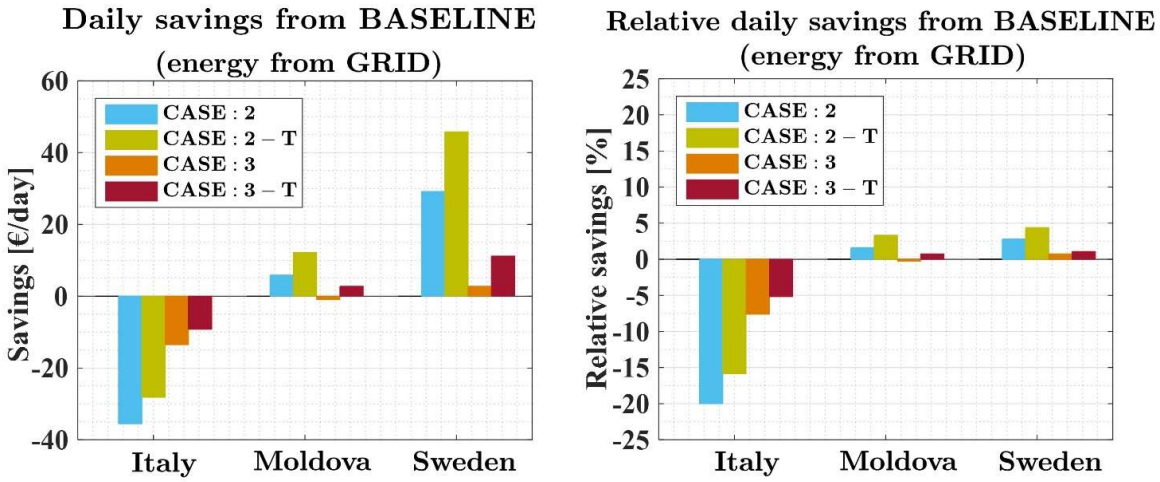

Figure 3-10. Daily savings compared to the baseline case when energy is bought from the grid.

3.3.2 Electrical energy for the storage charge from an excess of RES

The CAES system always provides relative economic savings when using excess of renewable energy sources, especially when fuel prices are high (Table 3-6). The results show that Case 2-T provides the highest daily savings and Case 3 the lowest compared to the baseline in all three countries. Therefore, in all the countries, significant benefits are obtained when injecting the maximum mass flow rate of 50 g/s at 80 kW with the expansion in the Tesla turbine. The daily and relative daily savings (in this scenario) compared to the baseline are also graphically reported in Figure 3-11. For Italy, compared to the previous case, higher relative daily savings (+22.7% for Case 2-T) can be obtained compared to the other countries due to the lower daily total cost. In absolute values, the daily savings for Moldova are the lowest and for Sweden the highest (Figure 3-11, left). However, they have comparable relative daily savings as Moldova's total daily costs are lower than those of Sweden.

Table 3-6. Daily costs and earnings when using an excess of renewables.

	Case identifier	Daily fuel cost [€/day]	Daily electricity cost [€/day]	Daily-earnings [€/day]	Total daily cost [€/day]	Daily savings [€/day]	Relative daily savings [%]
Italy	**CASE:1 (BASELINE)**	626.2	0.0	448.5	177.8	-	-
	CASE: 2	585.9	0.0	448.5	137.4	+40.4	+22.7%
	CASE: 2 - T	578.5	0.0	448.5	130.0	+47.8	+26.9%
	CASE: 3	617.6	0.0	448.5	169.1	+8.7	+4.9%
	CASE: 3 - T	613.2	0.0	448.5	164.8	+13.0	+7.3%
Moldova	**CASE:1 (BASELINE)**	534.8	0.0	168.7	366.0	-	-
	CASE: 2	500.3	0.0	168.7	331.6	+34.5	+9.4%
	CASE: 2 - T	494.0	0.0	168.7	325.3	+40.8	+11.1%
	CASE: 3	527.4	0.0	168.7	358.6	+7.4	+2.0%
	CASE: 3 - T	523.7	0.0	168.7	355.0	+11.1	+3.0%
Sweden	**CASE:1 (BASELINE)**	1407.4	0.0	363.5	1043.9	-	-
	CASE: 2	1316.7	0.0	363.5	953.2	+90.7	+8.7%
	CASE: 2 - T	1300.1	0.0	363.5	936.6	+107.3	+10.3%
	CASE: 3	1388.0	0.0	363.5	1024.5	+19.4	+1.9%
	CASE: 3 - T	1378.3	0.0	363.5	1014.7	+29.2	+2.8%

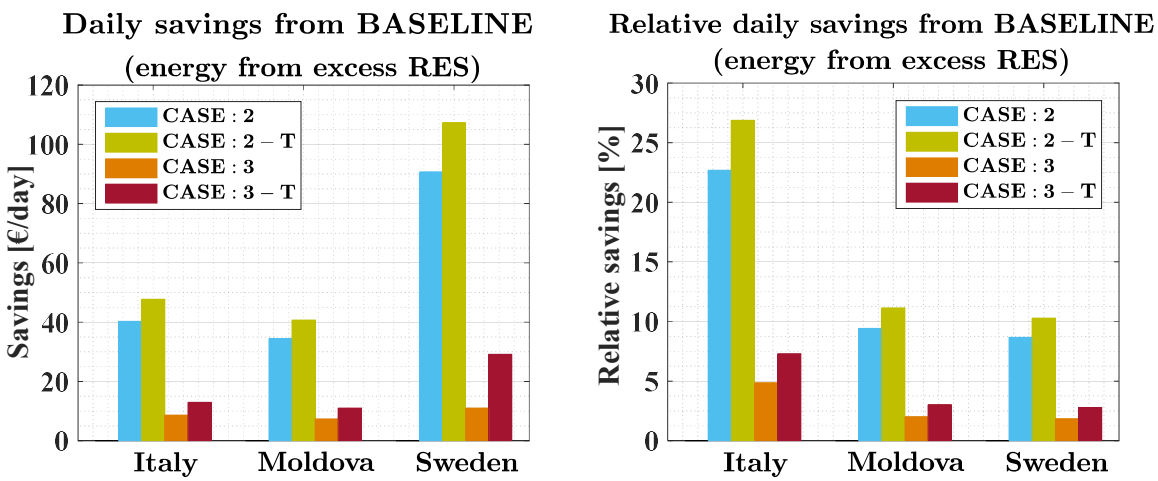

Figure 3-11. Daily savings compared to the baseline case when energy is taken from excess of renewables.

3.3.1 General considerations on the capital costs

In the previous analysis, the additional capital costs of the system were not considered since the aim of this work is to perform a dynamic analysis on the system and understand the interaction between the CAES system and mGT. For this reason, the system layout was selected based on a previous study conducted by Arnulfi et al. [64]. However, as the capital costs can determine the success or failure of a specific technology on the market, this paragraph provides a high-level analysis on the CAES system CAPEX. This analysis should not be considered as a technoeconomic analysis - that would require a more in-depth analysis on different electrical and thermal demands of typical days of the year - but it should be considered as a guide to understand the order of magnitude of costs that can be expected from the installation of a small-size CAES system.

Different alternatives are available for the compressed air man-made storage systems such as pressurised vessels, concrete or steel pipes. As suggested by [66,131,132], an air storage made of sections of large diameter steel pipe connected by manifolds is the most cost effective solution for pressures up to 150 bar. The storage system has been sized considering the ANSI standard by using 30" OD, 12 m length ANSI b.125.1 carbon steel pipe sections. The storage cost has been evaluated with the same approach considered by Salvini [66], considering the steel pipe purchase cost (0.8 €/kg), shipping cost (30% of purchase cost), installation costs (applying a factor of 1.5 to the base cost). For simplicity the welding costs have been neglected. The compressor cost has been estimated considering solutions available on the market based on the absorbed power by the compressor and delivery pressures [133]. The cost analysis results are shown in Table 3-7.

Table 3-7. CAES cost analysis results.

	Design pressure	Tank volume	Pipe thickness	Pipe overall length	Tank mass	Max compr. absorbed power	Tank cost	Compr. cost	Total cost
	[bar]	[m3]	[mm]	[m]	[kg]	[kW]	[€]	[€]	[€]
Case 2 and 2-T	50	40	19.84	87.48	16118	28.9	19922	27350	47272
Case 3 and 3-T	50	12	19.84	26.24	4835	8.2	5976	3646	9622

In a simplified scenario, if considering the same daily savings from each day over a lifetime of 20 years, it is possible to calculate the savings over the system lifetime and the net savings over the lifetime (subtracting the system CAPEX). These results are shown in Table 3-8 considering both cases when electricity is purchased from the grid or obtained from an excess of renewable electricity production. Despite the higher capital costs of case 2 and 2 – T, it is always more profitable to operate on those conditions due to the higher reduction of the operational costs during the system lifetime.

Table 3-8. Net savings over lifetime considering capital costs when electricity is purchased from the grid or from an excess of renewable production.

	Case identifier	Electricity purchased from the grid			Electricity from excess of renewables		
		Daily savings	Savings over lifetime	Net savings over lifetime	Daily savings	Savings over lifetime	Net savings over lifetime
		[€/day]	[€]	[€]	[€/day]	[€]	[€]
Italy	CASE:1 (BASELINE)	-	-	-	-	-	-
	CASE: 2	-36	-259'880	-307'152	40	294'920	247'648
	CASE: 2 - T	-28	-205'860	-253'132	48	348'940	301'668
	CASE: 3	-14	-98'550	-108'172	9	63'510	53'888
	CASE: 3 - T	-9	-67'160	-76'782	13	94'900	85'278
Moldova	CASE:1 (BASELINE)	-	-	-	-	-	-
	CASE: 2	6	43'070	-4'202	35	251'850	204'578
	CASE: 2 - T	12	89'060	41'788	41	297'840	250'568
	CASE: 3	-1	- 7'300	-16'922	7	54'020	44'398
	CASE: 3 - T	3	19'710	10'088	11	81'030	71'408
Sweden	CASE:1 (BASELINE)	-	-	-	-	-	-
	CASE: 2	29	213'160	165'888	91	662'110	614'838
	CASE: 2 - T	46	334'340	287'068	107	783'290	736'018
	CASE: 3	2	10'950	1'328	19	141'620	131'998
	CASE: 3 - T	11	81'760	72'138	29	213'160	203'538

3.4 Dynamic analysis

This paragraph investigates the influence of the injection of air and load change during CAES discharging on the dynamic performance of the mGT. The second configuration, with a tank size of V_{tank}= 40 m^3, has been chosen due to its higher economic potential in the considered scenarios. Different representative possible transient scenarios have been considered when operating with a CAES system:

1. Step injections of compressed air at constant power (for P_{net}= 40 kW and P_{net} = 80 kW)
2. Step and gradual injections at constant power (for P_{net}= 80 kW)
3. Step and gradual stop of injections at constant power (for P_{net}= 80 kW)
4. Step injection with gradual power output variation from 40 kW to 80 kW

Each case starts from a stable condition at t = 0 s, while the operating conditions change begins at t = 100 s.

3.4.1 Step injections of compressed air at constant power (for P_{net} = 40 kW and P_{net} = 80 kW)

The effect of the introduction of compressed air with a direct stepwise injection at constant power output was considered for a lower (P_{net}= 40 kW) and higher load (P_{net}= 80 kW). A direct stepwise injection represents the theoretical most critical condition. In a real application, some time is required for the flow rate to reach the requested value. However, this time is relatively short (around 1-2 seconds). Therefore, a similar behaviour of the system is expected compared to this theoretical case.

More air can be injected at a higher load since the starting surge margin (without injection) is higher than at a lower load. In both cases, the surge margin is initially reduced during the injection before reaching stable conditions (Figure 3-12). This effect is more noticeable at P_{net} = 80 kW and leads to a reduction of k_p below 1.1 when $\dot{m}_{inj}$ = 50 g/s is injected, which would have been acceptable considering the steady-state results. This reduction is due to the control system

action: when the air is injected, the power output initially increases, the control system reduces the rotational speed and, therefore, the compressor mass flow reduces with a fast response, while the pressure ratio remains high for a longer time before reducing as well. In detail, the pressure ratio initially increases before settling since the initial reduction of the TOT, due to the air injection, leads the control system to initially increase the fuel flow. This also contributes to the initial peak of produced power (Figure 3-13). The graphs of Figure 3-13 represent the generated power P_{gen} that considers the power used by auxiliaries. The TOT transient behaviour of Figure 3-14 shows a peak before stabilising to 645°C; however, the machine can handle a maximum value of 655°C for a few seconds and therefore, no potential problems due to thermal gradients have been detected.

These results mainly show that 50 g/s of air injection step is not acceptable at high load and 15 g/s of air injection step could be critical at low load, because an oscillation too close to the surge margin limit could be a risk. Since this significantly reduces the operating margin in comparison with the steady-state results, a different approach needs to be developed for a real application, to avoid to decrease the positive impact in terms of cost decrease and efficiency increase.

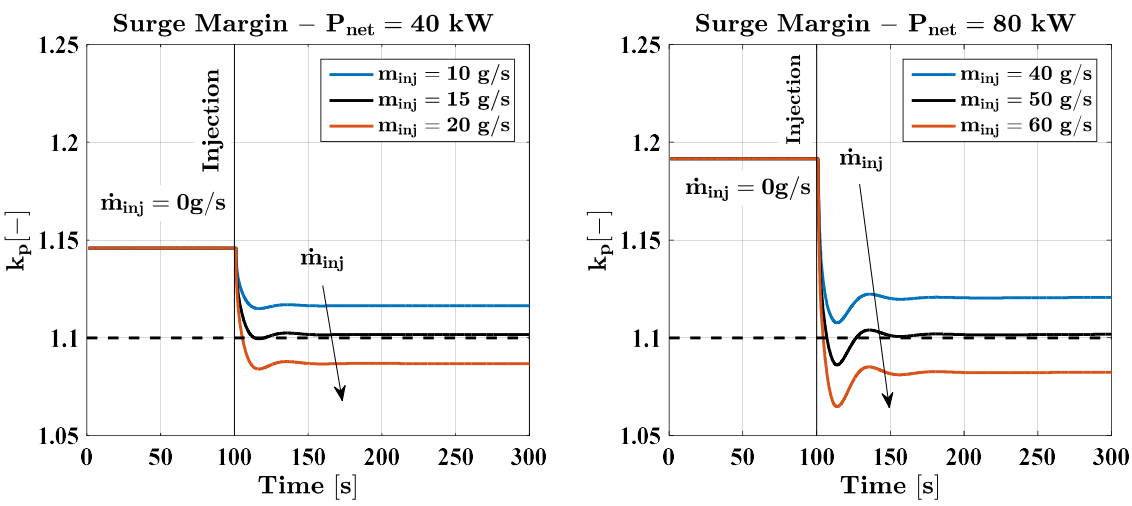

Figure 3-12. Surge margin variation when injecting compressed air at P_{net}= 40 kW (left) and 80 kW (right).

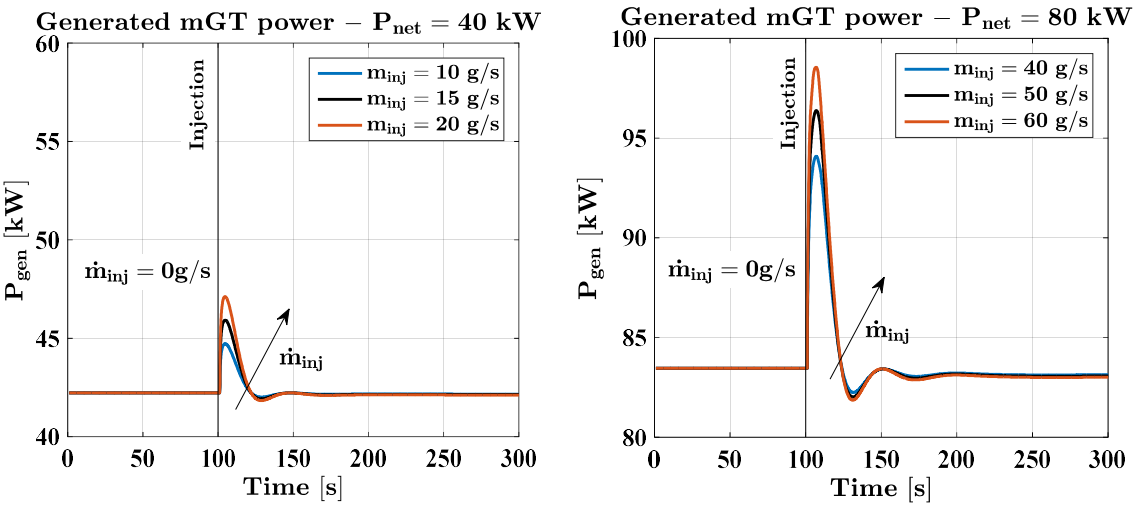

Figure 3-13. Generated mGT power variation when injecting compressed air at P_{net}= 40 kW (left) and 80 kW (right).

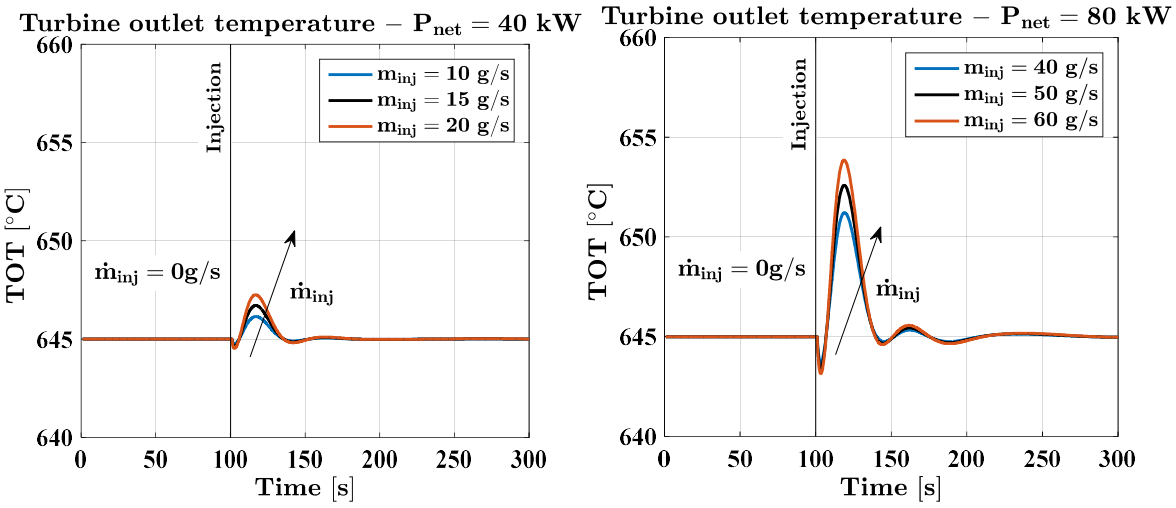

Figure 3-14. TOT variation when injecting compressed air at P_{net}= 40 kW (left) and 80 kW (right).

3.4.2 Step and gradual injections at constant power (for P_{net} = 80 kW)

Due to the critical dynamic behaviour when injecting the maximum allowed injection rate obtained for the steady-state conditions, different injection ramps

were considered by progressively reducing the rate of injection (Figure 3-15). This could be an important solution (coming from this dynamic analysis) to be implemented in a real CAES/mGT system. The case with P_{net}= 80 kW was chosen for this analysis as being the most critical. For example, with a rate of +0.5 (g/s)/s, it is always possible to ensure $k_p > 1.1$. Reducing the injection rate allows the k_p to stay within the acceptable limits and, therefore, to introduce a higher mass flow of injected air, benefiting the system overall performance. This also reduces the power and TOT oscillations with a smoother transition to the steady-state condition. Since the generated power peak is also reduced, more stable power output is provided to the grid. So, with the proposed ramp, a real commercial T100 could be used in the full operative range defined in the steady-state analysis without further limitations.

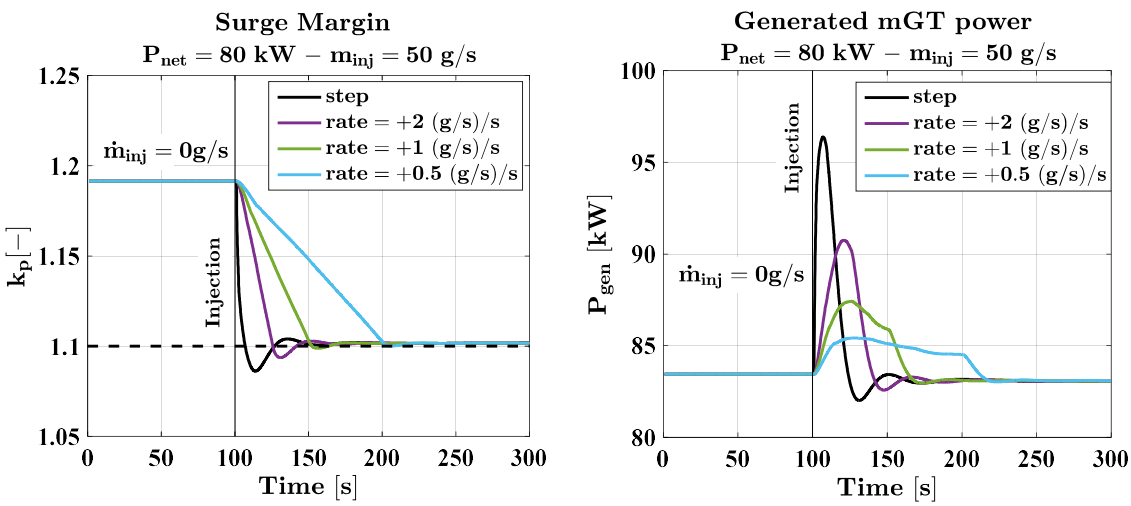

Figure 3-15. Surge margin (left) and generated mGT power (right) for step and gradual injections at constant power (for P_{net}= 80 kW).

3.4.3 Step and gradual stop of injections at constant power (for P_{net}= 80 kW)

Despite being less critical, it is also worth studying the dynamic behaviour at the moment where the injection is stopped. During the stop of the air injection, an opposite transient behaviour can be noticed (Figure 3-16). The surge margin and TOT values are never critical, even when the air injection suddenly stops.

However, considering the produced power, also in this case, a beneficial effect can be shown when gradually reducing the injected air to ensure a more stable power production. So, also in this case, the proposed ramp for removing the air injection is a positive solution to decrease the stress on the commercial machine extending the component duration.

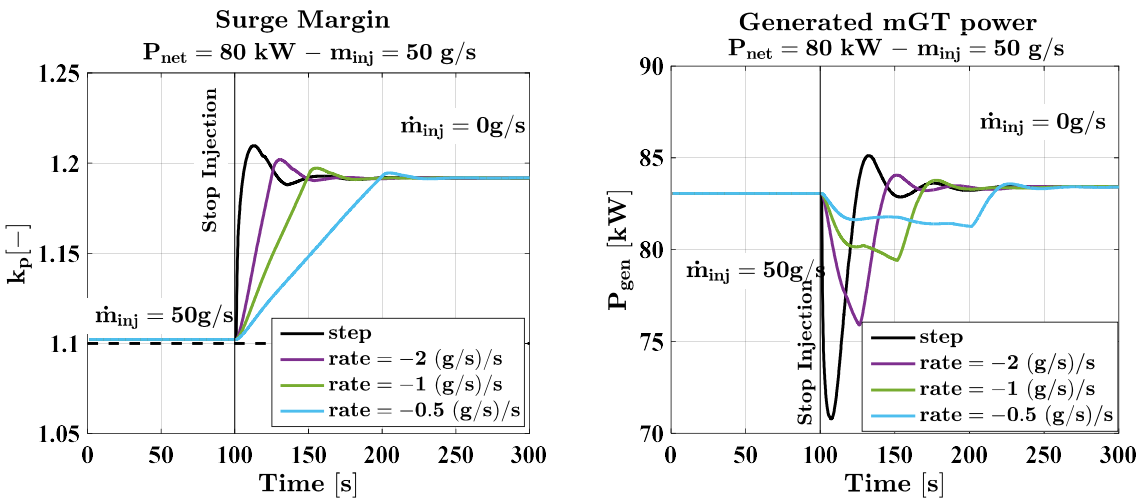

Figure 3-16. Surge margin (left) and generated mGT power (right) for step and gradual stop of injections at constant power (for P_{net}= 80 kW).

3.4.4 Step injection with gradual power output variation from 40 kW to 80 kW

A final case is investigated where a power output variation coincides with the start of the injection. In this case (see Figure 3-17), the injection was performed with a step of 50 g/s while the power output was gradually changed from 40 kW to 80 kW with a ramp of 1 minute. The surge margin plot shows that there is a significant reduction. This demonstrates that the injection schedule should not be performed during critical power change variations, and a waiting time should be considered. This is an important result to be applied in a real system because a waiting time (between the power and the air injection variations) of at least 2-3 minutes can prevent the superimposition of two transient operations and avoid the machine failure.

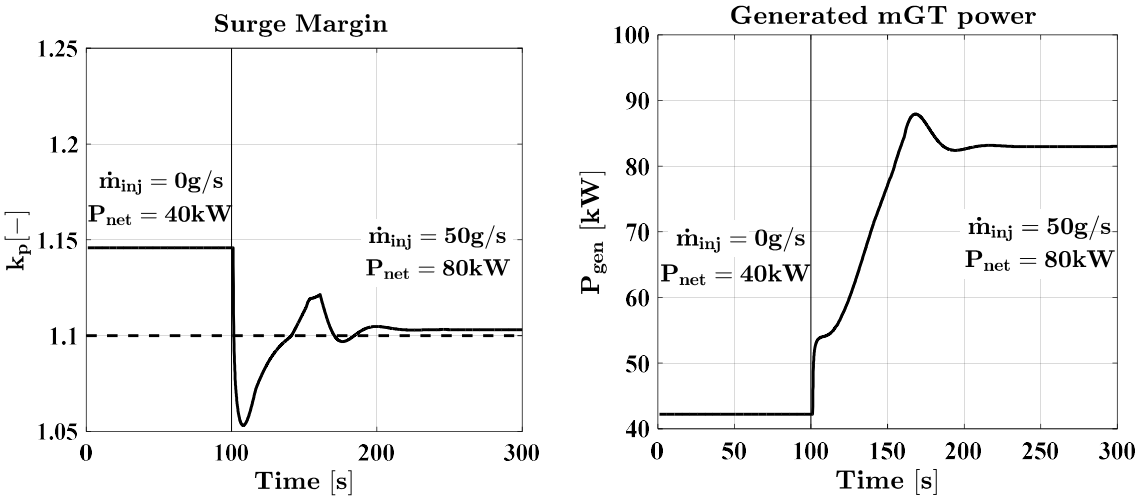

Figure 3-17. Surge margin (left) and generated mGT power (right) for step injection with gradual power output variation from 40 kW to 80 kW.

3.5 Conclusions

This chapter presents a dynamic analysis on an T100 micro gas turbine coupled with a small-size second-generation CAES system. It consists of a two-stage reciprocating compressor with intercooling and aftercooling, an artificial vessel for storing compressed air and an additional recuperator for air pre-heating. The application of a Tesla turbine placed after the storage vessel is also investigated for additional power recovery. The main results obtained in this work are able to extend the T100 applications in a CAES system with the following positive impacts on energy sustainability: efficiency increase, fuel consumption decrease, energy cost decrease, flexible energy storage for renewable sources. Special attention is focused on the calculation of the system integration constraints to prevent risks for the microturbine also in dynamic conditions and the related definition of operating procedures (ramps instead of steps) to enlarge the system flexibility to the maximum limits in terms of air flows injected in the T100 ducts.

The analysis begins with a steady-state study examining the micro gas turbine behavior when injecting compressed air at different part-load conditions. This analysis estimated the maximum mass flow rate that could be injected into the

micro gas turbine at different power outputs, ensuring safe operation of the compressor. This showed that higher mass flow rates can be injected at higher power outputs. For example, at P_{net}= 80 kW, the maximum mass flow rate is $\dot{m}_{inj}$ = 50 g/s resulting in an increment of the electrical efficiency of +3.23%, while at P_{net} = 40 kW, the maximum mass flow for discharge is $\dot{m}_{inj}$ = 15 g/s allowing a +0.76% of increment in efficiency.

The dynamic analysis of the micro gas turbine when operated with a compressed air energy storage (CAES) system is conducted. Results show that the surge margin is reduced during the step injection before reaching stable conditions, even in conditions acceptable for steady-state operations. The reduction is more pronounced at a higher load and injection rates. So, this analysis calculated that, considering injection steps, 50 g/s of air injection is not acceptable at high load and 15 g/s of air injection could be critical at low load, due to an oscillation too close to the surge margin limit. However, operating injection ramps instead of steps is a solution to keep the surge margin within acceptable limits and reduce power and TOT oscillations. In details, a rate of +0.5 (g/s)/s was calculated as a good compromise to operate the microturbine changes safely and fast in dynamic mode, without reducing the operating range related to the steady-state calculations.

Finally, the results obtained in this work will be important to manage this mGT/CAES system for commercial applications, avoiding dangerous operating procedures and situations, and proposing a calculation approach that can be repeated in case of other types of microturbines. In details, the definition of the air injection constraints and the ramp rates for safe operations allows to extend the system operative range to the calculated limits with a positive impact on the flexibility and the energy sustainability issues (fuel consumption decrease and flexibility increase for the variability compensation of renewable sources and the related positive impact on pollution and energy cost decrease).

4 Steady-state and dynamic analysis of the T100 with fuel composition change

4.1 Plant layout

The T100 traditional combustor is fired with natural gas through two separate injection lines: the pilot and the main line. A small percentage of fuel is provided by the pilot line, while the remaining is injected into the main line to operate the combustor in premixed lean conditions. The fraction of natural gas injected in the pilot is used for the ignition of the start-up process and to ensure flame stability during normal operating conditions, where an almost constant fuel flow is provided. The fuel injected into the main line has the most consistent variations and it is regulated by the control system to obtain the desired power output depending on the varying demand.

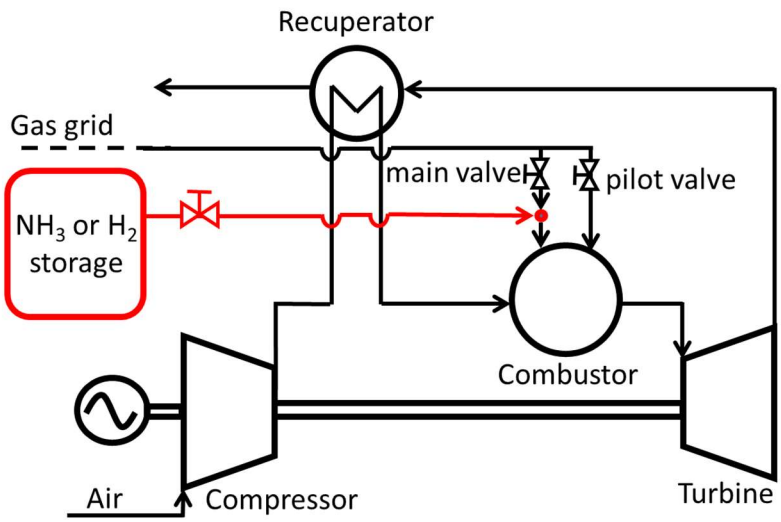

Figure 4-1: T100 layout with injection of H_2 or NH_3.

The T100 original layout has been modified according to Figure 4-1, where hydrogen or ammonia can be injected in the fuel line of the main burner, downstream of the natural gas fuel valve. In this configuration, the pilot line always supplies natural gas, while the main line can provide mixtures of natural gas and H_2 or NH_3 (depending on the considered storage solution). This solution does not require variations on the original control system, because the

regulation of the machine during transient manoeuvres can still be performed acting on the main valve. For example, staring from a stable operating condition with 100 % of NG, the injection of an amount of H_2 or NH_3 in the mGT main line, leads to a TIT rise, regardless of the LHV of the fuel, due to the overall increased fuel mass flow. This also leads to a consequent rise of the TOT. However, after a settling time, the control system can restore the TOT set point value by reducing the NG fuel flow in the main line. It should be noted that there is a limit to the maximum amount of additional fuel (H_2 or NH_3) that can be injected though the main line. The reason for this is that the pilot line always supplies an amount of natural gas and that a small fraction of natural gas should also be available for the TOT regulation.

The aim of this chapter is to study mGT behaviour at a system level. For this reason, a study on combustion performance and emission reduction is not tackled in this analysis and it is assumed that stable combustion is obtained without limitations on the amount of hydrogen or ammonia in blend with natural gas. However, a combustor re-design is required in presence of a high content of H_2 and NH_3 due to their different combustion properties and it should be addressed in future studies. The combustor redesign also includes the use of different fuel injectors, especially if ammonia is injected since the actual main injector allows to inject a maximum of 7.7 g/s of fuel.

4.2 Steady-state results

Steady-state off-design results were obtained at the ambient temperature of 25°C, in different power ranges, imposing several molar concentrations of H_2 and NH_3. This was done to calculate the amounts of required fuel mass flow rates of H_2 and NH_3 to be injected for the transient analyses and to calculate the maximum amount of fuel that can be injected in the main line at different power conditions. As previously mentioned, in the considered plant layout and with the considered traditional control system, there are some specific limits on the amount of H_2 and NH_3 that can be injected into the combustion chamber. This is because it is assumed that the NG is always injected in the pilot line. In

addition, for safe operations there should always be an amount of NG flowing through the main valve to regulate the TOT if there is an external disturbance. Although this solution is not completely carbon-free, it can still enable a reduction of CO_2 emissions, depending on the carbon content of the mixture. The advantage of keeping an amount of natural gas in the blend is the possibility to leave the control system almost unvaried when retrofitting the micro gas turbine for fuel flexible operation. In the configuration proposed in this study, it is not required to significantly modify the control system since the machine regulation can be performed acting on the natural gas fuel valve.

These limitations related to the maximum H_2 or NH_3 due to the control system requirements will be considered in transient analysis. However, for completeness, the steady-state results are provided also in the case it was possible to inject H_2-NG and NH_3-NG from the pilot so that 100% of H_2 and NH_3 could be reached in both cases.

For the injection of the fuel, constant temperature hydrogen is injected at 15°C and ammonia at 30 °C (and pressure of 10 bar). In the calculation of the power, no higher losses through the compression of the fuel are considered as it is assumed that the fuel is already at the desired conditions obtained from the power-to-fuel conversion system. The compression work of the natural gas in still considered and subtracted from the total power output.

Figure 4-2 displays the total fuel mass flow respectively for the H_2-NG and NH_3-NG blends. The presented operating points were obtained keeping the net power output constant. The reduction of the overall fuel mass flow when injecting H_2 and the increment when injecting NH_3 are due to the respective increase and decrease of the LHV.

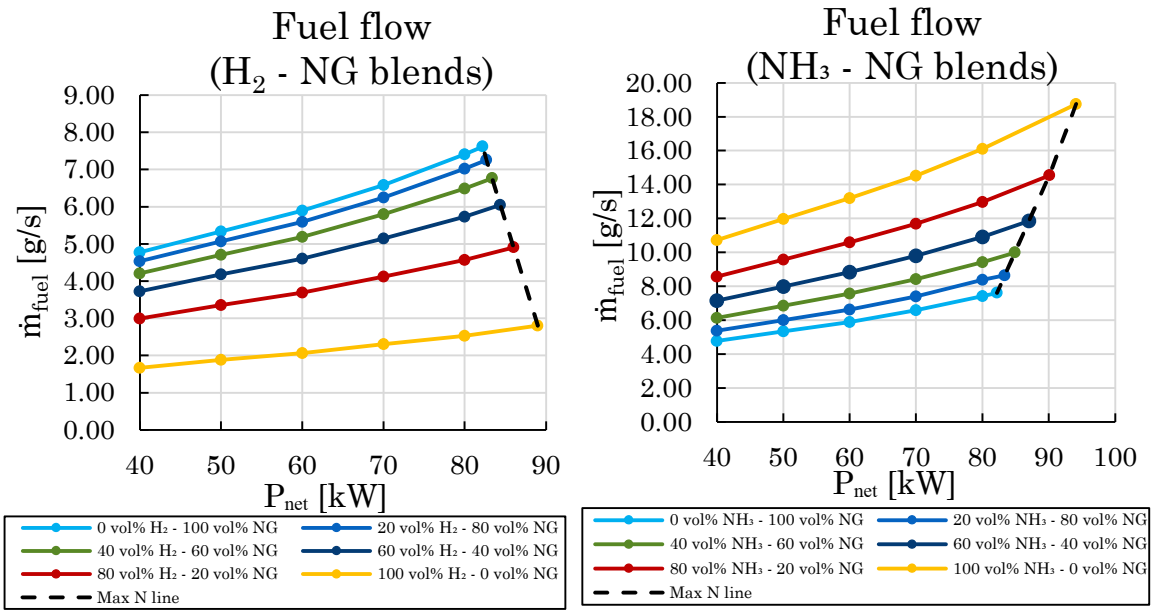

Figure 4-2: Off-design fuel mass flow for different hydrogen and ammonia molar concentrations.

Regarding the rotational speed, Figure 4-3 depicts that for the H_2-NG blends, the rotational speed slightly reduces due to a reduction of the required overall mass flow to achieve the same power output. This is due to a combined effect of the reduction of fuel flow and the increment of the heat capacity of the flue gases. For the NH_3-NG blends, the rotational speed reduction is less noticeable. In this case the mass flow reduction is due to the increment of the heat capacity whose effect prevails from the increment of fuel flow.

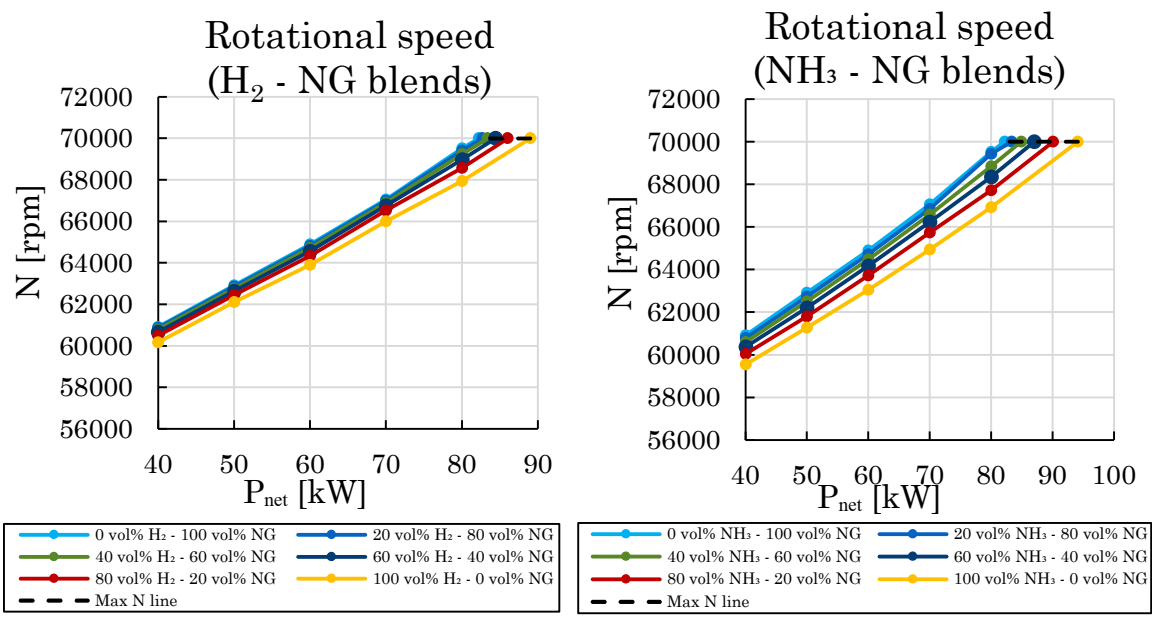

Figure 4-3: Off-design rotational speed for different hydrogen and ammonia molar concentrations.

The reduction of the rotational speed has a positive impact on the mGT causing a slight increase in the maximum power output: with 100% of H_2 it is possible to reach a maximum of 88.9 kW (+6.1 kW compared to the baseline of 82.8 kW), and with 100% of NH_3 a maximum of 94.1 kW can be obtained (+ 11.3 kW from the baseline). Table 4-1 summarises the main steady-state performance parameters when operating the mGT with 100% of NG, H_2 and NH_3 at the maximum power output. Along with the increased power output, another positive impact is the increase of the electrical efficiency due to the higher specific heat at the exhaust and the reduced work of the NG compressor.

Table 4-1: Summary of the main steady-state performance points at the maximum rotational speed at using 100% of NG, H_2 and NH_3.

Fuel	P_{net} [kW]	N [rpm]	η_{el} [%]	β_c [-]	$\dot{m}_{fuel}$ [g/s]	$\dot{m}_{out}$ [g/s]	T_{c_out} [°C]	$T_{rec\_cold\_out}$ [°C]	$T_{rec\_hot\_out}$ [°C]	TIT [°C]
NG	82.8	70000	24.95	4.44	7.62	727	172.7	601.6	209.8	941.1
H_2	88.9	70000	26.40	4.44	2.81	723	170.3	601.6	205.0	943.3
NH_3	94.1	70000	26.98	4.46	18.75	729	169.2	601.7	202.6	940.1

It is also critical to analyse the variation of the surge margin during steady-state operations when considering different compositions of H_2 and NH_3. As expected,

the surge margin for the H_2-NG blends remains almost unvaried (Figure 4-4, left) compared to the baseline with 100% natural gas operation, whereas for the case of NH_3-NG blends (Figure 4-4, right), the k_p reduces as the concentration of ammonia increases. The reduction of the surge margin is due to the increment of the ratio $\beta/\dot{m}$. There is both a reduction of the pressure ratio and of the mass flow but $\dot{m}$ reduces more than β. Despite the surge margin reduction for high ammonia contents, during steady-state operation the system is able to operate well above the minimum limit of 1.1 even at low electrical power outputs. However, during transient operations, in particular at lower electrical power outputs, it could still be possible to reach unstable conditions when operating with high ammonia content.

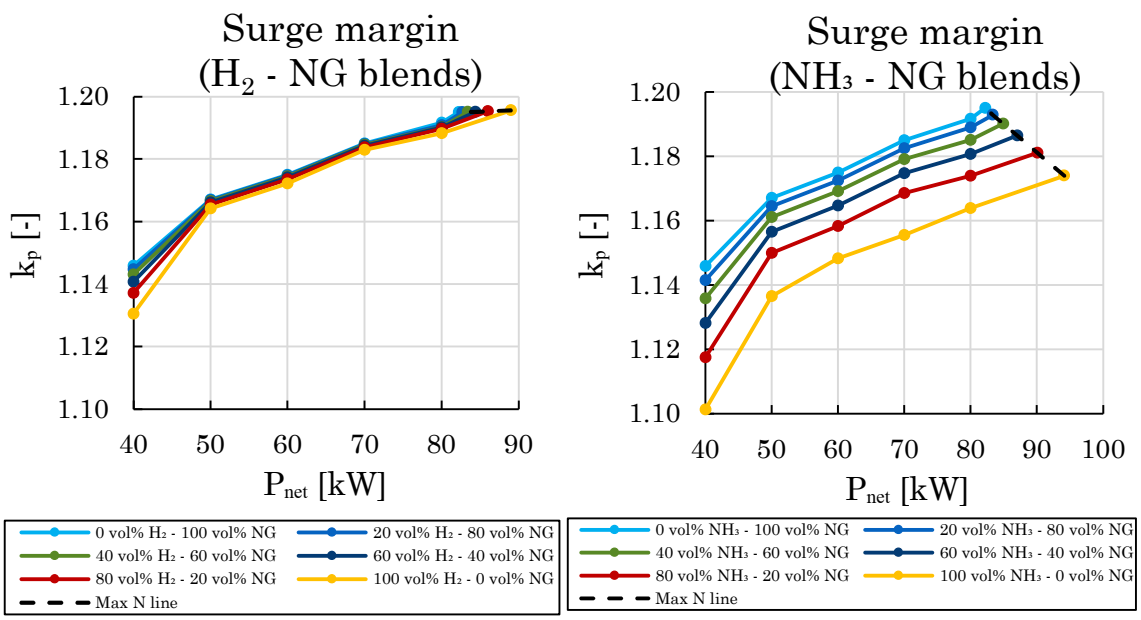

Figure 4-4: Off-design surge margin for different hydrogen and ammonia molar concentrations.

4.3 Dynamic analysis

This paragraph analyses the transient behaviour of the mGT with a focus on:

1) The power decrease steps keeping a constant fuel injection of ammonia, to analyse the effects on the surge margin and TOT for different NH_3-NG blends.

2) The injection of different mass flows of hydrogen and ammonia starting from an operation of 100% NG keeping a constant power output, to analyse the overtemperature that could be reached and the variations of the surge margin.

4.3.1 Power decrease steps

The analysis of the compressor stability during power decrease steps was performed only considering NH_3-NG blends since the mGT operating with H_2-NG blends results in similar values of the k_p compared to the 100% natural gas operation, as shown from the steady-state results. Since the steady state k_p is lower at lower loads (Figure 4-4), this condition is potentially the most critical during transient operations. Two cases of power variation have been considered, one at high loads with a step change from 80 kW to 70kW and the other at lower loads from 50 kW to 40 kW, to analyse the combined effect of different fuel compositions and power ranges on the surge margin. The simulations were performed injecting a constant mass flow of NH_3. This approach has been considered to investigate the mGT behaviour when there is a reduction in the requested load, while a constant mass flow rate of ammonia is injected. The injection is performed downstream of the natural gas fuel valve to keep the same original control system, because the regulation can be performed acting on the main valve. It should be noted that the relative percentage of NH_3 cannot be constant during a load variation if the injected mass flow of NH_3 is unchanged, because the natural gas content will be varied by the control system to satisfy the power fluctuations. For example, in case of a load reduction, the control system will reduce the amount of NG and consequently the percentage of ammonia will increase.

Initially, a step load reduction from 80 kW to 70 kW was considered. This was performed in the case of full natural gas operation and in the case of a constant injection of NH_3 mass flows of around 6.8 g/s and 11 g/s corresponding to a molar mass flow of ammonia of 60% and 80% respectively at 80 kW. It was not possible to inject more than 11 g/s because this would have exceeded the maximum

allowed mass flow to ensure a proper regulation of the main valve. The surge margin results are shown in Figure 4-5. The reduction of the k_p after t=0 s for the case of 100% NG is caused by the action of the control system. If the load is suddenly reduced, the control system reduces the rotational speed with a fast response while the pressure remains high before reaching the new stable condition. This is normally acceptable because the machine operates far from the surge line. When considering the use of NH_3-NG blends, the lower k_p during the load change is a result of the combined effect of the control system behaviour and the starting lower k_p at steady-state conditions. In this case, although the surge margin is reduced, this is still kept above 1.1. Figure 4-6 presents the TOT variations during the step variation showing that the control system is able to keep the constant value of the TOT without having temperature peaks during the transient phase.

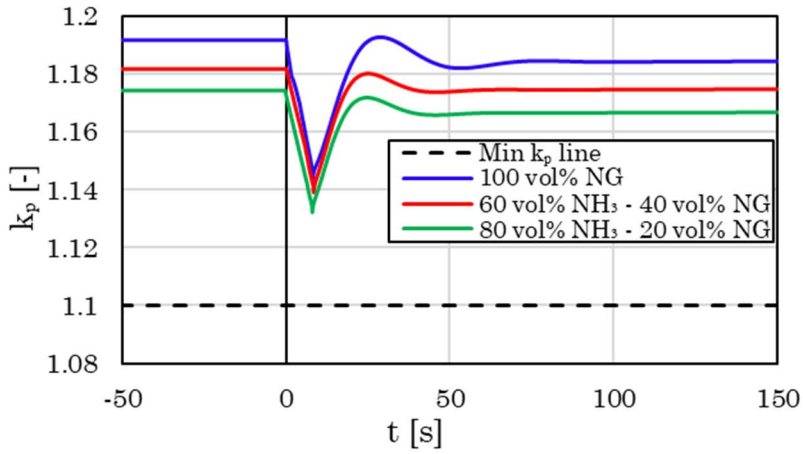

Figure 4-5: Surge margin for a power decrease step from 80 kW to 70 kW injecting different ammonia mass flows.

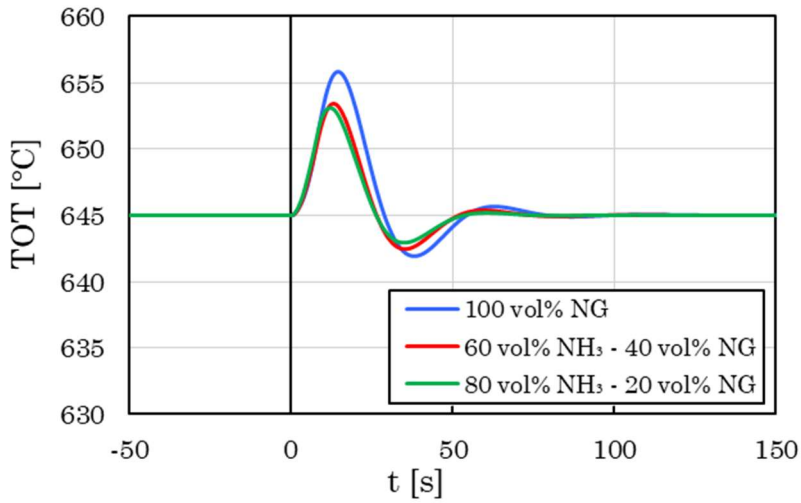

Figure 4-6: Turbine outlet temperature for a power decrease step from 80 kW to 70 kW injecting different ammonia mass flows.

After that, a step change from 50 kW to 40 kW was investigated, which represents a more critical condition due to starting lower surge margin at steady-state conditions.

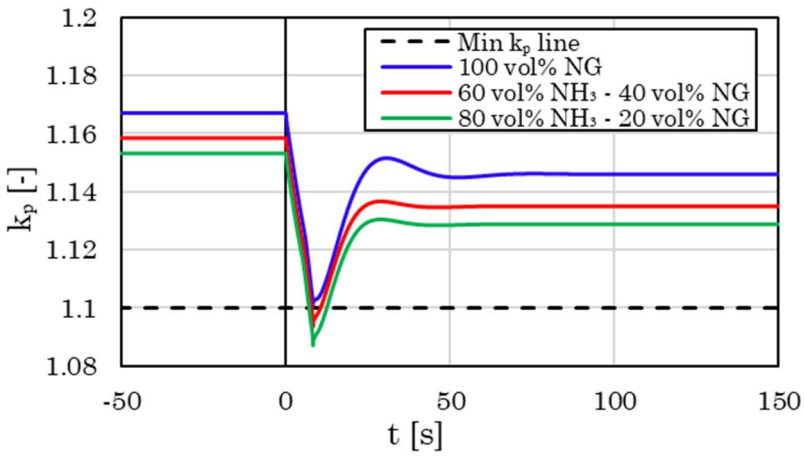

Figure 4-7: Surge margin for a power decrease step from 50 kW to 40 kW injecting different ammonia mass flows.

Figure 4-7 shows the surge margin variation comparing the case of 100% natural gas operation with the case of a constant injection of NH_3 mass flows around 4.9 g/s and 6.2 g/s corresponding to a molar mass flow of ammonia of

60% and 70% respectively at 50 kW. The system response has a similar behaviour compared to the 80 kW - 70 kW step condition. However, in this case, it is possible to reach low compressor surge margin for the power step investigated with the considered ammonia mass flows considering that the case with 100% natural gas was already more critical than the previous- These analysis show that especially at low power conditions slower rate of power reductions should be adopted when using blends with higher ammonia content.

4.3.2 Fuel injections

This analysis was mainly performed to evaluate the possibility of reaching high temperatures when injecting a quantity of ammonia or hydrogen in the main line. In this case the electrical power output was kept constant and equal to 80 kW. Higher power conditions are more critical conditions for overtemperature risks since higher fuel mass flows are injected.

For the dynamic analysis of the system, fuel injection steps were initially carried out considering H_2-NG blends, varying the composition from 100% of natural gas to blends with 10 vol%, 50 vol% and 80% of hydrogen. Due to the low density of H_2, this corresponds to mass concentrations of around 1.3 mass%, 10.6 mass% and 32.2 mass%, which requires the injection of around 0.094 g/s, 0.65 g/s and 1.48 g/s of hydrogen respectively. Figure 4-8 shows the transient behaviour of the TIT and TOT during the hydrogen injection. At t=0 s the H_2 mass flow is injected and after an initial temperature increase, the control system is able to reduce the NG flow rate of the main line, bringing the operating point to steady-state conditions and restoring the TOT value to 645 °C. The fuel step injections represent the theoretical most critical condition in terms of temperature peaks. In a real application, some time would be required for the flow rate to reach the requested value and for ensuring a stable combustion during the transition.

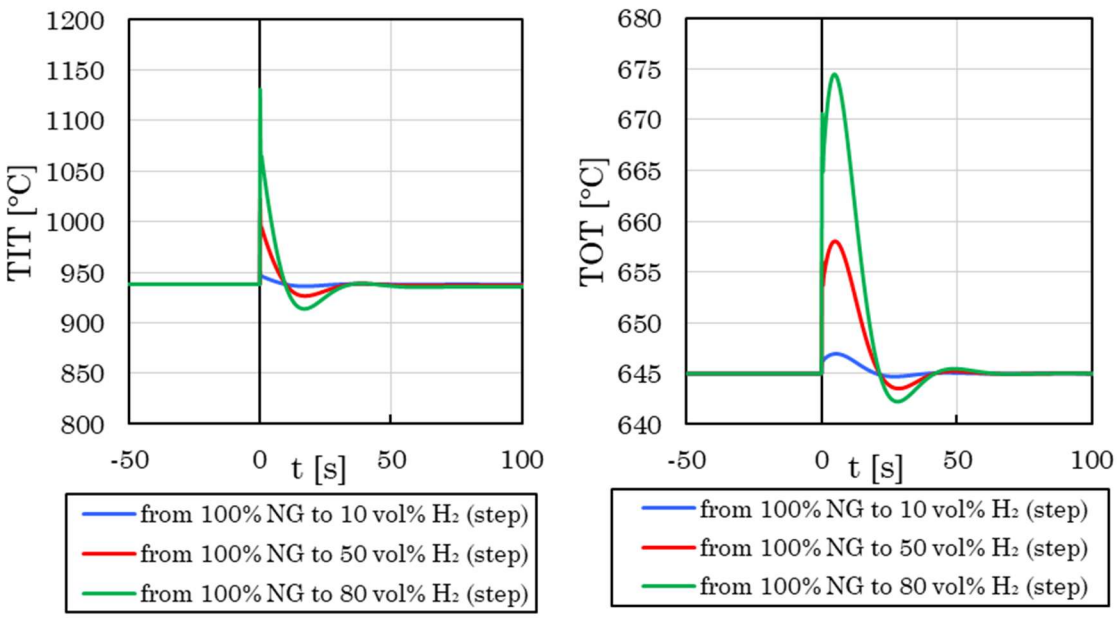

Figure 4-8: TIT (left) and TOT (right) variations due to hydrogen injection to reach 10%, 50% and 80% of H_2 molar concentration in a single step.

These results show that excessive peaks in the TIT and TOT can be reached with a step variation, and gradual injections are required. Only the case with 10 vol% is acceptable but this corresponds to a small amount of injected mass flow (0.094 g/s). For this reason, it was then proposed to gradually vary the composition linearly with a ramp of 50 s and 80 s for the 50 vol% and 80 vol% cases. By gradually injecting the hydrogen mass flow it was possible to significantly reduce the TIT, as shown in Figure 4-9.

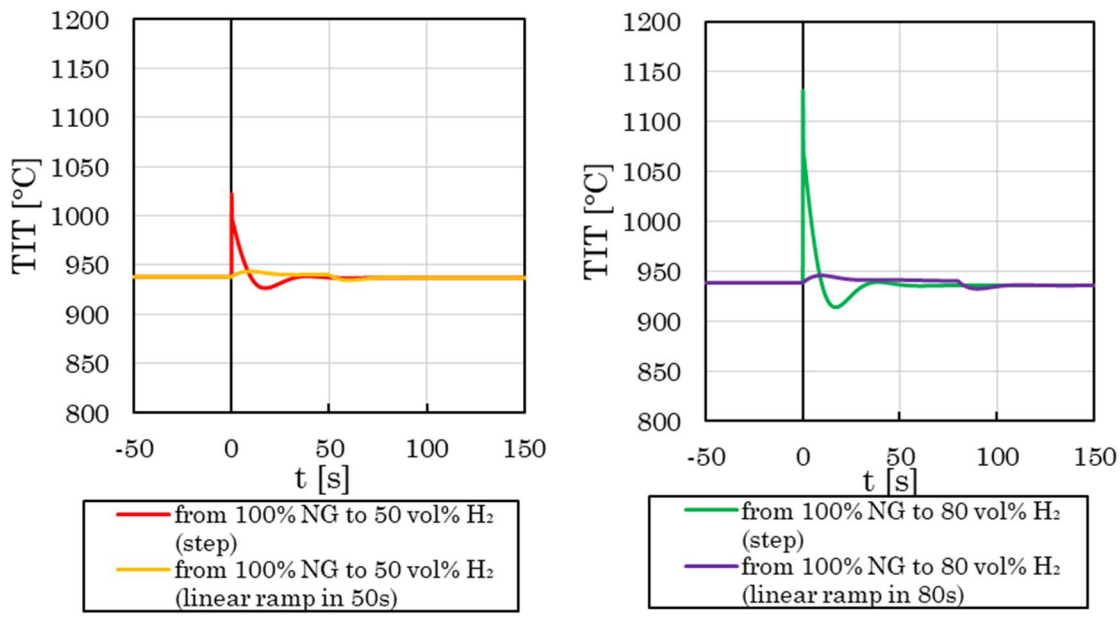

Figure 4-9: TIT variation due to hydrogen injection to reach with a step and linear ramp 50% (left) and 80% (right) of H_2 molar concentration.

This is also reflected on the TOT behaviour displayed in Figure 4-10. It can be seen that with these linear ramps even by increasing the percentage of H_2 excessive temperature peaks do not occur.

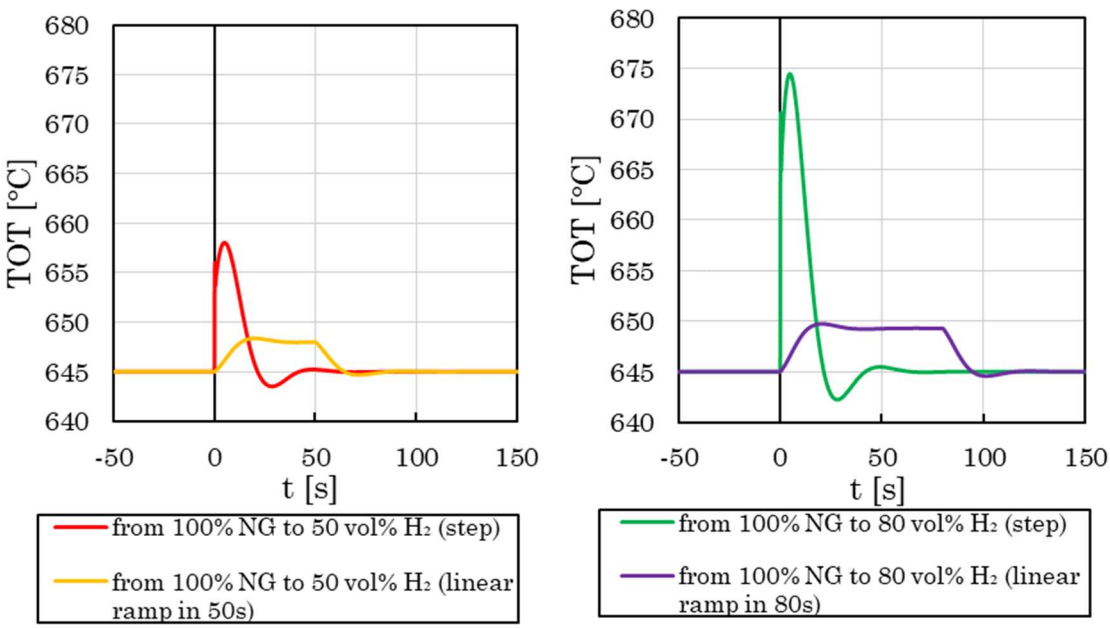

Figure 4-10: TOT variation due to hydrogen injection to reach with a step and linear ramp 50% (left) and 80% (right) of H_2 molar concentration.

Finally, the effects on the surge margin were considered and they can be observed in Figure 4-10, as these can be of potential threat during the injection of an additional amount of fuel mass flow. Considering the starting high value of the surge margin at steady-state conditions for P_{net}= 80 kW, the limit of 1.1 is always respected despite its initial reduction. Moreover, a more gradual injection can reduce the k_p oscillations which is be beneficial at low power outputs.

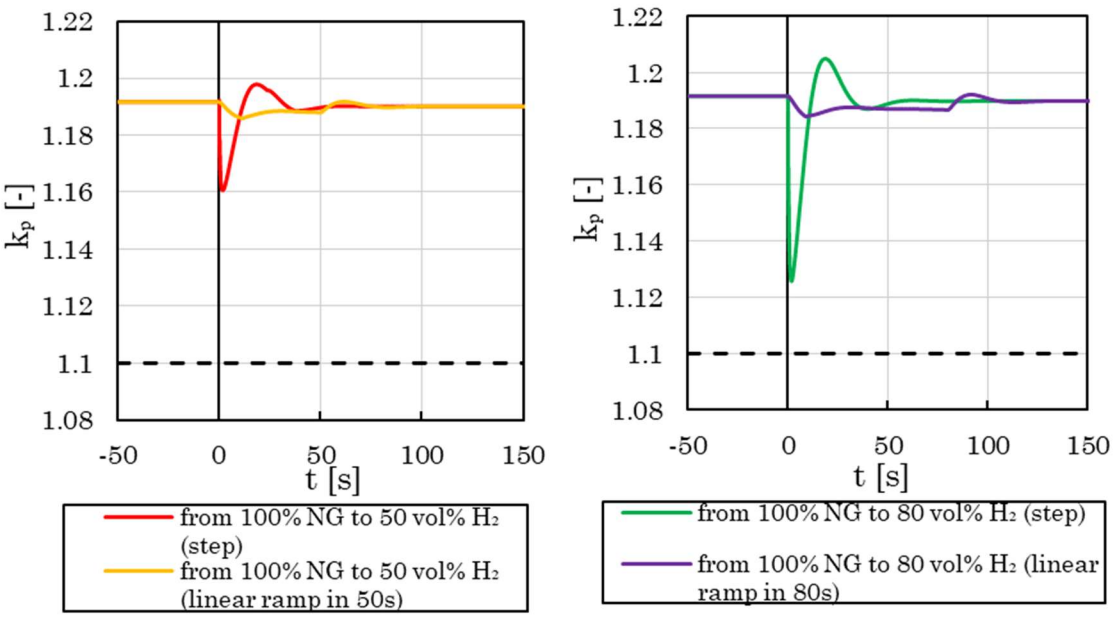

Figure 4-11: Surge margin variation due to hydrogen injection to reach with a step and linear ramp 50% (left) and 80% (right) of H_2 molar concentration.

Fuel injection steps were also carried out considering NH_3-NG blends, varying in the same way the composition from 100% of natural gas to blends with 10 vol%, 50 vol% and 80% of ammonia. In the case of ammonia injection, similar results of temperature oscillations were obtained. For briefness, only the TOT results are presented in Figure 4-12. The reason for the initial temperature increase, despite the lower LHV compared to NG, is that an additional quantity of fuel is injected, and the control system requires some time in order to regulate the natural gas mass flow of the main valve to restore the TOT to the set point value. The NG fraction is not replaced with the same mass of NH_3. The NH_3 mass flow is injected and the main valve controlling the NG fuel flow is

regulated to keep a constant TOT. Similar high temperature values are reached with a step injection compared to the injection of hydrogen as the comparison is performed in molar fraction. However, it should be considered that the ammonia concentration in mass is higher: a composition of 10 vol% requires an injection of 0.78 g/s, while a composition of 50 vol% and 80 vol% requires 5.2 g/s and 11 g/s of ammonia. Even in this case, a more gradual variation of the composition allows for a reduction of the temperature oscillations. This means that a higher amount of fuel flow of ammonia can be injected in a shorter amount of time without causing excessive peaks of temperature.

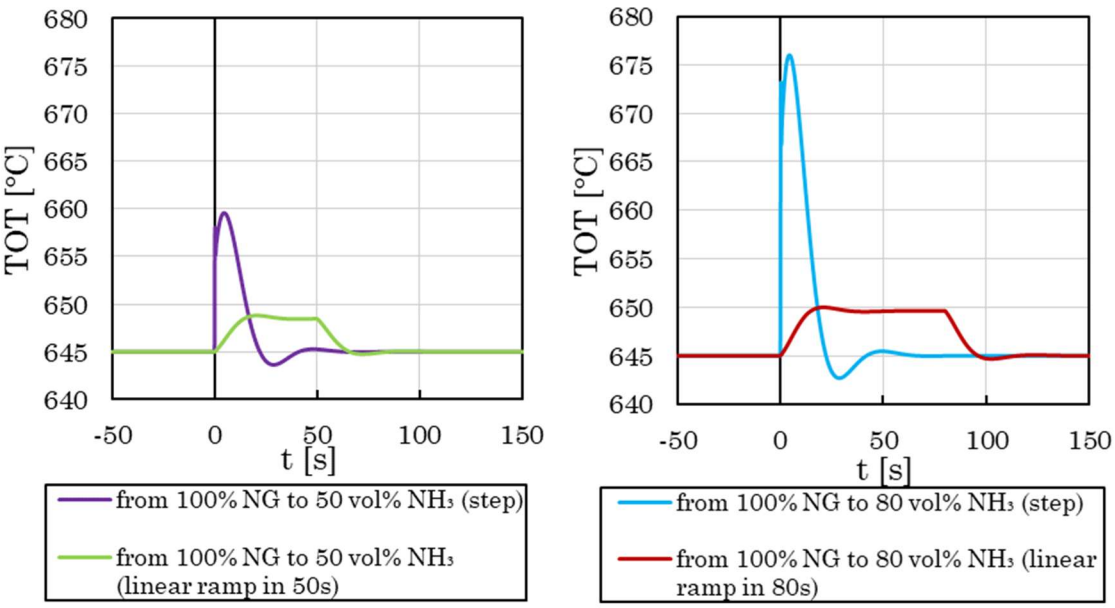

Figure 4-12: TOT variation due to ammonia injection to reach with a step and linear ramp 50% (left) and 80% (right) of NH_3 molar concentration.

The surge margin dynamic behaviour is presented in Figure 4-13 also for the ammonia case considering the step and the linear gradual injections to reduce the oscillations. The limit of 1.1 is always respected even with a step injection despite the initial dip, slightly lower compared to the injection of hydrogen. Both cases (with 50 vol% NH_3 and 80 vol% NH_3) terminate with a lower k_p, as already presented in the steady-state analysis.

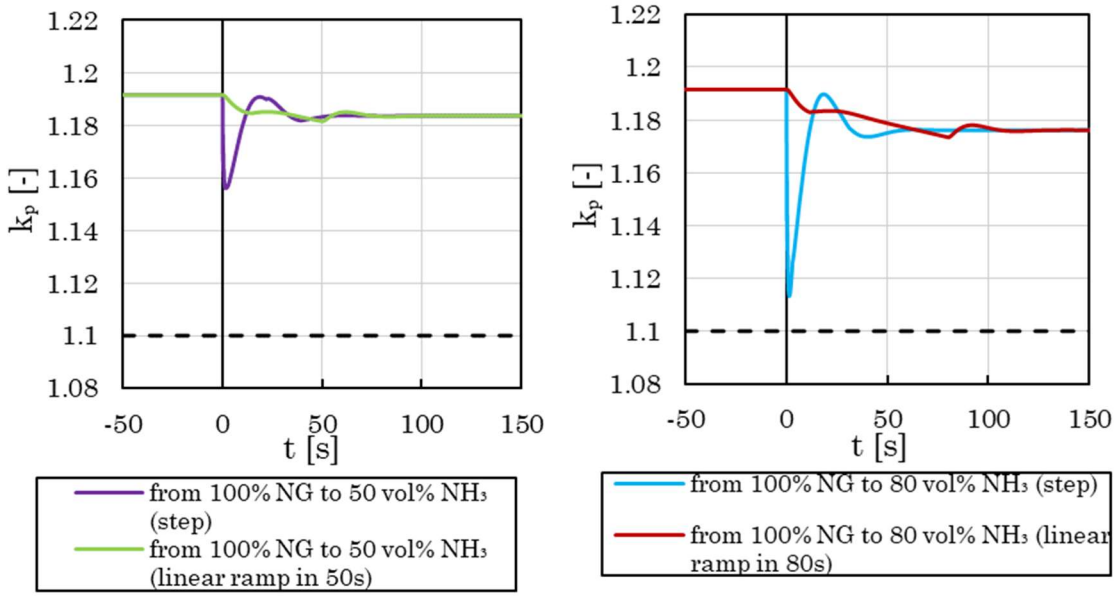

Figure 4-13: Surge margin variation due to ammonia injection to reach with a step and linear ramp 50% (left) and 80% (right) of NH_3 molar concentration.

4.4 Conclusions

This chapter investigates the impact of fuel composition changes on the performance and dynamic behaviour of the T100 micro gas turbine. While the current research studies are predominantly focused on improving combustion stability and performance with alternative fuels, this study focuses on understanding the system-level effects of varying blends of H_2-NG and NH_3-NG on steady-state and transient performance. These aspects are important for retrofitting mGTs for flexible operation with diverse fuel blends. An investigation into the mGT behaviour under dynamic conditions is essential for both compressor safety and turbine outlet temperature control during composition changes. The study adopts a modified T100 layout where hydrogen or ammonia can be injected into the main fuel line of the burner while the pilot line is still supplied with natural gas.

Steady-state results for various fuel compositions reveal variations in fuel mass flow and rotational speed. The reduction in rotational speed contributes to increased power output, with both hydrogen and ammonia blends. In particular,

with 100% of H_2 it is possible to increase the power output of +4.9 kW and with 100% of NH_3 a maximum of + 2.35 kW compared to the baseline with at 100% NG operation. The steady-state results showed a reduction on the surge margin only for the NH_3-NG blends due to the increased fuel mass flow required for a given power output.

Transient power decrease steps were investigated for studying the limits of the ammonia content to inject in the blend to ensure stable operation. It was demonstrated that during operation at high power settings, with a power step from 80 kW to 70 kW, the surge margin always kept above the minimum acceptable value of 1.1. However, for operation at lower power settings, it was possible to reach critical dangerous conditions. For example, in the considered step from 50 kW to 40 kW, the presence of ammonia reduced the k_p below 1.1. These analyses show that especially at low power conditions slower rate should be considered.

Finally, transient simulations were performed for the analysis of possible over-temperatures that can be caused by sudden injections of H_2 or NH_3 in the main fuel line. Step variations of the composition by adding 10 vol%, 50 vol% and 80 vol% of hydrogen and ammonia to the natural gas were performed at constant power output where excessive temperature peaks were determined. Nevertheless, the dynamic model developed with the TRANSEO tool was successfully used to define ramps for the variation of fuel with different percentages in the fuel mixture to ensure that high peaks of temperature are not reached. Gradual linear injections proved to be beneficial, reducing temperature oscillations and increasing the surge margin during transient.

5 Energy management of the T100 integrated with energy storage systems

This chapter focuses on developing an energy scheduler for different plant layouts based on the integration of the previously analysed T100 with different energy storage systems. The following configurations are considered and compared:

- Baseline plant: T100 and a latent heat TES;
- Baseline plant integrated with a battery;
- Baseline plant integrated with a small-size CAES system;
- Baseline plant integrated with a power-to-H_2 system.

The optimisation performed in this study uses a discretisation time of 1 hour, and it employs the off-design curves obtained from the steady-state results of the VUB mGT (in standard conditions, with air injection and hydrogen injection).

5.1 Common scenario for the optimisation

To identify a common scenario to for the energy management optimisation, the following data are required:

- Electrical and thermal demands: $\boldsymbol{P}_{el-DEMAND}(\boldsymbol{T})$, $\boldsymbol{P}_{th-DEMAN}$ $(\boldsymbol{T})$;
- Ambient temperature: $\boldsymbol{T}_{amb}(\boldsymbol{T})$;
- Electricity costs to buy from the grid or sell to the grid: $\mathbf{C}_{\mathrm{el-GRID-bu}}$ $(\mathbf{T})$ and $\mathbf{C}_{\mathrm{el-GRID-sell}}(\mathbf{T})$;
- Natural gas cost $\mathrm{C_{NG}}$.

Where $\boldsymbol{T} = [t_1, t_2, \dots, t_{i-1}, t_i, t_{i+1}, \dots, t_{N-1}, t_N]$ is a vector representing the time, and the parameters in bold represent vector with N elements for each hour of the day. For this study, the considered time interval ΔT is 1 hour and therefore N=24. The load profiles and ambient conditions are taken from typical days

referred to past operations of the "Smart Polygeneration Microgrid" (SPM) of the UNIGE University Campus (Savona, Italy). The electrical demands have been scaled down due to the smaller size of the considered plant layout compared to the SPM. It is assumed that on the electrical side, each plant is connected to grid, and on the thermal side, the plant is connected to a district heating network (DHN), where water feeds the system at around 75 °C and returns at around 50 °C as in the SPM.

The electricity for buying from the grid and fuel costs are taken from the Gestore Mercati Energetici (GME) website [134], the authority operating the Italian electrical energy and natural gas markets. The electricity cost is variable while the natural gas cost is constant during a single day. Typically, the selling price from microgrids is less than the buying price and it depends on the specific contract of the microgrid. To perform a parametric study on the selling price, the electricity costs for selling to the grid are obtained by multiplying the buying price with a constant selling-to-buying ratio, $\mathrm{ratio}_{\mathbf{sell-buy}}$ (Eq.(5-1)):

$$\mathbf{C}_{\mathrm{el-GRID-sell}}(\mathbf{T}) = \mathrm{ratio}_{\mathrm{sell-buy}} * \mathbf{C}_{\mathrm{el-GRID-buy}}(\mathbf{T}) \tag{5-1}$$

For this analysis the two extreme values are considered:

1. $\mathrm{ratio}_{\mathrm{sell-buy}} = 1$, where $\mathbf{C}_{\mathbf{el-GRID-sell}}(\mathbf{T}) = \mathbf{C}_{\mathbf{el-GRID-buy}}(\mathbf{T})$
2. $\mathrm{ratio}_{\mathrm{sell-buy}} = 0$, where $\mathbf{C}_{\mathbf{el-GRID-sell}}(\mathbf{T}) = \mathbf{0}$

In the former case, the plant can profit by selling to the grid with the same price of the buying costs; in the latter case, an exchange to the grid is still possible in case of overproduction but without an economical benefit. A representative day of April 2022 was selected, where the variable demands, ambient temperature and electricity prices are shown in Figure 5-1 and the considered natural gas cost is 0.1031 €/kWh [134].

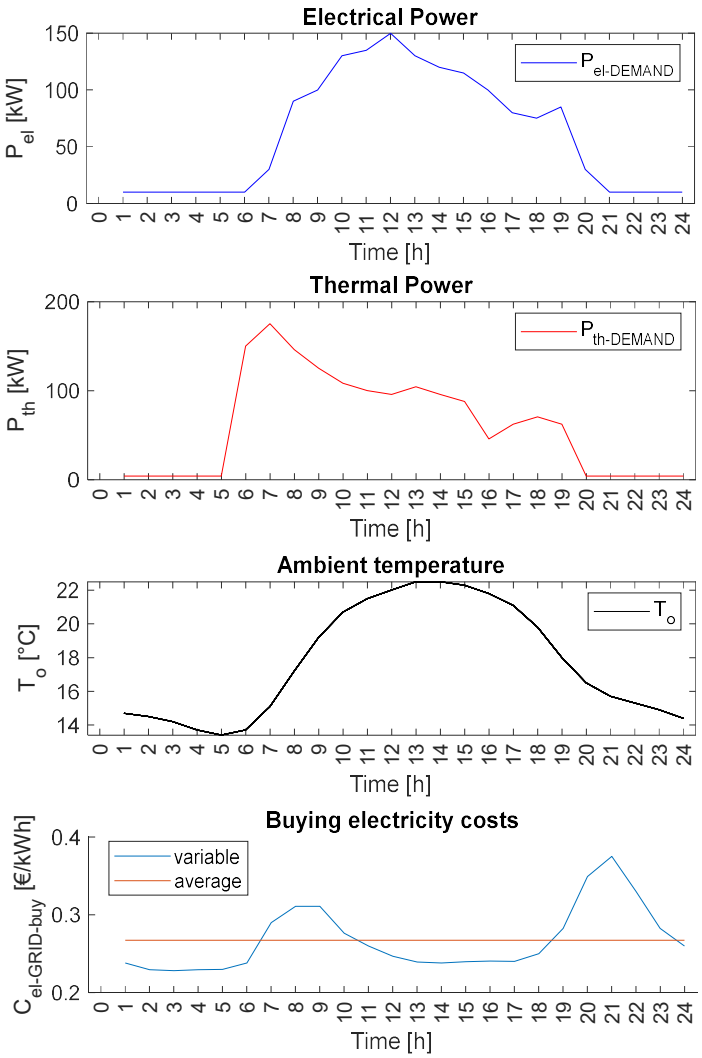

Figure 5-1. Variable demands, ambient temperature and electricity prices of a representative day of April 2022 with the averaged value [134]**.**

5.2 Components performance modelling, operational limits and operational costs

To calculate the overall daily plant cost, the optimiser requires for each component:

- functions to calculate the relevant performance characteristics, such as fuel flow required and thermal power produced from the mGT or the state of charge (SOC) of the various ESSs;

- operational limits, such as the minimum and maximum operating range of each component;
- operational costs (OPEX).

This paragraph describes how these functions and data have been obtained for each component. The different layouts are shown in Figure 5-2, Figure 5-4, Figure 5-6 and Figure 5-9.

5.2.1 T100 micro gas turbine

The micro gas turbine performance is calculated with off-design curves obtained from the steady-state results of the TRANSEO model. Three separate functions have been developed depending on the specific use of the mGT: the first function is used to represent the normal operation of the T100 (without compressed air or hydrogen injection), the second function to model the effect of air injection from the CAES and the third one for the use with natural gas and hydrogen blends.

The first function calculates the thermal power output $\boldsymbol{P}_{th-mG}$ and the natural gas mass flow $\dot{\boldsymbol{m}}_{NG-mGT}$ of the mGT from the ambient temperature $\boldsymbol{T}_{amb}$ and the electrical power output $\boldsymbol{P}_{el-mGT}$. Therefore, the mGT performance function has this general structure (Eq. (5-2)):

$$[\boldsymbol{P}_{th-mGT}, \dot{\boldsymbol{m}}_{NG-mGT}] = f_{mGT-STD}(\boldsymbol{T}_{amb}, \boldsymbol{P}_{el-mGT}) \tag{5-2}$$

The second function is used to calculate the T100 performance during air injection. In this case, $\boldsymbol{P}_{th-mG}$ and $\dot{\boldsymbol{m}}_{NG-mGT}$ are also a function of the injected air mass flow $\dot{\boldsymbol{m}}_{air-inj-mG}$ (Eq. (5-3)):

$$[\boldsymbol{P}_{th-mGT}, \dot{\boldsymbol{m}}_{NG-mGT}] = f_{mGT-CAES}(\boldsymbol{T}_{amb}, \boldsymbol{P}_{el-mGT}, \dot{\boldsymbol{m}}_{air-inj-mGT}) \tag{5-3}$$

Instead, the last function requires the information on the H_2 mass flow $\dot{\boldsymbol{m}}_{H_2-mGT}$ (Eq. (5-4)):

$$[\boldsymbol{P}_{th-mGT}, \dot{\boldsymbol{m}}_{NG-mGT}] = f_{mGT-H_2}(\boldsymbol{T}_{amb}, \boldsymbol{P}_{el-mGT}, \dot{\boldsymbol{m}}_{H_2-mGT}) \tag{5-4}$$

Additional functions are required to calculate several constraints, depending on the considered case. For the mGT used in the traditional mode, only the minimum and maximum power outputs are required $\boldsymbol{P}_{el-mGT-min}$ and $\boldsymbol{P}_{el-mGT-max}$. The minimum power output is set constant to $P_{el-mGT-min}$ = 40 kW in all the cases, so that the T100 can operate in stable conditions even at high ambient temperatures, and to avoid high production of CO emissions, typical of low loads. The maximum power output of the standard mGT depends on the ambient temperature and is also obtained from the TRANSEO off-design results. The function has this general structure (Eq. (5-5)):

$$\boldsymbol{P}_{el-mGT-max} = f_{mGT-max-STD}(\boldsymbol{T}_{amb}) \tag{5-5}$$

For the CAES case, two additional functions are required to calculate the minimum and maximum compressed air mass flow rates ($\dot{\boldsymbol{m}}_{air-mGT-min}$ and $\dot{\boldsymbol{m}}_{air-mGT-max}$) that can be injected as a function of $\boldsymbol{T}_{amb}$ and $\boldsymbol{P}_{el-mGT}$ (Eqs. (5-6), (5-7)):

$$\dot{\boldsymbol{m}}_{air-mGT-min} = f_{mGT-air-max}(\boldsymbol{T}_{amb}, \boldsymbol{P}_{el-mGT}) \tag{5-6}$$

$$\dot{\boldsymbol{m}}_{air-mGT-max} = f_{mGT-air-max}(\boldsymbol{T}_{amb}, \boldsymbol{P}_{el-mGT}) \tag{5-7}$$

Not only the maximum limit function for $\dot{\boldsymbol{m}}_{air-mGT}$ is required due to the compressor surge limitations, but also the minimum limit function is required if the air injection is used to increase the power output compared to the standard operation.

Similarly, for the power-to-H_2 case, two functions are required to calculate the minimum and maximum hydrogen flow rates ($\dot{\boldsymbol{m}}_{H_2-mGT-min}$ and $\dot{\boldsymbol{m}}_{H_2-mGT-max}$) (Eqs. (5-8),(5-9)):

$$\dot{\boldsymbol{m}}_{H_2-mGT-min} = f_{mGT-H_2-max}(\boldsymbol{T}_{amb}, \boldsymbol{P}_{el-mGT}) \tag{5-8}$$

$$\dot{\boldsymbol{m}}_{H_2-mGT-max} = f_{mGT-H_2-max}(\boldsymbol{T}_{amb}, \boldsymbol{P}_{el-mGT}) \tag{5-9}$$

Finally, the costs related to the mGT operations are not only linked to the fuel mass flow rate utilised but also to the variable operation and maintenance costs $OPEX_{Var-m}$ = 0.015 €/kWh, whose value is obtained from ref. [135].

5.2.2 Thermal energy storage

The chosen TES is a latent heat water thermal energy storage system, due to its simplicity and low capital cost. The dimensions and characteristics are the same of the TES used in the IES (Innovative Energy System) laboratory of the Savona Campus with 5 m^3 of capacity for the heat storage, resulting in around 150 kWh of maximum thermal capacity (with a thermal swift of around 25 °C). This TES allows for up to around 150 kW for charge and discharge. The TES is used to store and release thermal energy based on the requested thermal power $\boldsymbol{P}_{th-TES-req}$. According to the considered convention, the TES thermal power is considered positive during the discharge and negative during the charge.

The main formula used to calculate each component of thermal capacity vector $\boldsymbol{E}_{th-TE}$ is (Eq.(5-10)):

$$E_{th-TES}(t_i) = E_{th-TES}(t_{i-1}) - P_{th-TES-req}(t_i) * \Delta T \qquad (5\text{-}10)$$

using the initial state of charge SOC_{TES-t} , the minimum and maximum thermal capacity $\mathrm{E_{th-TES-min}}$ and $\mathrm{E_{th-TES-ma}}$, the requested power $P_{th-TES-re}$ (t_i) and the time interval ΔT. The requested power $\boldsymbol{P}_{th-TES-req}$ vector is an input generated by the optimiser ranging within its acceptable operating limits (in this case, between -150 kW and +150 kW). However, the real power output $P_{th-TES}(t_i)$ is also dependent on the storage capacity at the previous time step $E_{th-TES}(t_{i-1})$. For example, the optimiser could request +150 kW when the TES is fully or partially discharged, and it would not be able to satisfy the requested demand. This additional constraint is imposed in the model to avoid the use of non-linear constraints, according to this approach: if the requested power exceeds the capability of the storage (if E_{th-T} $(t_i) < \mathrm{E_{th-TES-min}}$ or E_{th-TE} $(t_i) > \mathrm{E_{th-TES-max}}$), the thermal capacity is set to its minimum or maximum value (E_{th-TE} $(t_i) = \mathrm{E_{th-TES-min}}$ or $E_{th-TES}(t_i) = \mathrm{E_{th-TES-max}}$). The real power output $P_{th-TES}(t_i)$ is then calculated by rearranging equation (5-10) with the updated E_{th-TE} (t_i) values.

Therefore, the TES performance function has this general structure (Eq.(5-11)):

$$[\boldsymbol{E}_{th-TES}, \boldsymbol{P}_{th-TES}] = f_{TES}(SOC_{TES-t0}, \mathrm{E}_{\mathrm{th-TES-min}}, \mathrm{E}_{\mathrm{th-TES-max}}, \boldsymbol{P}_{th-TES-req}, \Delta T) \quad (5\text{-}11)$$

The variable OPEX for the TES are negligible due to non-moving parts [136] while the fixed maintenance cost is constant and therefore is not considered for the optimisation.

5.2.3 Battery

The battery performance is modelled with the same approach of the TES. The storage capacity $E_{el-BES-ma}$ is assumed equal to 50 kWh and the maximum C-rate is set equal to 1, reflected in a maximum charging and discharging power of $P_{el-BES-max}$ = 50 kW. The other limit regards the minimum capacity $E_{el-BES-mi}$ that must be kept at least 20% of the maximum capacity, to avoid a depth of discharge (DoD) above 80%, which negatively impacts batteries life. The battery efficiency η_{BES} is assumed equal for both charging and discharging and set to 90%, resulting in a round trip efficiency (RTE) of 81%. These are general values for stationary batteries as reported in [137], typical for example of Li-ion batteries.

The main formulas used to calculate each component of the storage capacity $\boldsymbol{E}_{el-}$ over each time step are (Eqs.(5-12),(5-13)):

$$E_{el-BES}(t_i) = E_{el-BES}(t_{i-1}) - \eta_{BES} * P_{el-BES-req}(t_i) * \Delta T \text{ (charging)} \quad (5\text{-}12)$$

$$E_{el-BES}(t_i) = E_{el-BES}(t_{i-1}) - P_{el-BES-req}(t_i) * \Delta T / \eta_{BES} \ (discharging) \quad (5\text{-}13)$$

In this case the function structure is the following (Eq.(5-14)):

$$[\boldsymbol{E}_{el-BES}, \boldsymbol{P}_{el-BES}] = f_{BES}(SOC_{BES-t0}, \eta_{BES}, E_{el-BES-min}, E_{el-BES-max}, \boldsymbol{P}_{el-BES-req}, \Delta T) \quad (5\text{-}14)$$

Similarly to the thermal energy storage approach, if the requested power exceeds the capability of the storage, the battery capacity is set either to its minimum or maximum value and the real power output $\boldsymbol{P}_{el-BES}$ is calculated rearranging equations (5-12) or (5-13).

5.2.4 Air compressor

A two-stage reciprocating compressor is considered with a polytropic efficiency $\eta_{pol-COMP}$ of 85 % for each stage and with an overall pressure ratio $\beta = 50$ as in the preliminary analysis of Chapter 3. The power output $P_{COMPR-stage}$ to compress a specific air mass flow $\dot{m}_{COMPR-air}$ is calculated as below (Eq.(5-15)):

$$P_{el-COMPR-stage} = \dot{m}_{COMPR-air} c_p T_{in} \left(\beta_{stage}^{\frac{k-1}{k*\eta_{pol}}} - 1 \right) \tag{5-15}$$

The overall maximum compressor power is set to 50 kW.

5.2.1 Electrolyser

A PEM electrolyser is considered for the hydrogen production, considering a constant efficiency η_{PEMEC} = 50 kWh/kgH_2 (around 67%) [51]. The required electrolyser power $P_{el-PEMEC}(t_i)$ to produce a desired amount of hydrogen mass flow $\dot{m}_{H_2-PEM}$ (t_i) is calculated with this formula (Eq.(5-16)):

$$P_{el-PEMEC}(t_i) = \left(\frac{1}{\Delta T}\right) * \frac{\dot{m}_{H_2-PEMEC}(t_i)}{\eta_{PEMEC}} \tag{5-16}$$

The overall maximum electrolyser power is set to 50 kW.

5.3 Baseline plant: T100 with TES connected to the grid

The minigrid layout is shown in Figure 5-2. The main components are the T100 micro gas turbine, used to produce both electrical and thermal power, and the TES which is used to decouple the mGT electrical and thermal production. The TES is also used to satisfy the thermal demand during peak hours, where the demand exceeds the T100 maximum power output (around 6.00 to 8.00 am, see Figure 5-1), allowing for a downsizing of the plant. The plant is electrically connected to the grid and can share electricity in both directions and to a DHN, where water feeds the system at around 75°C and returns at around 50°C.

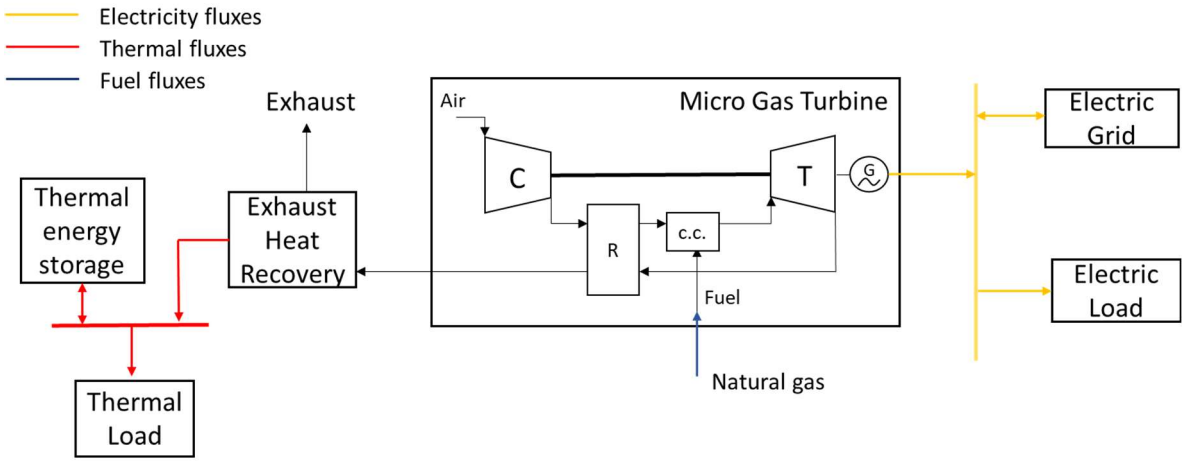

Figure 5-2. Baseline plant layout

The final equations that need to be introduced are the energy balances and the cost function. The energy balances represent the problem constraints and are reported below (Eqs.(5-17),(5-18)):

$$\boldsymbol{P}_{el-DEMAND} - \boldsymbol{P}_{el-GRID} - \boldsymbol{P}_{el-mGT} = \mathbf{0} \tag{5-17}$$

$$\boldsymbol{P}_{th-DEMAND} - \boldsymbol{P}_{th-mGT} - \boldsymbol{P}_{th-TES} \leq \mathbf{0} \tag{5-18}$$

The electrical side is represented by an equality constraint while the thermal side by an inequality constraint, meaning that the thermal power produced by the plant needs to be at least equal to the demand. In the real operation of the T100, if the $\boldsymbol{P}_{th-mGT}$ produced by the mGT is more than the demand, and the TES cannot store the excess of energy, a bypass-valve at the exhausts opens to release the unused energy. This is imposed because the objective function of the optimisation problem is the reduction of the operative costs and not the reduction of thermal losses. Therefore, this is not an heat-driven operation as the optimiser is allowed to dissipate some of the heat if this leads to a reduction of the overall plant costs.

The total cost for operating the plant is calculated as below (Eq.(5-19)):

$$\mathrm{COST_{TOT}} = \frac{\Delta T}{3600}\sum_{i=1}^{N}\Big(C_{el}(t_i)\,P_{el-GRID}(t_i) + \dot{m}_{NG-mGT}(t_i)\,C_{NG}\,LHV_{NG} + OPEX_{Var-mGT}\,P_{el-mGT}(t_i)\Big) + C_{th} \tag{5-19}$$

Where $C_{el} = \begin{cases} C_{el-GRID-buy}(t_i) & if\ (P_{el-GR}\ \ (t_i) \geq 0) \\ C_{el-GRID-sell}(t_i) & if(P_{el-GRID}(t_i) < 0) \end{cases}$, and C_{th} is a penalty cost introduced to impose the thermal power inequality constraint.

The only decision variables for this problem are is $\boldsymbol{P}_{el-mG}$, while $\boldsymbol{P}_{el-GR}$ and $\boldsymbol{P}_{th-mG}$ and $\dot{\boldsymbol{m}}_{NG-mGT}$ can be calculated from the two energy balances and mGT function. In combination with the energy balance constraints, the upper and lower constraints of each component are also be respected. It was also imposed only one startup for the mGT per day since repetitive shutdowns and startup can negatively affect the life duration and maintenance costs.

The optimiser used in this study is the particle-swarm algorithm, a widely used metaheuristic optimisation scheme used for different energy scheduling problems [138]. This algorithm generates a random initial guess and iteratively modifies $\boldsymbol{P}_{el-mGT}$. At each iteration, $\boldsymbol{P}_{el-GRID}$ is calculated from the energy balance (Eq. (5-7) rearranged) and $\boldsymbol{P}_{th-mGT}$, $\dot{\boldsymbol{m}}_{NG-mGT}$ from the mGT function (Eq. (5-5)). The requested TES thermal power is obtained from the thermal energy balance ($\mathbf{P}_{\mathrm{th-TES-req}} = \boldsymbol{P}_{th-DEMAND} - \boldsymbol{P}_{th-mG}$) and $\boldsymbol{P}_{th-TES}$ is calculated from the TES function (Eq.(5-11)). If $P_{th-DEMAND} - P_{th-mG} - P_{th-TES-out} > 0$ (this happens when $P_{\mathrm{th-TES-req}}(t_i) < P_{\mathrm{th-TES}-ou}\ (t_i)$) the thermal constraint is imposed by adding a penalty cost C_{th} to $\mathrm{COST_{TOT}}$. In this way the optimiser selects the decision variable to also eliminate the penalty cost C_{th} together with reducing the other operative costs, therefore ensuring that $P_{th-DEMAND} - P_{th-mGT} - P_{th-TES} \leq 0$. The obtained values of $\boldsymbol{P}_{el}$, $\boldsymbol{P}_{el-mGT}$ and $\boldsymbol{m}_{NG-mGT}$ are used to calculate the total cost (equation (5-19)). The optimiser will return the optimal values $\boldsymbol{P}_{el-mGT}$, from which the optimal final values $\boldsymbol{P}_{el-GR}$, $\boldsymbol{P}_{th-mGT}$ and $\dot{\boldsymbol{m}}_{NG-m}$, can be calculated with the same equations.

Figure 5-3 displays the electrical and thermal power scheduling of the considered plant with a $ratio_{sell\text{-}buy}$ equal to 0 (Figure 5-3, left) and 1 (Figure 5-3, right), respectively. Both scenarios start with SOC_{TES} equal to 0.

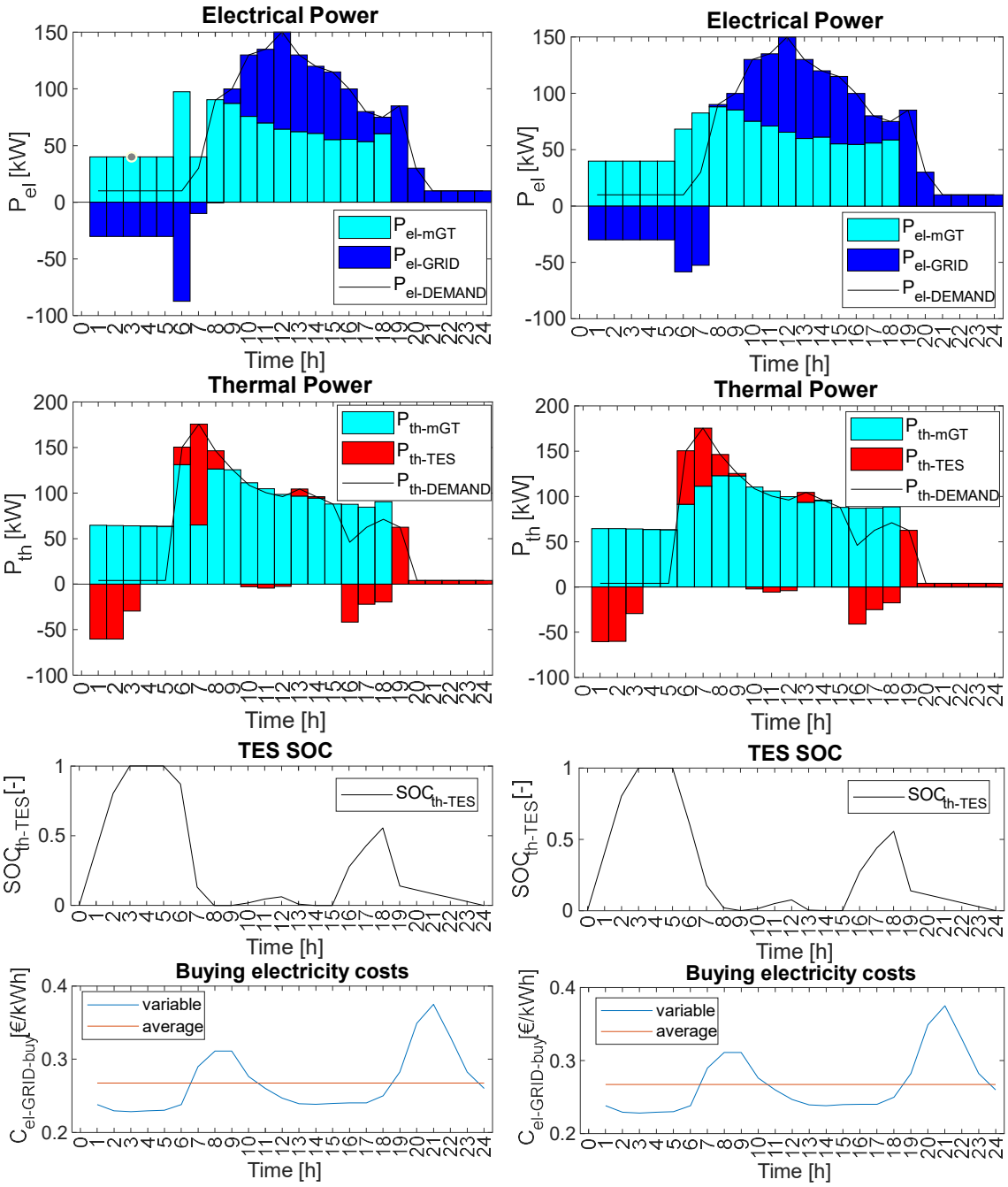

Figure 5-3. Electrical and thermal power scheduling of the baseline plant.

In Figure 5-3 left, the mGT turns on from t = 1 to 5 hours to satisfy the low thermal demand, therefore remaining at the minimum load due to the low

electrical demand. The unused electricity is injected into the grid without revenue and the TES is charged with the excess of produced thermal power. At t= 6 hours, the mGT operates at higher load to satisfy a higher thermal demand and keep the TES almost charged to be used at t=7 and 8 hours. During the central hours of the day, the electricity price is low, and the mGT runs at a high load only to satisfy the thermal power and charge the TES for later use. During the last hours of the day, from t=19 to 24 hours, electrical demand is satisfied by the grid and the thermal demand only by the TES. In Figure 5-3 right, the behaviour of the mGT and TES is similar but with a higher revenue as it is possible to sell to the grid (in this case in the initial part of the day) : the total cost in the case of $ratio_{sell/buy}$=0 is C_{tot}=656.2 €/day and in the case of $ratio_{sell/buy}$=1 is C_{tot}=593.8 €/day.

5.4 Baseline plant with BES

The layout is shown in Figure 5-4 and it consists of the baseline plant with the addition of the battery.

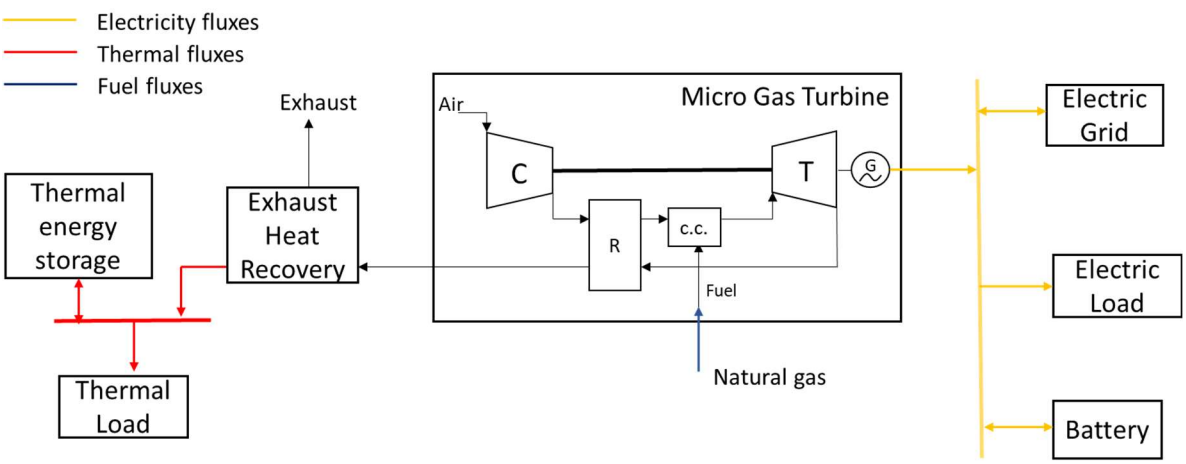

Figure 5-4. Plant layout with battery

The energy balance on the electrical side takes into account of the battery power $\boldsymbol{P}_{el-B}$ while on the thermal side the approach is unvaried (Eqs.(5-20),(5-21)(5-18)):

$$\boldsymbol{P}_{el-DEMAND} - \boldsymbol{P}_{el-GRID} - \boldsymbol{P}_{el-mGT} - \boldsymbol{P}_{el-BES} = \mathbf{0} \quad (5\text{-}20)$$

$$\boldsymbol{P}_{th-DEMAND} - \boldsymbol{P}_{th-mGT} - \boldsymbol{P}_{th-TES} \leq \mathbf{0} \quad (5\text{-}21)$$

The same cost function and optimiser are applied to this optimisation problem. The decision variables for this problem are $\boldsymbol{P}_{el-mG}$ and $\boldsymbol{P}_{el-BESS-req}$. The approach for the calculation of all the parameters is similar to the previous case. In this case, the electrical power exchanged from the grid $\boldsymbol{P}_{el}$ is obtained from the new electricity balance (Eq.(5-20)) where $\boldsymbol{P}_{el-BESS}$ is calculated from $\boldsymbol{P}_{el-BESS-req}$ though the battery function (Eq. (5-14)).

Figure 5-5 displays the electrical and thermal power scheduling of the considered plant with a $ratio_{sell\text{-}buy}$ equal to 0 (Figure 5-5, left) and 1 (Figure 5-5, right), respectively. Both scenarios start with SOC_{TES} equal to 0 and battery with the minimum depth of discharge.The behaviour of the mGT and TES is similar to the baseline case. The TES is charged at the beginning of the day with the mGT at its minimum load and then discharge from 6 to 8 hours. After that it is charged again, mainly from 16 to 18 hours to satisfy the low thermal power at the end of the day and switch off the mGT.

For the case with $ratio_{sell/buy}$=0 the battery is charged from 3 to 5 hours instead of wasting the electrical energy (electricity is not sold to the grid) and then it is used to partially satisfy the electrical demand at time 9 and 10 hour where the electricity price is high. A second charge/discharge cycle start at t=14 hour where the electricity price is low. The accumulated energy is used at time 20 and 21 hours instead of buying at higher price. For the case with $ratio_{sell/buy}$ = 1, the battery is charged at low electricity price (3 hour) and discharged to sell to the grid at t= 8 hours. Another cycle starts at t=14 hour and finishes at t=21 hour. Overall, with $ratio_{sell/buy}$=0, the battery is used to avoid purchasing when the price is high, in this case C_{tot}=640.3 €/day while in the case of $ratio_{sell/buy}$=1, the battery is used to sell when the price is high C_{tot}=585.1 €/day.

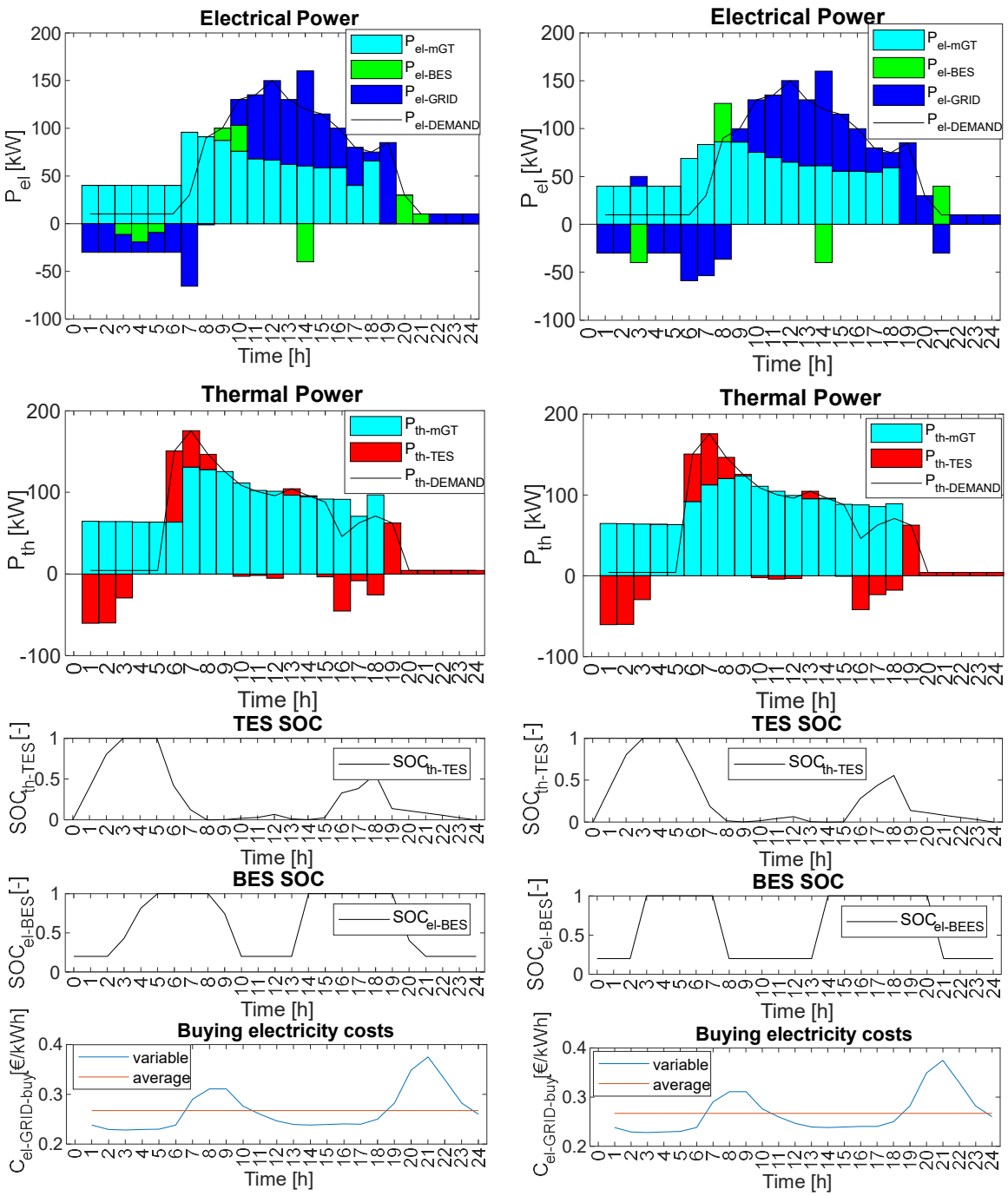

Figure 5-5. Electrical and thermal power scheduling of the plant with battery.

5.5 Baseline plant with the CAES system

The layout including the CAES system is shown in Figure 5-6 and it includes all the limitations considered in the previous chapter including the possibility to increase the mGT power output when injecting compressed air.

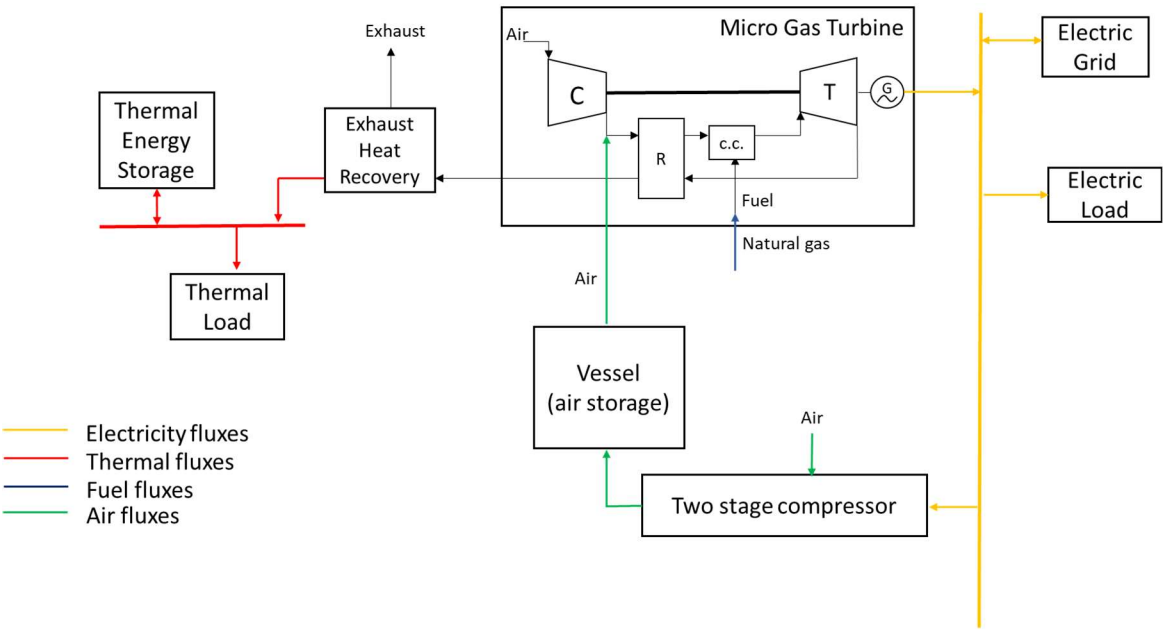

Figure 5-6. Plant layout with the CAES system.

The energy balance on the electrical side also considers the compressor power $\boldsymbol{P}_{el-COMPR}$ while on the thermal side the approach is again unvaried (Eqs.(5-22),(5-23)):

$$\boldsymbol{P}_{el-DEMAND} - \boldsymbol{P}_{el-GRID} - \boldsymbol{P}_{el-mGT} - \boldsymbol{P}_{el-COMPR} = \mathbf{0} \tag{5-22}$$

$$\boldsymbol{P}_{th-DEMAND} - \boldsymbol{P}_{th-mGT} - \boldsymbol{P}_{th-TES} \leq \mathbf{0} \tag{5-23}$$

The same cost function and optimiser are applied to this optimisation problem. The decision variables for this problem are $\boldsymbol{P}_{el-mGT}$, $\boldsymbol{P}_{el-COMPR}$ and the injected $\dot{\boldsymbol{m}}_{air-mGT-inj}$. The electrical power exchanged with the grid $\boldsymbol{P}_{el-GRID}$ is obtained from the new electricity balance (Eq.(5-20)) where $\boldsymbol{P}_{el-COMPR}$ is calculated from the compressor function (Eq. (5-15)). The value of $\dot{\boldsymbol{m}}_{air-mGT-inj}$ is kept within the acceptable limits for the mGT using Eq.(5-6) and Eq. (5-7) and the new mGT performance is calculated with Eq. (5-3).

Both scenarios start with SOC_{TES} equal to 0 and discharged air tank. Figure 5-7 displays only the electrical and thermal power scheduling of the considered plant with a $ratio_{sell\text{-}buy}$ equal to 0, which leads to an overall cost of C_{tot}=603.2 €/day. Again, the TES behaviour is similar to the previous cases. The compressor is used to compress air when there is an excess of mGT electricity production when the mGT is forced to operate at minimum load. The air injection in the mGT respects the machine limits: at low load the injected mass flow is low and higher at higher loads. The air injection also leads to increased power output in the central part of the day.

The case with $ratio_{sell\text{-}buy}$ = 1 is not displayed as it leads to a similar total cost C_{tot}=586.6 €/day as it is not convenient to compress at the initial pressure ratio of 50 bar. Therefore, a case with a lower pressure ratio, ß = 25 bar is also considered, and it is displayed in Figure 5-8. By reducing the pressure ratio, the total cost is reduced, although not significantly, C_{tot}=579.2 €/day. In this case, similarly to the case with BES the charging phase occurs when the electricity price is low and the discharging when the price is high in order to improve the efficiency of the mGT and increase the power output.

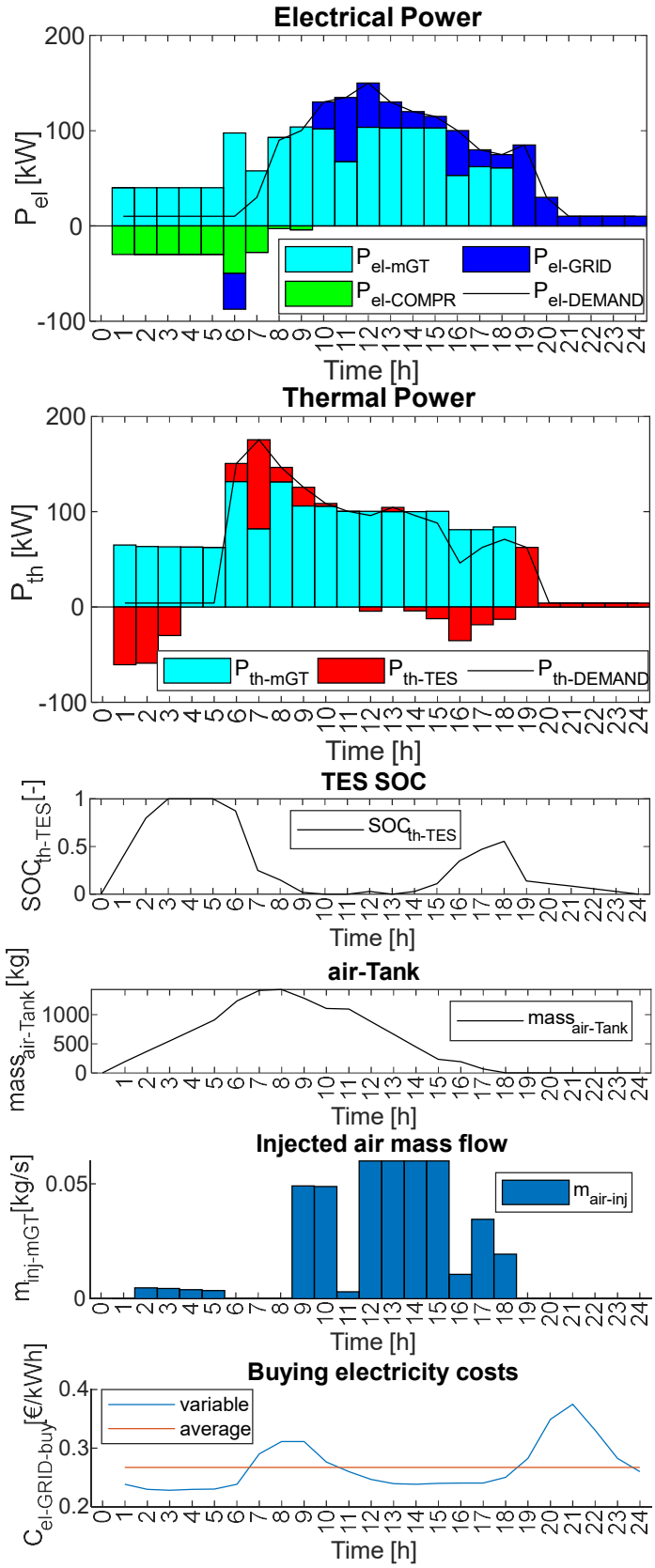

Figure 5-7. Electrical and thermal power scheduling of the plant with CAES ($ratio_{sell\text{-}buy}$ = 0).

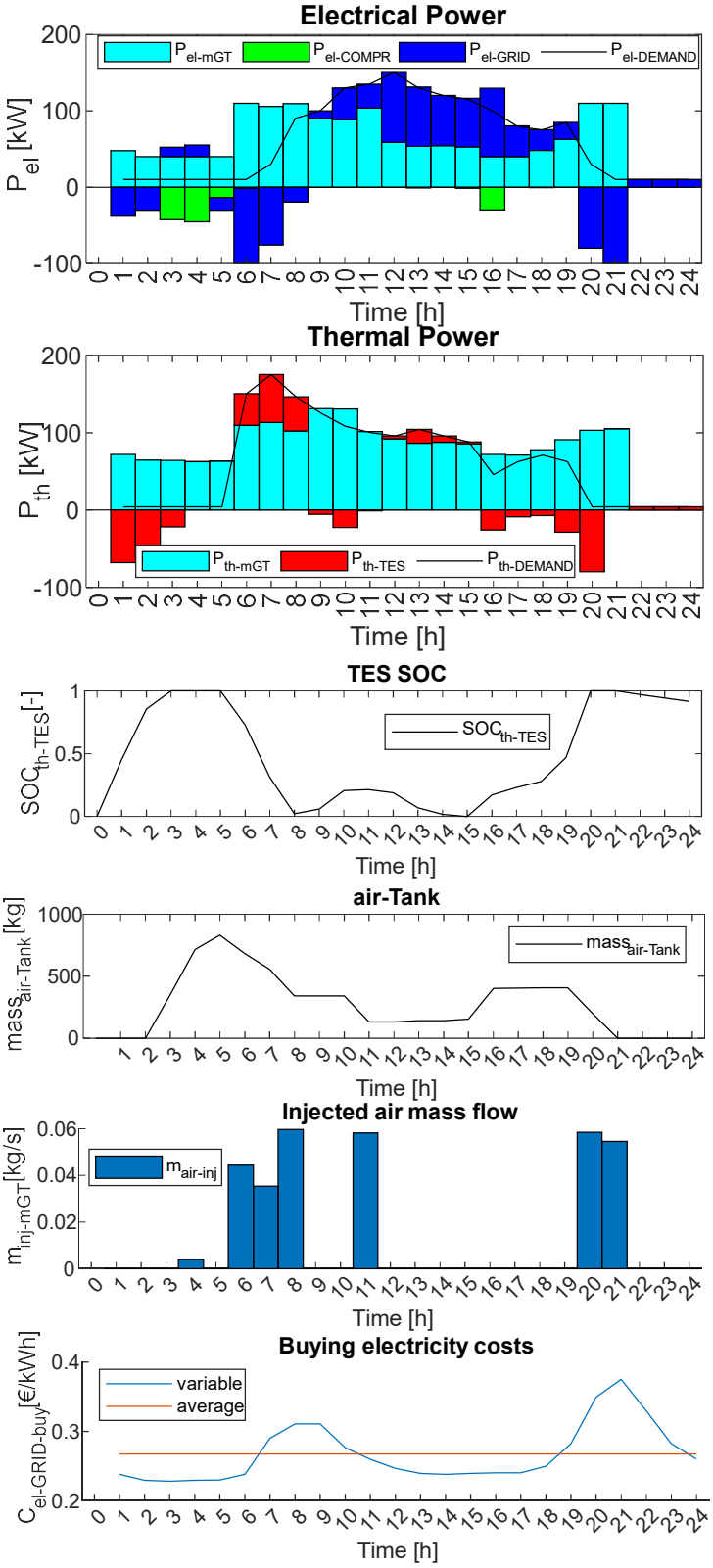

Figure 5-8. Electrical and thermal power scheduling of the plant with CAES ($ratio_{sell\text{-}buy}$ = 0 and β = 25).

5.6 Baseline plant with the electrolyser

The layout including the electrolyser is shown in Figure 5-9.

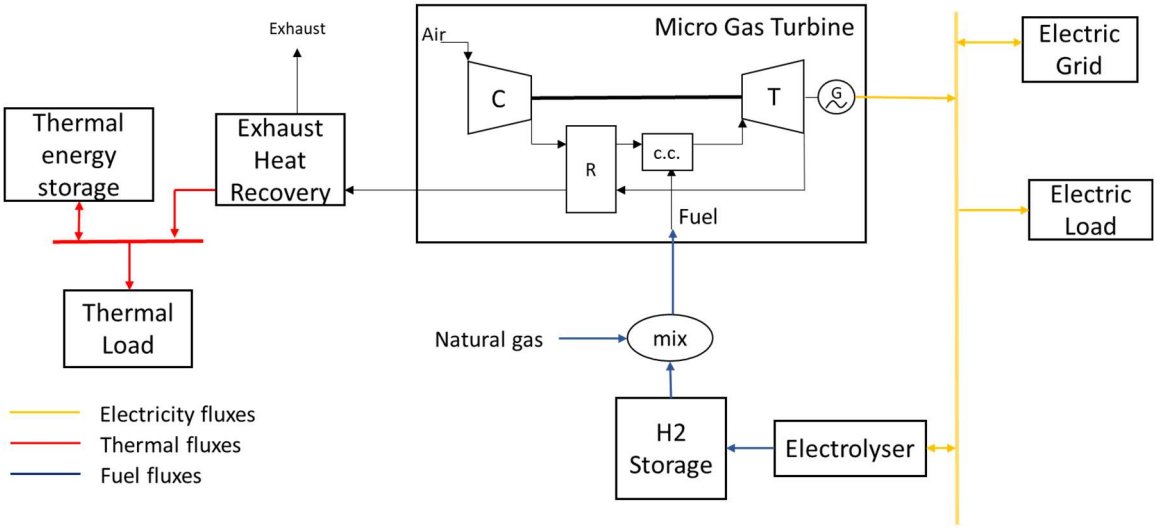

Figure 5-9. Plant layout with the electrolyser.

The energy balance on the electrical side also considers the electrolyser power $\boldsymbol{P}_{el-PEMEC}$ (Eqs.(5-24),(5-25)):

$$\boldsymbol{P}_{el-DEMAND} - \boldsymbol{P}_{el-GRID} - \boldsymbol{P}_{el-mGT} - \boldsymbol{P}_{el-PEMEC} = \boldsymbol{0} \tag{5-24}$$

$$\boldsymbol{P}_{th-DEMAND} - \boldsymbol{P}_{th-mGT} - \boldsymbol{P}_{th-TES} \leq \boldsymbol{0} \tag{5-25}$$

The same cost function and optimiser are applied to this optimisation problem. The decision variables for this problem are $\boldsymbol{P}_{el-mGT}$, $\boldsymbol{P}_{el-PEMEC}$ and the injected hydrogen $\dot{\boldsymbol{m}}_{H_2-mGT}$. The electrical power exchanged with the grid $\boldsymbol{P}_{el-GRID}$ is obtained from the new electricity balance (Eq.(5-24)) where $\boldsymbol{P}_{el-PEMEC}$ is calculated from the electrolyser function (Eq. (5-16)). The value of $\dot{\boldsymbol{m}}_{H_2-mGT}$ is kept within the operating limits for the mGT using Eq. (5-8) and Eq. (5-9) and the new mGT performance is calculated with Eq. (5-4).

Both scenarios start with SOC_{TES} equal to 0 and discharged hydrogen tank. Figure 5-10 displays only the electrical and thermal power scheduling of the considered plant with a $ratio_{sell\text{-}buy}$ equal to 0. In this case, C_{tot}= 621.4 €/day. With $ratio_{sell\text{-}buy}$ = 1 the optimal solution consists of not using the power to

hydrogen system, as it is more beneficial to sell the electricity instead of storing it in the form of hydrogen.

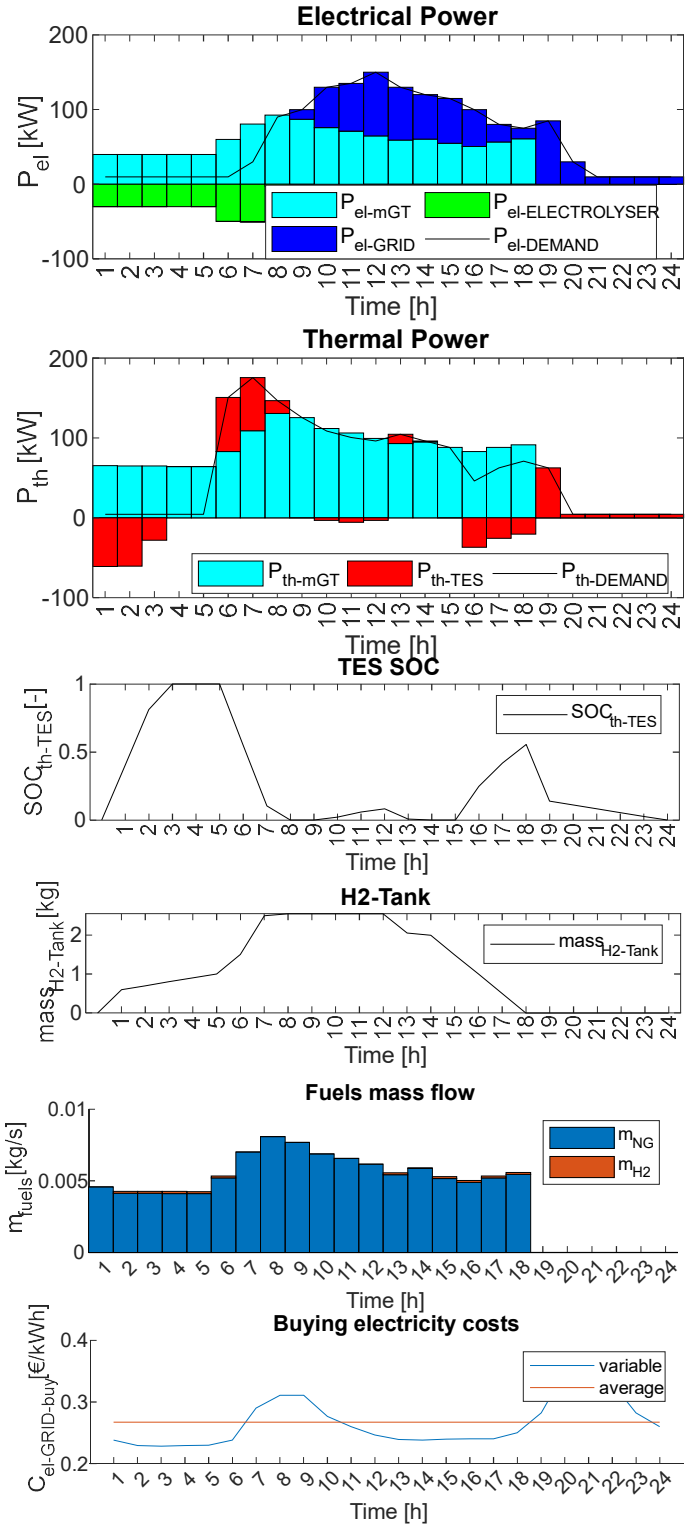

Figure 5-10. Electrical and thermal power scheduling of the plant with power-to-H_2 system ($ratio_{sell\text{-}buy}$ = 0).

The operation with H_2 is similar to the CAES case, since the electrolyser is used when the mGT operates at minimum load. The economic advantage is lower since the use of hydrogen has a less significant impact on the electrical efficiency and increase power output. Nevertheless, the amount of H_2 used in the mGT is very low compared to the NG. Since it is difficult to visualise the H_2 content from Figure 5-10, the same fuel plot is also reported separately in Figure 5-11.

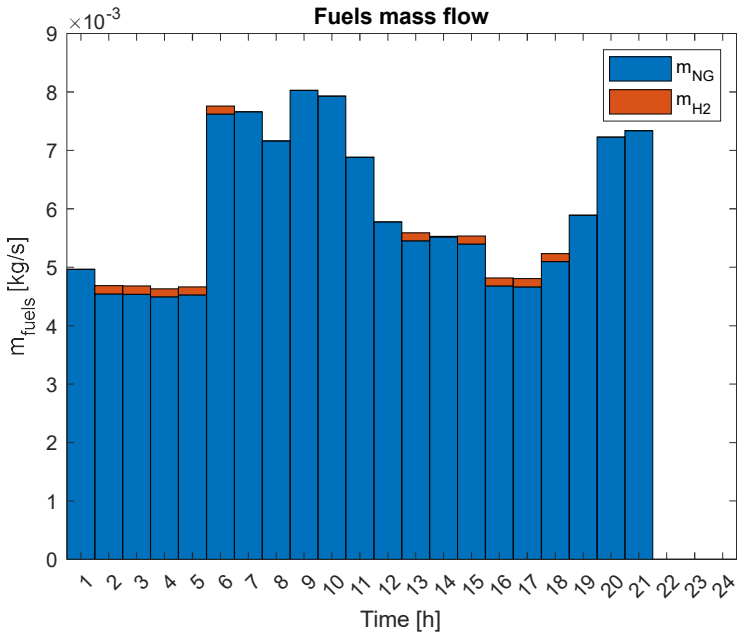

Figure 5-11. Hourly mGT fuel mass flow.

5.7 Global comparison of the layouts

A full comparison of the investigated layouts would require a complete sizing of the plants considering the capital costs of each component and the demands of at least a representative year. However, it is already possible to identify some characteristics of the different energy storage systems considering the results obtained in this work, which are summarised in Table 5-1.

In general, and as expected, the total plant costs are always higher $ratio_{sell\text{-}buy}=1$ due to the possibility to sell to the grid what is produced in excess (mainly from the mGT when it is forced to operate at the minimum load). All the energy storage systems provide an economic benefit by reducing the overall plant costs

except from the power-to-H_2 case when $ratio_{sell\text{-}buy}$ =1. The benefit of adding an ESS is always higher in the case $ratio_{sell\text{-}buy}$ =0 since the storage device can be used to exploit the excess of electricity produced and that cannot be sold. Instead, with the considered scenario, when $ratio_{sell\text{-}buy}$ =1, the ESS is used to buy at low price and sell to the grid at higher prices.

Table 5-1. Summary of costs for the different plant layouts

Parameter	Unit	Base layout: T100 and TES		Base layout with BES		Base layout with CAES		Base layout with power-to-H_2	
$ratio_{sell\text{-}buy}$	-	0	1	0	1	0	1	0	1
Plant total cost	€	656.2	593.8	640.3	585.1	603.2	586.6	621.4	593.8
mGT total cost	€	486.9	487.0	486.7	487.0	486.9	556.3	451.3	487.0
GRID total cost	€	169.3	106.7	153.5	97.9	116.3	30.3	170.1	106.7
Saving from baseline (absolute)	€	-	-	15.9	8.6	53.0	7.1	34.8	0.0
Saving from baseline (relative)	%	-	-	2.4%	1.5%	8.1%	1.2%	5.3%	0.0%

When $ratio_{sell\text{-}buy}$ =0, the storage system that provide higher relative cost savings (+8.1%) is the CAES system, this is due to the fact that the air injection increases both the electrical efficiency of the mGT and the maximum power output, while the effect of the thermal power reduction does not affect negatively the system due to the presence of the TES. The power-to-H_2 system also provides good relative savings (+5.3%), although the injection of H_2 does not significantly increase the efficiency of the T100 and the maximum power output compared to the CAES case. The least performing energy storage device is the battery with a relative saving of +2.4%.

When $ratio_{sell\text{-}buy}$ =1, the use of CAES and BES provide low and comparable energy savings, +1.2% and 2.4%, and the power-to- H_2 does not provide any advantage since the optimiser forces the electrolyser to switch off during all day.

5.7.1 General considerations on the capital costs

In this thesis chapter, the size of the components was fixed as the aim of this study was to understand optimal operating strategies of the micro gas turbine integrated with different storage devices. However, to determine the optimal size of the components, the capital costs should be considered in a complete analysis. Similarly to Paragraph 3.3.1, this paragraph discusses the effects of the ESSs capital costs. The CAPEX of batteries, for example li-ion batteries is around 400 €/kWh [139], while the cost of a PEM electrolyser can be assumed around 1500 €/kW [140]. For the selected sizes, the total BES cost would be 20'000 €, for the PEM electrolyser 75'000 €. The CAES system cost was calculated in Paragraph 3.3.1 and it is equal to 47'272 €. In a simplified scenario, if considering the same daily savings from each day over a lifetime of 20 years, it is possible to calculate the savings over the system lifetime and the net savings over the lifetime (subtracting the system CAPEX). These results are shown Table 5-2 and can give an estimation of expected plant costs. However, this does not represent a complete techno-economic analysis due to the several considered assumptions. The CAES system results in the highest cost savings when $ratio_{sell-buy}$=0, while the BES has the highest cost savings when $ratio_{sell-buy}$=1. A further analysis should be conducted by increasing the BES size to determine whether there could be an economical advantage over the CAES system due to the lower capital costs. Finally, the power-to- H_2 resulted in the least economical layout.

Table 5-2. Cost analysis results.

Parameter	Unit	Base layout: T100 and TES		Base layout with BES		Base layout with CAES		Base layout with power-to-H_2	
$ratio_{sell\text{-}buy}$	-	0	1	0	1	0	1	0	1
Saving from baseline (absolute)	€	-	-	15.9	8.6	53	7.1	34.8	0
Savings over lifetime	€	-	-	116070	62780	386900	51830	254040	0
Net savings over lifetime	€	-	-	96070	42780	339628	4558	179040	-75000

5.8 Conclusions

In conclusion, this chapter focused on the development of an energy scheduler for various plant layouts, incorporating a T100 micro gas turbine integrated with different energy storage systems. Four configurations have been examined and compared:

1. A baseline plant including a T100 and a latent heat thermal energy storage (TES) system with possibility to exchange electricity with the grid.

2. The baseline plant integrated with a BES.

3. The baseline plant integrated with a CAES system.

4. The baseline plant integrated with a power-to-H_2 system.

A common scenario for the optimisation involves was selected including electrical and thermal demands, ambient temperature, electricity costs, and natural gas costs of a representative day of April 2022. The study utilised load profiles and ambient conditions from historical operations of a "Smart Polygeneration Microgrid" at UNIGE University Campus, with a scaling factor to accommodate for the smaller plant layouts under consideration. The chapter also discussed the modelling of component performance, operational limits, and

operational costs. For the T100 mGT performance, the off-design curves were derived from the results obtained in Chapter 2, 3 and 4 for the standard operation, air injection, or hydrogen blends respectively. Also, the previously obtained operational limits for various cases were formulated, such as the minimum and maximum operating range of the mGT, compressed air mass flow rates for CAES, and hydrogen flow rates for the power-to-H_2 system.

While a detailed comparison involving complete plant sizing and annual demand patterns would be necessary to provide a more accurate assessment, the findings presented in this chapter offer valuable preliminary observations. The analysis conducted on the various plant layouts has led to valuable insights into the economic benefits of the ESSs integrated with the mGTs. This is primarily due to the ability of these systems to mitigate excess electricity production, especially in scenarios where surplus power cannot be sold to the grid ($ratio_{sell\text{-}buy} = 0$). Under these circumstances, all the energy storage systems effectively reduce the overall plant costs, with the CAES system showing the highest relative cost savings at +8.1%, followed by the power-to-H_2 system with +5.3%. This outcome is attributed to the CAES system capability to enhance the efficiency and power output of the micro gas turbine through air injection. Conversely, when considering a scenario where the excess electricity can be sold to the grid ($ratio_{sell\text{-}buy} = 1$), the economic benefits of energy storage systems are reduced. In this context, both CAES and BES systems offer modest and comparable energy savings of +1.2% and +2.4% respectively, as they facilitate buying electricity at lower prices and selling it at higher rates, while the power-to-H_2 system fails to provide any.

6 Conclusions

In summary, this thesis presented different aspects of a T100 micro gas turbine (mGT), ranging from its coupling with compressed air energy storage (CAES) systems, to the effects of fuel composition changes, and the development of an energy scheduler for diverse plant layouts including different energy storage systems.

In the first part, an analysis of the T100 micro gas turbine combined with a small second-generation CAES system was performed. The CAES system included a two-stage reciprocating compressor with cooling, a storage vessel for compressed air, and an extra recuperator for pre-heating air. The study also examined the potential of a Tesla turbine for additional power recovery. The main outcomes highlighted the benefits of integrating the T100 with CAES, including improved efficiency, reduced fuel consumption, and enhanced renewable energy storage. The focus was also on ensuring safe operation, both under steady-state conditions and during dynamic scenarios. The analysis consisted with a steady-state investigation of the micro gas turbine behaviour with varying compressed air injection at different power outputs. It identified that injecting higher mass flow rates is possible at higher power outputs, leading to an increase of efficiency. For instance, at 80 kW net power, a maximum mass flow rate of 50 g/s increases efficiency by 3.23%. The study then considered the dynamic analysis of the micro gas turbine with the CAES system. It analysed the surge margin reduction during step injections, particularly pronounced at higher loads and injection rates. This indicated potential instability issues during these scenarios. However, using injection ramps instead of steps can maintain acceptable surge margins and reduce power and temperature oscillations. A ramp rate of +0.5 (g/s)/s was identified as a suitable compromise for safe and rapid dynamic mode operation. The overall findings are significant for managing the mGT/CAES system in commercial applications, preventing dangerous operations, and proposing an approach that could be applicable to other microturbines. By defining air injection constraints and ramp rates, the

operational range of the system can be extended safely, positively impacting flexibility, energy sustainability, pollution reduction, and cost savings.

In the second part, the impact of changes in the fuel composition on the performance and behaviour of the T100 micro gas turbine (mGT) was investigated. While most existing research focuses on enhancing combustion stability and performance with alternative fuels, this study considered the broader effects of varying H_2-NG and NH_3-NG blends on both steady-state and transient performance. This investigation is important for adapting mGTs to flexible operation with diverse fuel mixtures. The study used a modified T100 setup, injecting hydrogen or ammonia into the main fuel line while keeping the pilot line supplied with natural gas. Steady-state results for different fuel compositions showed lower rotational speeds, contributing to higher power output, regardless of whether hydrogen or ammonia was used. Notably, using 100% H_2 increased the power output by +6.1 kW, and 100% NH_3 increases it by up to +11.3 kW compared to baseline with 100% NG operation. The steady-state results also showed that the surge margin decreases only for NH3-NG blends due to increased fuel mass flow requirements for a given power output. The study examined transient power decrease steps to determine safe levels of ammonia injection for stable operation. It was highlighted that during high-power operation, such as stepping from 80 kW to 70 kW, the surge margin remains above the acceptable threshold of 1.1. However, at lower power levels, critical conditions can be reached. For instance, in a step from 50 kW to 40 kW, the presence of ammonia lowered the surge margin below 1.1. This highlights the need for careful consideration, especially at low power conditions, where slower rate transitions are advisable. Furthermore, the study conducted transient simulations to analyse potential over-temperatures resulting from sudden injections of H_2 or NH_3 into the main fuel line. Step changes in composition, adding 10%, 50%, and 80% hydrogen or ammonia to natural gas, were tested at a constant power output to identify excessive temperature spikes. The TRANSEO approach was successfully used to define controlled ramps for varying fuel percentages in the mixture, preventing extreme temperature

peaks. Gradual linear injections prove beneficial, decreasing temperature fluctuations and increasing surge margin during transients.

The last chapter focused on the development of an energy scheduler for different plant setups using the previously analysed T100 combined with various energy storage systems. The study evaluated four plant layouts: a baseline configuration with a micro gas turbine and thermal storage, the same baseline with added battery storage, the integration of a compressed air storage, and the incorporation of a power-to-hydrogen system. The aim was to develop an optimisation approach and to compare and analyse the performance and capabilities of the different energy storage systems when integrated with the T100. The optimisation involved the identification of a common scenario with electrical and thermal demands, ambient temperature, electricity and natural gas costs. Data from a "Smart Polygeneration Microgrid" at UNIGE University Campus were used and adjusted for the smaller plant layouts. The chapter explained how the performance of the components, operational limits, and costs were modelled. In particular, the performance functions for the T100 were derived based on off-design curves derived by the previous analysis with TRANSEO, which vary based on operational mode (standard, with air injection and fuel flexible mode with hydrogen). Furthermore, the identified operational limits were also respected for different cases, including the micro gas turbine minimum and maximum operating range, compressed air mass flow rates for the CAES, and hydrogen flow rates for the power-to-H2 system.

The results of this analysis showed that the ESSs can provide significant advantages especially when managing surplus electricity production, particularly when the excess power cannot be sold to the grid ($ratio_{sell\text{-}buy} = 0$). In such scenarios, all energy storage systems effectively reduced overall plant costs. Among these, the CAES system was the most performing, providing the most substantial relative cost savings of +8.1%, followed by the power-to-H2 system at +5.3%. This favourable outcome for CAES system can be attributed to its capability to enhance both the mGT efficiency and power output through air

injection. Conversely, when considering a scenario where excess electricity can be exported to the grid ($ratio_{sell\text{-}buy}$ = 1), the economic benefits of the ESSs diminish. Under these conditions, both CAES and BES systems showed modest energy savings of +1.2% and +2.4%, respectively. This reduction in savings occurs as these systems were used to purchase electricity at lower prices and sell it at higher prices. In contrast, the power-to-H_2 system failed to confer any economic advantage in this context. Furthermore, this analysis provided the basis for subsequent analyses of energy scheduling of micro gas turbines integrated with different energy storage systems.

Project acknowledgements

This project has received funding from the European Union's Horizon 2020 research and innovation programme under the Marie Sklodowska-Curie grant agreement No 861079 ("NextMGT - Next Generation of Micro Gas Turbines for High Efficiency, Low Emissions, and Fuel Flexibility"). This paper reflects only the authors' view and the Research Executive Agency and the European Commission are not responsible for any use that may be made of the information it contains.

Bibliography

[1] International Energy Agency, 2022, "International Energy Agency (IEA) World Energy Outlook 2022," Https://Www.Iea.Org/Reports/World-Energy-Outlook-2022/Executive-Summary, p. 524.

[2] Maamoun, N., 2019, "The Kyoto Protocol: Empirical Evidence of a Hidden Success," J. Environ. Econ. Manage., **95**, pp. 227–256.

[3] 2016, "Paris Agreement," (54113).

[4] Hannah Ritchie, and Max Roser, 2020, "CO_2 and Greenhouse Gas Emissions - Our World in Data," Our World Data, p. 1.

[5] International Renewable Energy Agency (IRENA), 2022, "World Energy Transitions Outlook 2022: 1.5° C Pathway -Executive Summary," World Energy Transitions, pp. 1–54.

[6] Hallegatte, S., Bangalore, M., Bonzanigo, L., Fay, M., Kane, T., Narloch, U., Rozenberg, J., Treguer, D., and Vogt-Schilb, A., 2016, "Poverty and Climate Change," Econ. Clim. Dev., pp. 33–52.

[7] Church, C., and Crawford, A., 2020, *Minerals and the Metals for the Energy Transition: Exploring the Conflict Implications for Mineral-Rich, Fragile States*, Springer International Publishing.

[8] Hodge, B. M. S., Jain, H., Brancucci, C., Seo, G. S., Korpås, M., Kiviluoma, J., Holttinen, H., Smith, J. C., Orths, A., Estanqueiro, A., Söder, L., Flynn, D., Vrana, T. K., Kenyon, R. W., and Kroposki, B., 2020, "Addressing Technical Challenges in 100% Variable Inverter-Based Renewable Energy Power Systems," Wiley Interdiscip. Rev. Energy Environ., **9**(5), pp. 1–19.

[9] Ryan Kennedy, 2023, "California's Electricity Duck Curve Is Deepening," PV Mag.

[10] IRENA, 2020, "Advanced Forecasting of Variable Renewable Power Generation."

[11] Pierre Pinson, "Current Challenges with Renewables in Electricity Markets."

[12] Akinyele, D. O., and Rayudu, R. K., 2014, "Review of Energy Storage Technologies for Sustainable Power Networks," Sustain. Energy Technol. Assessments, **8**, pp. 74–91.

[13] Bouakkaz, A., Mena, A. J. G., Haddad, S., and Ferrari, M. L., 2021, "Efficient Energy Scheduling Considering Cost Reduction and Energy Saving in Hybrid Energy System with Energy Storage," J. Energy Storage, **33**(August 2020), p. 101887.

[14] Faisal, M., Hannan, M. A., Ker, P. J., Hussain, A., Mansor, M. Bin, and Blaabjerg, F., 2018, "Review of Energy Storage System Technologies in

Microgrid Applications: Issues and Challenges," IEEE Access, **6**, pp. 35143–35164.

[15] AL Shaqsi, A. Z., Sopian, K., and Al-Hinai, A., 2020, "Review of Energy Storage Services, Applications, Limitations, and Benefits," Energy Reports, **6**, pp. 288–306.

[16] Krishan, O., and Suhag, S., 2019, "An Updated Review of Energy Storage Systems: Classification and Applications in Distributed Generation Power Systems Incorporating Renewable Energy Resources," Int. J. Energy Res., **43**(12), pp. 6171–6210.

[17] Beaudin, M., Zareipour, H., Schellenberglabe, A., and Rosehart, W., 2010, "Energy Storage for Mitigating the Variability of Renewable Electricity Sources: An Updated Review," Energy Sustain. Dev., **14**(4), pp. 302–314.

[18] Sprake, D., Vagapov, Y., Lupin, S., and Anuchin, A., 2017, "Housing Estate Energy Storage Feasibility for a 2050 Scenario," 2017 Internet Technol. Appl. ITA 2017 - Proc. 7th Int. Conf., (September), pp. 137–142.

[19] Behabtu, H. A., Messagie, M., Coosemans, T., Berecibar, M., Fante, K. A., Kebede, A. A., and Van Mierlo, J., 2020, "A Review of Energy Storage Technologies' Application Potentials in Renewable Energy Sources Grid Integration," Sustain., **12**(24), pp. 1–20.

[20] Ibrahim, H., Ilinca, A., and Perron, J., 2008, "Energy Storage Systems-Characteristics and Comparisons," Renew. Sustain. Energy Rev., **12**(5), pp. 1221–1250.

[21] Ferrari, M. L., Cuneo, A., Pascenti, M., and Traverso, A., 2017, "Real-Time State of Charge Estimation in Thermal Storage Vessels Applied to a Smart Polygeneration Grid," Appl. Energy, **206**(November 2016), pp. 90–100.

[22] Zhu, C., Zhang, J., Wang, Y., Deng, Z., Shi, P., Wu, J., and Wu, Z., 2022, "Study on Thermal Performance of Single-Tank Thermal Energy Storage System with Thermocline in Solar Thermal Utilization," Appl. Sci., **12**(8).

[23] Bloemendal, M., Jaxa-rozen, M., and Rostampour, V., 2017, "Aquifer Thermal Energy Storage Improved Performance of Heat Pumps Helps to Use Full Potential of Subsurface Space for Aquifer Thermal Energy Storage."

[24] Liu, W., Li, Q., Yang, C., Shi, X., Wan, J., Jurado, M. J., Li, Y., Jiang, D., Chen, J., Qiao, W., Zhang, X., Fan, J., Peng, T., and He, Y., 2023, "The Role of Underground Salt Caverns for Large-Scale Energy Storage: A Review and Prospects," Energy Storage Mater., **63**(October), p. 103045.

[25] Okello, D., Omony, R., Nyeinga, K., and Chaciga, J., 2022, "Performance Analysis of Thermal Energy Storage System Integrated with a Cooking Unit," Energies, **15**(23), pp. 1–19.

[26] Villada, C., Ding, W., Bonk, A., and Bauer, T., 2022, "Simulation-Assisted Determination of the Minimum Melting Temperature Composition of

MgCl2–KCl–NaCl Salt Mixture for Next-Generation Molten Salt Thermal Energy Storage," Front. Energy Res., **10**(March), pp. 1–10.

[27] Wang, R., Ni, L., Yang, C., and Yao, Y., 2021, "Laboratory Study on the Thermal Performance of Vertical U-Tube Ground Heat Exchanger during Short-Term Borehole Thermal Energy Storage (BTES) and Heat Extraction Process," Int. J. Energy Res., **45**(2), pp. 2043–2057.

[28] Liu, W., Bie, Y., Xu, T., Cichon, A., Królczyk, G., and Li, Z., 2022, "Heat Transfer Enhancement of Latent Heat Thermal Energy Storage in Solar Heating System: A State-of-the-Art Review," J. Energy Storage, **46**(November 2021).

[29] Fallahi, A., Guldentops, G., Tao, M., Granados-Focil, S., and Van Dessel, S., 2017, "Review on Solid-Solid Phase Change Materials for Thermal Energy Storage: Molecular Structure and Thermal Properties," Appl. Therm. Eng., **127**, pp. 1427–1441.

[30] MacPhee, D., and Dincer, I., 2009, "Performance Assessment of Some Ice TES Systems," Int. J. Therm. Sci., **48**(12), pp. 2288–2299.

[31] Kumar, N., Gupta, S. K., and Sharma, V. K., 2021, "Application of Phase Change Material for Thermal Energy Storage: An Overview of Recent Advances," Mater. Today Proc., **44**, pp. 368–375.

[32] Zhou, X., Mahmood, M., Chen, J., Yang, T., Xiao, G., and Ferrari, M. L., 2019, "Validated Model of Thermochemical Energy Storage Based on Cobalt Oxides," Appl. Therm. Eng., **159**(June), p. 113965.

[33] Abedin, A. H., 2011, "A Critical Review of Thermochemical Energy Storage Systems," Open Renew. Energy J., **4**(1), pp. 42–46.

[34] Divya, K. C., and Østergaard, J., 2009, "Battery Energy Storage Technology for Power Systems-An Overview," Electr. Power Syst. Res., **79**(4), pp. 511–520.

[35] Itani, K., and De Bernardinis, A., 2023, "Review on New-Generation Batteries Technologies: Trends and Future Directions," Energies, **16**(22), p. 7530.

[36] Hemavathi, S., Srirama, S., and Prakash, A. S., 2023, "Present and Future Generation of Secondary Batteries: A Review," ChemBioEng Rev., (6), pp. 1123–1145.

[37] Li, C., Wang, Z. yu, He, Z. jiang, Li, Y. jiao, Mao, J., Dai, K. hua, Yan, C., and Zheng, J. chao, 2021, "An Advance Review of Solid-State Battery: Challenges, Progress and Prospects," Sustain. Mater. Technol., **29**(April), p. e00297.

[38] Vangapally, N., Rao, T., Elias, Y., Muduli, S., Maddukuri, S., Luski, S., Aurbach, D., and Kumar, S., 2023, "Lead-Acid Batteries and Lead – Carbon Hybrid Systems : A Review," J. Power Sources, **579**(April), p. 233312.

[39] Yang, Y., Wang, R., Shen, Z., Yu, Q., Xiong, R., and Shen, W., 2023, "Towards a Safer Lithium-Ion Batteries: A Critical Review on Cause, Characteristics, Warning and Disposal Strategy for Thermal Runaway," Adv. Appl. Energy, **11**(April), p. 100146.

[40] David, J., 1995, "Nickel-Cadmium Battery Recycling Evolution in Europe," J. Power Sources, **57**(1–2), pp. 71–73.

[41] Sudworth, J. L., 1984, "The Sodium/Sulphur Battery," J. Power Sources, **11**(1–2), pp. 143–154.

[42] Blurton, K. F., and Sammells, A. F., 1979, "Metal/Air Batteries: Their Status and Potential - a Review," J. Power Sources, **4**(4), pp. 263–279.

[43] Soloveichik, G. L., 2015, "Flow Batteries: Current Status and Trends," Chem. Rev., **115**(20), pp. 11533–11558.

[44] International Renewable Energy Agency (IRENA), 2022, "Global Hydrogen Review 2022," Glob. Hydrog. Rev. 2022.

[45] Noussan, M., Raimondi, P. P., Scita, R., and Hafner, M., 2021, "The Role of Green and Blue Hydrogen in the Energy Transition—a Technological and Geopolitical Perspective," Sustain., **13**(1), pp. 1–26.

[46] Walker, S. B., Van Lanen, D., Fowler, M., and Mukherjee, U., 2016, "Economic Analysis with Respect to Power-to-Gas Energy Storage with Consideration of Various Market Mechanisms," Int. J. Hydrogen Energy, **41**(19), pp. 7754–7765.

[47] Götz, M., Lefebvre, J., Mörs, F., McDaniel Koch, A., Graf, F., Bajohr, S., Reimert, R., and Kolb, T., 2016, "Renewable Power-to-Gas: A Technological and Economic Review," Renew. Energy, **85**, pp. 1371–1390.

[48] Morales-Ospino, R., Celzard, A., and Fierro, V., 2023, "Strategies to Recover and Minimize Boil-off Losses during Liquid Hydrogen Storage," Renew. Sustain. Energy Rev., **182**(April), p. 113360.

[49] Abe, J. O., Popoola, A. P. I., Ajenifuja, E., and Popoola, O. M., 2019, "Hydrogen Energy, Economy and Storage: Review and Recommendation," Int. J. Hydrogen Energy, **44**(29), pp. 15072–15086.

[50] Züttel, A., 2004, "Hydrogen Storage Methods," Naturwissenschaften, **91**(4), pp. 157–172.

[51] Bellotti, D., Rivarolo, M., and Magistri, L., 2022, "A Comparative Techno-Economic and Sensitivity Analysis of Power-to-X Processes from Different Energy Sources," Energy Convers. Manag., **260**(January), p. 115565.

[52] Valera-Medina, A., Xiao, H., Owen-Jones, M., David, W. I. F., and Bowen, P. J., 2018, "Ammonia for Power," Prog. Energy Combust. Sci., **69**, pp. 63–102.

[53] Atsonios, K., Li, J., and Inglezakis, V. J., 2023, "Process Analysis and Comparative Assessment of Advanced Thermochemical Pathways for E-

Kerosene Production," Energy, **278**(PA), p. 127868.

[54] Zvirgzdins, J., and Linkevics, O., 2020, "Pumped-Storage Hydropower Plants as Enablers for Transition to Circular Economy in Energy Sector: A Case of Latvia," Latv. J. Phys. Tech. Sci., **57**(3), pp. 20–31.

[55] Bamisile, O., Zheng, Z., Adun, H., Cai, D., Ting, N., and Huang, Q., 2023, "Development and Prospect of Flywheel Energy Storage Technology: A Citespace-Based Visual Analysis," Energy Reports, **9**, pp. 494–505.

[56] Wang, J., Lu, K., Ma, L., Wang, J., Dooner, M., Miao, S., Li, J., and Wang, D., 2017, "Overview of Compressed Air Energy Storage and Technology Development," Energies, **10**(7).

[57] Briola, S., Di Marco, P., Gabbrielli, R., and Riccardi, J., 2016, "A Novel Mathematical Model for the Performance Assessment of Diabatic Compressed Air Energy Storage Systems Including the Turbomachinery Characteristic Curves," Appl. Energy, **178**, pp. 758–772.

[58] Yao, E., Wang, H., Wang, L., Xi, G., and Maréchal, F., 2016, "Thermo-Economic Optimization of a Combined Cooling, Heating and Power System Based on Small-Scale Compressed Air Energy Storage," Energy Convers. Manag., **118**, pp. 377–386.

[59] Minutillo, M., Lubrano Lavadera, A., and Jannelli, E., 2015, "Assessment of Design and Operating Parameters for a Small Compressed Air Energy Storage System Integrated with a Stand-Alone Renewable Power Plant," J. Energy Storage, **4**, pp. 135–144.

[60] Mcculloch, C., Ghavami, M., Zaili, J. Al, and Sayma, A., 2020, "Design and Analysis of an Adiabatic Micro-Compressed Air Energy Storage System," pp. 1–9.

[61] Zhao, P., Wang, M., Wang, J., and Dai, Y., 2015, "A Preliminary Dynamic Behaviors Analysis of a Hybrid Energy Storage System Based on Adiabatic Compressed Air Energy Storage and Flywheel Energy Storage System for Wind Power Application," Energy, **84**, pp. 825–839.

[62] Gouda, E. M., Fan, Y., Benaouicha, M., Neu, T., and Luo, L., 2021, "Review on Liquid Piston Technology for Compressed Air Energy Storage," J. Energy Storage, **43**(June), p. 103111.

[63] Chen, H., Peng, Y. hang, Wang, Y. ling, and Zhang, J., 2020, "Thermodynamic Analysis of an Open Type Isothermal Compressed Air Energy Storage System Based on Hydraulic Pump/Turbine and Spray Cooling," Energy Convers. Manag., **204**(November 2019), p. 112293.

[64] Arnulfi, G. L., and Croce, G., 2020, "Compressed Air Energy Storage for a Small Size Standalone Plant Powered by a Solar Power Unit and a Gas Turbine," Proc. ASME Turbo Expo, **5**, pp. 1–10.

[65] Salvini, C., 2018, "Performance Analysis of Small Size Compressed Air Energy Storage Systems for Power Augmentation: Air Injection and Air

Injection/Expander Schemes," Heat Transf. Eng., **39**(3), pp. 304–315.

[66] Salvini, C., 2015, "Techno-Economic Analysis of Small Size Second Generation CAES System," Energy Procedia, **82**, pp. 782–788.

[67] Akorede, M. F., Hizam, H., and Pouresmaeil, E., 2010, "Distributed Energy Resources and Benefits to the Environment," Renew. Sustain. Energy Rev., **14**(2), pp. 724–734.

[68] Pierre Pinson, and Prices, D., "Fundamental of Electricity Markets - Historiacal Perspective."

[69] Jiayi, H., Chuanwen, J., and Rong, X., 2008, "A Review on Distributed Energy Resources and MicroGrid," Renew. Sustain. Energy Rev., **12**(9), pp. 2472–2483.

[70] Bouakkaz, A., Mena, A. J. G., Haddad, S., and Ferrari, M. L., 2021, "Efficient Energy Scheduling Considering Cost Reduction and Energy Saving in Hybrid Energy System with Energy Storage," J. Energy Storage, **33**(March 2020), p. 101887.

[71] Pilavachi, P. A., 2002, "Mini- and Micro-Gas Turbines for Combined Heat and Power," Appl. Therm. Eng., **22**(18), pp. 2003–2014.

[72] Magistri, L., Costamagma, P., Massardo, A. F., Rodgers, C., and MacDonald, C. F., 2002, "A Hybrid System Based on a Personal Turbine (5 KW) and a Solid Oxide Fuel Cell Stack: A Flexible and High Efficiency Energy Concept for the Distributed Power Market," J. Eng. Gas Turbines Power, **124**(4), pp. 850–857.

[73] Giugno, A., Mantelli, L., Cuneo, A., and Traverso, A., 2020, "Performance Analysis of a Fuel Cell Hybrid System Subject to Technological Uncertainties," Appl. Energy, **279**(August), p. 115785.

[74] Cappelletti, A., Martelli, F., Bianchi, E., and Trifoni, E., 2014, "Numerical Redesign of 100kW MGT Combustor for 100% H2 Fueling," Energy Procedia, **45**, pp. 1412–1421.

[75] Calabria, R., Chiariello, F., Massoli, P., and Reale, F., 2014, "Part Load Behavior of a Micro Gas Turbine FED with Different Fuels," Proc. ASME Turbo Expo 2014, **1B**, pp. 1–11.

[76] du Toit, M., Engelbrecht, N., Oelofse, S. P., and Bessarabov, D., 2020, "Performance Evaluation and Emissions Reduction of a Micro Gas Turbine via the Co-Combustion of H2/CH4/CO2 Fuel Blends," Sustain. Energy Technol. Assessments, **39**(March), p. 100718.

[77] Devriese, C., Pennings, W., de Reuver, H., Bastiaans, R., and De Paepe, W., 2019, "The Preliminary CFD Design of a Compressor and Combustor System Towards a 100 KW Hydrogen Fuelled Micro Gas Turbine," Proc. ASME Turbo Expo 2019, pp. 1–10.

[78] Tuccillo, R., Cameretti, M. C., De Robbio, R., Reale, F., and Chiariello, F., 2019, "Methane-Hydrogen Blends in Micro Gas Turbines: Comparison of

Different Combustor Concepts," Proc. ASME Turbo Expo 2019, pp. 1–13.

[79] Kobayashi, H., Hayakawa, A., Somarathne, K. D. K. A., and Okafor, E. C., 2019, "Science and Technology of Ammonia Combustion," Proc. Combust. Inst. 37, pp. 109–133.

[80] Valera-Medina, A., Morris, S., Runyon, J., Pugh, D. G., Marsh, R., Beasley, P., and Hughes, T., 2015, "Ammonia, Methane and Hydrogen for Gas Turbines," *Energy Procedia 75*, pp. 118–123.

[81] Rocha, R. C., Ramos, C. F., Costa, M., and Bai, X. S., 2019, "Combustion of NH3/CH4/Air and NH3/H2/Air Mixtures in a Porous Burner: Experiments and Kinetic Modeling," Energy and Fuels, **33**(12), pp. 12767–12780.

[82] "FLEXnCONFU – FLEXibilize Combined Cycle Power Plant through Power- to-X Solutions Using CONventional Fuels."

[83] Iki, N., Kurata, O., Matsunuma, T., Inoue, T., Suzuki, M., Tsujimura, T., and Furutani, H., 2014, "Micro Gas Turbine Operation with Kerosene and Ammonia," 11th Annu. NH3 fuel Conf., pp. 1–22.

[84] Iki, N., Kurata, O., Matsunuma, T., Inoue, T., Tsujimura, T., Furutani, H., Kobayashi, H., Hayakawa, A., Ichikawa, A., and Arakawa, Y., 2016, "Micro Gas Turbine Firing Ammonia," *Proceedings of ASME Turbo Expo 2016*, pp. 1–6.

[85] Kurata, O., Iki, N., Inoue, T., Fujitani, T., Fan, Y., Matsunuma, T., Tsujimura, T., Furutani, H., Kawano, M., Arai, K., Okafor, E. C., Hayakawa, A., and Kobayashi, H., 2019, "Pure Ammonia Combustion Micro Gas Turbine System."

[86] Kurata, O., Iki, N., Fan, Y., Matsunuma, T., Inoue, T., Tsujimura, T., Furutani, H., Kawano, M., Arai, K., Okafor, E. C., Hayakawa, A., and Kobayashi, H., 2021, "Start-up Process of 50kW-Class Gas Turbine Firing Ammonia Gas," *Proceedings of ASME Turbo Expo 2021*, pp. 1–7.

[87] Heidari, M., Parra, D., and Patel, M. K., 2021, "Physical Design, Techno-Economic Analysis and Optimization of Distributed Compressed Air Energy Storage for Renewable Energy Integration," J. Energy Storage, **35**(August 2020), p. 102268.

[88] Facci, A. L., Sánchez, D., Jannelli, E., and Ubertini, S., 2015, "Trigenerative Micro Compressed Air Energy Storage: Concept and Thermodynamic Assessment," Appl. Energy, **158**, pp. 243–254.

[89] Congedo, P. M., Baglivo, C., Panico, S., Mazzeo, D., and Matera, N., 2022, "Optimization of Micro-CAES and TES Systems for Trigeneration Optimization of Micro - CAES and TES Systems for Trigeneration," (August).

[90] Dib, G., Haberschill, P., Rullière, R., and Revellin, R., 2021, "Modelling Small-Scale Trigenerative Advanced Adiabatic Compressed Air Energy

Storage for Building Application," Energy, **237**(December 2019).

[91] Wang, X., Yang, C., Huang, M., and Ma, X., 2018, "Multi-Objective Optimization of a Gas Turbine-Based CCHP Combined with Solar and Compressed Air Energy Storage System," Energy Convers. Manag., **164**(30), pp. 93–101.

[92] Zhang, J., Li, K. J., Wang, M., Lee, W. J., Gao, H., Zhang, C., and Li, K., 2016, "A Bi-Level Program for the Planning of an Islanded Microgrid Including CAES," IEEE Trans. Ind. Appl., **52**(4), pp. 2768–2777.

[93] Ghadi, M. J., Azizivahed, A., Mishra, D. K., Li, L., Zhang, J., Shafie-khah, M., and Catalão, J. P. S., 2021, "Application of Small-Scale Compressed Air Energy Storage in the Daily Operation of an Active Distribution System," Energy, **231**.

[94] Jin, H., Liu, P., and Li, Z., 2019, "Dynamic Modeling and Design of a Hybrid Compressed Air Energy Storage and Wind Turbine System for Wind Power Fluctuation Reduction," Comput. Chem. Eng., **122**, pp. 59–65.

[95] Mucci, S., Bischi, A., Briola, S., and Baccioli, A., 2021, "Small-Scale Adiabatic Compressed Air Energy Storage: Control Strategy Analysis via Dynamic Modelling," Energy Convers. Manag., **243**, p. 114358.

[96] Reboli, T., Ferrando, M., Mantelli, L., Gini, L., Sorce, A., Garcia, J., and Guedez, R., 2022, "GAS TURBINE COMBINED CYCLE RANGE ENHANCER - PART 1: CYBER-PHYSICAL SETUP," pp. 1–15.

[97] Ansaldo Energia, 2016, "AE-T100 Micro Turbine Natural Gas," (v), p. 2 [Online]. Available: https://www.atetsrl.it/Content/Atet/Images/Partner/Ansaldo/allegato (4).pdf.

[98] Turbec, 2009, "T100 Microturbine System: Technical Description," p. 17.

[99] Aslanidou, I., Rahman, M., Zaccaria, V., and Kyprianidis, K. G., 2021, "Micro Gas Turbines in the Future Smart Energy System: Fleet Monitoring, Diagnostics, and System Level Requirements," Front. Mech. Eng., **7**(June), pp. 1–14.

[100] di Gaeta, A., Reale, F., Chiariello, F., and Massoli, P., 2017, "A Dynamic Model of a 100 KW Micro Gas Turbine Fuelled with Natural Gas and Hydrogen Blends and Its Application in a Hybrid Energy Grid," Energy, **129**(2017), pp. 299–320.

[101] Banihabib, R., and Assadi, M., 2022, "A Hydrogen-Fueled Micro Gas Turbine Unit for Carbon-Free Heat and Power Generation," Sustain., **14**(20).

[102] De Paepe, W., Carrero, M. M., Bram, S., Parente, A., and Contino, F., 2018, "Toward Higher Micro Gas Turbine Efficiency and Flexibility-Humidified Micro Gas Turbines: A Review," J. Eng. Gas Turbines Power, **140**(8).

[103] Renzi, M., Caresana, F., Pelagalli, L., and Comodi, G., 2014, "Enhancing Micro Gas Turbine Performance through Fogging Technique: Experimental Analysis," Appl. Energy, **135**, pp. 165–173.

[104] De Paepe, W., Delattin, F., Bram, S., and De Ruyck, J., 2013, "Water Injection in a Micro Gas Turbine - Assessment of the Performance Using a Black Box Method," Appl. Energy, **112**, pp. 1291–1302.

[105] De Paepe, W., Contino, F., Delattin, F., Bram, S., and De Ruyck, J., 2014, "Optimal Waste Heat Recovery in Micro Gas Turbine Cycles through Liquid Water Injection," Appl. Therm. Eng., **70**(1), pp. 846–856.

[106] De Paepe, W., Delattin, F., Bram, S., and De Ruyck, J., 2012, "Steam Injection Experiments in a Microturbine - A Thermodynamic Performance Analysis," Appl. Energy, **97**, pp. 569–576.

[107] Renzi, M., Riolfi, C., and Baratieri, M., 2017, "Influence of the Syngas Feed on the Combustion Process and Performance of a Micro Gas Turbine with Steam Injection," **105**, pp. 1665–1670.

[108] Ferrari, M. L., Pascenti, M., Traverso, A. N., and Massardo, A. F., 2012, "Hybrid System Test Rig: Chemical Composition Emulation with Steam Injection," Appl. Energy, **97**, pp. 809–815.

[109] Paepe, W. De, Montero, M., Bram, S., Parente, A., and Contino, F., 2014, "Experimental Characterization of a T100 Micro Gas Turbine Converted to Full Humid Air Operation .," Energy Procedia, **61**, pp. 2083–2088.

[110] Pascenti, M., Magistri, L., Ferrari, M. L., and Massardo, A. F., 2007, "Micro Gas Turbine Based Test RIG for Hybrid System Emulation," Proc. ASME Turbo Expo, **3**, pp. 7–15.

[111] Barberis, S., Traverso, A. N., Traverso, A., and Massardo, A. F., 2017, "High Temperature Storage for Csp Hybrid Gas Turbine: Test Rig Dynamic Analysis and Experimental Validation," pp. 1–11.

[112] Comodi, G., Renzi, M., Cioccolanti, L., Caresana, F., and Pelagalli, L., 2015, "Hybrid System with Micro Gas Turbine and PV (Photovoltaic) Plant: Guidelines for Sizing and Management Strategies," Energy, **89**, pp. 226–235.

[113] Giorgetti, S., De Paepe, W., Bricteux, L., Parente, A., and Contino, F., 2017, "Carbon Capture on a Micro Gas Turbine: Assessment of the Performance," Energy Procedia, **105**, pp. 4046–4052.

[114] Green, D. W., and Perry, R. H., 2019, *Perry's Chemical Engineers' Handbook*.

[115] Traverso, A., Calzolari, F., and Massardo, A., 2005, "Transient Analysis of and Control System for Advanced Cycles Based on Micro Gas Turbine Technology," J. Eng. Gas Turbines Power, **127**(2), pp. 340–347.

[116] Chen, J., Xiao, G., Luigi, M., Yang, T., and Ni, M., 2020, "Dynamic Simulation of a Solar-Hybrid Microturbine System with Experimental

Validation of Main Parts," Renew. Energy, **154**, pp. 187–200.

[117] Mahmood, M., Traverso, A., Nicola, A., Massardo, A. F., Marsano, D., and Cravero, C., 2018, "Thermal Energy Storage for CSP Hybrid Gas Turbine Systems : Dynamic Modelling and Experimental Validation," Appl. Energy, **212**(November 2017), pp. 1240–1251.

[118] Larosa, L., Traverso, A., and Massardo, A. F., 2016, "Dynamic Analysis of a Recuperated Mgt Cycle for Fuel Cell Hybrid Systems," *Proceedings of the ASME Turbo Expo*, American Society of Mechanical Engineers (ASME).

[119] Mahmood, M., Traverso, A., Traverso, A. N., Massardo, A. F., Marsano, D., and Cravero, C., 2018, "Thermal Energy Storage for CSP Hybrid Gas Turbine Systems: Dynamic Modelling and Experimental Validation," Appl. Energy, **212**(December 2017), pp. 1240–1251.

[120] Montero Carrero, M., Ferrari, M. L., De Paepe, W., Parente, A., Bram, S., and Contino, F., 2015, "Transient Simulations of a T100 Micro Gas Turbine Converted into a Micro Humid Air Turbine," Proc. ASME Turbo Expo 2015, pp. 1–9.

[121] Sk, M., Actions, C., Networks, I. T., Generation, N., Turbines, M. G., Efficiency, H., Emissions, L., Flexibility, F., and No, D., 2022, "Innovative Training Networks (ITN) 861079 – NextMGT (Next Generation of Micro Gas Turbines for High Efficiency , Low Emissions and Fuel Flexibility) Innovation in Heat Exchanger Design for MGTs Including Energy Storage," (861079), pp. 38–44.

[122] Traverso, A., 2005, "TRANSEO Code for the Dynamic Performance Simulation of Micro Gas Turbine Cycles," *Proceedings of the ASME Turbo Expo*, pp. 45–54.

[123] Traverso, A., Massardo, A. F., and Scarpellini, R., 2006, "Externally Fired Micro-Gas Turbine: Modelling and Experimental Performance," Appl. Therm. Eng., **26**(16), pp. 1935–1941.

[124] Powers, K., Kennedy, I., Archer, J., Eynon, P., Horsley, J., Brace, C., Copeland, C., and Milewski, P., 2022, "A New First-Principles Model to Predict Mild and Deep Surge for a Centrifugal Compressor," Energy, **244**, p. 123050.

[125] Ferrari, M. L., Pascenti, M., Magistri, L., and Massardo, A. F., 2010, "Hybrid System Test Rig: Start-up and Shutdown Physical Emulation," J. Fuel Cell Sci. Technol., **7**(2), pp. 0210051–0210057.

[126] Ferrari, M. L., Pascenti, M., Bertone, R., and Magistri, L., 2009, "Hybrid Simulation Facility Based on Commercial 100 KWe Micro Gas Turbine," J. Fuel Cell Sci. Technol., **6**(3), pp. 0310081–0310088.

[127] Renuke, A., Traverso, A., and Pascenti, M., 2019, "Experimental Campaign Tests on a Tesla Micro-Expanders," E3S Web Conf., **113**, pp. 1–

9.

[128] Traverso, A., Reggio, F., Silvestri, P., and Pascenti, M., 2020, "Experimental Investigation on a 3 KW Air Tesla Expander With High Speed Generator," pp. 1–13.

[129] "Gas Prices for Household Consumers - Bi-Annual Data (from 2007 Onwards)."

[130] "Electricity Prices for Household Consumers - Bi-Annual Data (from 2007 Onwards)."

[131] Dave Pemberton, Jim Jewitt, Ryan Pletka, Mike Fischbach, Terry Meyer, Mike Ward, Bob Bjorge, Dave Hargreaves, G. J., 2008, "Mini-Compressed Air Energy Storage for Transmission Congestion Relief and Wind Shaping Applications," New York state energy Res. Dev. Auth.

[132] James B. Marean, 2009, "Compressed Air Energy Storage Engineering and Economic Study," New York state energy Res. Dev. Auth.

[133] Elang Industrial (Shanghai) Co ., L., 2017, "Ielang.En.Alibaba.Com."

[134] GME, 2016, "GME - Gestore Dei Mercati Energetici," pp. 9–10.

[135] Montero Carrero, M., De Paepe, W., Bram, S., Musin, F., Parente, A., and Contino, F., 2016, "Humidified Micro Gas Turbines for Domestic Users: An Economic and Primary Energy Savings Analysis," Energy, **117**(December), pp. 429–438.

[136] Ashfaq, A., and Ianakiev, A., 2018, "Cost-Minimised Design of a Highly Renewable Heating Network for Fossil-Free Future," Energy, **152**, pp. 613–626.

[137] Vasylyev, A., Vannoni, A., and Sorce, A., 2023, "Best Practices for Electricity Generators and Energy Storage Pptimal Dispatch Problems," pp. 1–14.

[138] Ali, M. Y., Khan, F., and Sood, V. K., 2018, "Swarm Optimization and Wireless Communication System," 2018 IEEE Electr. Power Energy Conf., pp. 1–7.

[139] IRNEA, 2022, *Renewable Power Generation Costs in 2021*.

[140] Proost, J., 2019, "State-of-the Art CAPEX Data for Water Electrolysers, and Their Impact on Renewable Hydrogen Price Settings," Int. J. Hydrogen Energy, **44**(9), pp. 4406–4413.